**Title**
Design and Synthesis of Metal-Organic Frameworks for Hydrogen Storage and Carbon Dioxide Capture



**Author**
Sumida, Kenji

**Publication Date**
2012

Peer reviewed|Thesis/dissertation

# Design and Synthesis of Metal-Organic Frameworks for Hydrogen Storage and Carbon Dioxide Capture

By

Kenji Sumida

A dissertation submitted in partial satisfaction of the

requirements for the degree of

Doctor of Philosophy

in

Chemistry

in the

Graduate Division

of the

University of California, Berkeley

Committee in charge:

Professor Jeffrey R. Long, Chair
Professor Richard A. Andersen
Professor Roger W. Falcone

Fall 2012

Design and Synthesis of Metal-Organic Frameworks
for Hydrogen Storage and Carbon Dioxide Capture



by

Kenji Sumida

Abstract

Design and Synthesis of Metal-Organic Frameworks
for Hydrogen Storage and Carbon Dioxide Capture

by

Kenji Sumida

Doctor of Philosophy in Chemistry

University of California, Berkeley

Professor Jeffrey R. Long, Chair

This dissertation describes the design and synthesis of metal-organic frameworks for applications in high-density hydrogen storage for mobile applications, and in post-combustion carbon dioxide capture from coal- or gas-fired power plants.

*Chapter One* introduces the area of metal-organic frameworks, which are a new class of porous coordination solids, with an emphasis on the parameters requiring optimization in order to achieve applications in hydrogen storage and carbon dioxide capture. The current state-of-the-art is briefly discussed, and strategies for the development of next-generation materials exhibiting enhanced performance are presented in the context of metal-organic frameworks. Furthermore, the benefit of high-throughput technologies in the synthesis and characterization of metal-organic frameworks is also highlighted as a potential means of accelerating the discovery of high-performance materials.

In *Chapter Two*, the synthesis and hydrogen storage properties of $Be_{12}(OH)_{12}(BTB)_4$, the first metal-organic framework based on the lightest divalent metal, $Be^{2+}$, is described. The high surface area resulting from the use of lightweight $Be^{2+}$ cations leads to one of the highest gravimetric hydrogen storage densities observed at both cryogenic and ambient temperatures.

*Chapter Three* introduces the use of a high-throughput methodology in the synthesis of an $Fe^{2+}$-based, sodalite-type metal-organic framework, $Fe_3[(Fe_4Cl)_3(BTT)_8]_2$ (Fe-BTT). This material features a high-density of exposed metal cation adsorption sites on the pore surface, which facilitates strong framework-$H_2$ interactions that are close to the adsorption enthalpy considered optimal for hydrogen storage at ambient temperatures. The resulting hydrogen adsorption

properties are discussed, as well as the effect of these adsorption sites on the carbon dioxide capture performance.

The hydrogen storage properties of $Mg_2$(dobdc), a lightweight metal-organic framework possessing $Mg^{2+}$ adsorption sites, are studied in *Chapter Four* using a combination of adsorption experiments, infrared spectroscopy, and powder neutron diffraction data. The high affinity of $H_2$ toward the exposed metal cation sites results in a high enthalpy of adsorption, which is of importance in raising the storage density at ambient temperatures.

*Chapter Five* describes the hydrogen storage properties of $Cr_3(BTC)_2$, a metal-organic framework featuring pores decorated with $Cr^{2+}$ adsorption sites. In contrast to Fe-BTT and $Mg_2$(dobdc), the relatively diffuse nature of the $Cr^{2+}$ cations results in a low adsorption enthalpy at these sites, highlighting the importance of the identity of the metal ion in controlling the thermodynamics of adsorption.

*Chapter Six* describes a new high-throughput methodology developed for the synthesis and adsorption screening of new metal-organic frameworks for carbon dioxide capture. The use of the workflow is discussed in the context of metal-insertion reactions within the material Al(OH)(bpydc), which features one-dimensional pores lined with 2,2'-bipyridine binding sites. As will be demonstrated, the metal salt employed imparts a considerable impact on the $CO_2$ adsorption capacity, highlighting the benefit of a high-throughput approach to materials optimization.

The precise control of the opposing wall distribution within metal-organic frameworks is an important aspect in optimizing the adsorption properties for high-density storage and molecular separation applications. In *Chapter Seven*, a new method for geometrically calculating the wall separation distances from the single-crystal structure is described and employed in studying a variety of known structure types. In this case, the routine is used to analyze metal-organic frameworks for methane storage due to the abundance of high-pressure methane adsorption data in the literature, and it is demonstrated that the optimization of the wall separations is indeed crucial for maximizing the volumetric storage capacity in storage applications.

# Table of Contents

# List of Figures

**Chapter 4**



**Chapter 5**

**Chapter 6**



**Chapter 7**

**Appendix A**



**Appendix B**

# List of Tables

# Chapter 1: Design and Synthesis of Metal-Organic Frameworks for Hydrogen Storage and Carbon Dioxide Capture

## 1.1 Introduction

Metal-organic frameworks are a new class of porous solids that have attracted much recent attention owing to their potential applications in a variety of areas, including gas storage, molecular separations, heterogeneous catalysis, and drug delivery.[1] These structures consist of metal-based nodes (single ions or clusters) bridged by organic linking groups to form a one-, two-, or three-dimensional coordination network. From an applications point of view, their extraordinary surface areas ($SA_{Langmuir}$ of up to 10,400 $m^2/g$),[2] finely tunable pore surface properties,[3] and potential scalability to industrial scale[4] have made these materials an attractive target for further study. Although a number of excellent reviews already exist on the synthetic and structural aspects of metal-organic frameworks,[1a,b,5,6] a number of key aspects of these materials are described here in order to present the promises and challenges of utilizing metal-organic frameworks for hydrogen storage and carbon dioxide capture.

## 1.2 Metal-Organic Frameworks

The preparation of metal-organic frameworks is generally achieved via the combination of metal ions and an organic bridging unit in a high-boiling, polar solvent, resulting in a crystalline coordination solid as shown schematically in Figure 1.1. This modular approach is particularly attractive in the context of synthesizing materials that display a specific chemical or structural property, since control over the material characteristics can often be achieved by rational selection of the individual components. For example, the use of metal ions exhibiting a preference for certain coordination geometries (or having a tendency for forming clusters that facilitate a certain external coordination geometry), or the incorporation of organic ligands possessing a specific geometry or functionalization, presents the opportunity for the properties of the resulting framework to be optimized for a given application.

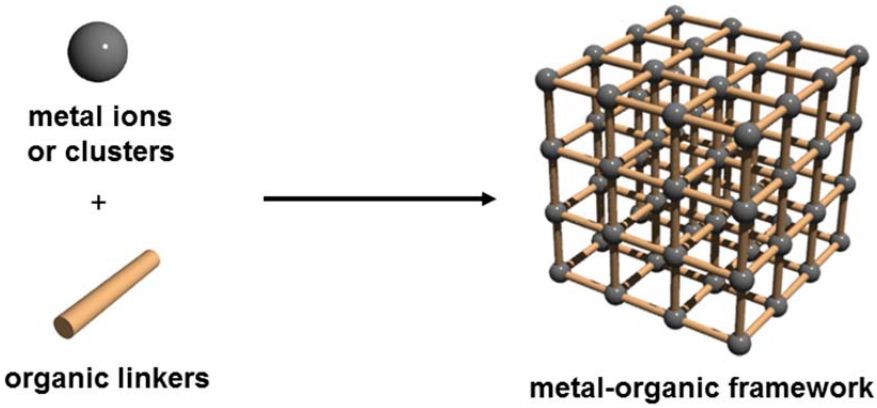


***Figure 1.1.*** A schematic drawing showing the concept of a metal-organic framework, in which metal-based nodes (consisting of single ions or polynuclear clusters), and multitopic organic briding units are combined in solution to assemble a three-dimensional metal-organic framework.

One of the most well-studied metal-organic frameworks, and one that serves as an illustrative example of the versatility of these compounds as a platform for developing next-generation materials, is the $Zn_4O(BDC)_3$ (MOF-5; $BDC^{2-}$ = 1,4-benzenedicarboxylate) network depicted in Figure 1.2.[7] This material consists of tetrahedral $[Zn_4O]^{6+}$ clusters bridged by ditopic $BDC^{2-}$ ligands to form a cubic, three-dimensional network with a BET surface area as high as 3800 $m^2/g$.[7c] Importantly, from the perspective of materials optimization, functionalized derivatives of the MOF-5 structure type can be prepared using other substituted linear dicarboxylate linkers, allowing the linker length or functional groups present on the aromatic backbone to be readily modified, while preserving the overall connectivity of the framework.[3a,8] More recently, this concept has been extended to other families of materials, such as the $Zr_6O_4(OH)_4(BDC)_6$ (UiO-66),[9,10] Al(OH)(BDC) (MIL-53),[11] and $Cu_2$(BPTC) (NOTT-100; $BPTC^{4-}$ = 3,3',5,5'-biphenyltetracarboxylate)[12] structure types. In each case, the length and functionality of the ligands can be changed, while forming materials of the same network connectivities. As discussed in the forthcoming sections, in the context of $H_2$ storage and post-combustion $CO_2$ capture, the ability to readily modify the surface chemistry of metal-organic frameworks is of particular interest for installing the desired chemical features (such as exposed metal cations, amines, or polarizing groups) for enhancing the performance of the material.

## 1.3 High-Density Hydrogen Storage for Mobile Applications

The widespread deployment of carbon-neutral energy sources for use in mobile applications is of paramount importance due to the increasing atmospheric levels of $CO_2$ resulting from the combustion of fossil fuels. As a result of its high energy content, clean combustion, and potential renewability, hydrogen is one of the leading candidates in this regard, although its high fugacity presents a difficult challenge in terms of its safe and efficient storage.

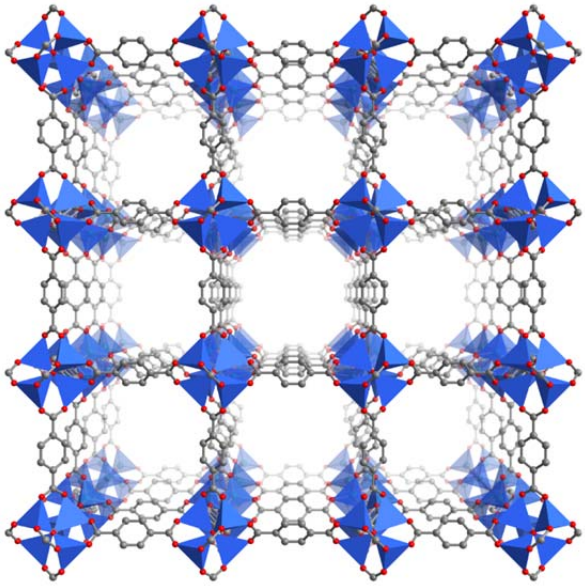

***Figure 1.2.*** A portion of the crystal structure of $Zn_4O(BDC)$ (MOF-5; $BDC^{2-}$ = 1,4-benzenedicarboxylate). The network consists of $[Zn_4O]^{6+}$ units bridged by the linear $BDC^{2-}$ bridging units to form a porous, three-dimensional coordination solid.

The U.S. Department of Energy (DOE) has set system performance targets[13] for mobile hydrogen storage systems with respect to their storage capacities, operating temperature, system cost, kinetics of refueling and delivery, and durability. The most commonly employed storage methods currently involve compression within insulated pressure tanks,[14] although the cooling systems used in these configurations are too bulky and energy-intensive to emerge as a practical alternative to petroleum fuel tanks. This has spurred interest in a variety of other modes of storage of hydrogen, including chemisorptive systems such as metal hydrides, and in physisorptive storage within high-surface area porous materials.[15]

Metal-organic frameworks have recently come under intense investigation for applications in hydrogen storage, as a result of their high internal surface areas, convenient modular synthesis, and chemical tunability. At cryogenic temperatures, gravimetric and/or volumetric hydrogen storage capacities approaching the U.S. DOE targets for have been demonstrated within the highest-surface area materials,[7c,16] although the weak affinity for $H_2$ toward the surfaces of these materials leads to a greatly diminished storage density at ambient temperatures. In order to increase the storage density of metal-organic frameworks, the following two strategies are proposed: (1) the use of lightweight metal nodes consisting of main group elements; and (2) the decoration of the pore surfaces of metal-organic frameworks with highly polarizing binding sites to raise the adsorption enthalpy of $H_2$.

**Lightweight Materials.** The construction of metal-organic frameworks from light main group metal ions such as $Be^{2+}$, $Mg^{2+}$, or $Al^{3+}$, rather than the commonly employed heavier first-row transition metals, namely $Cu^{2+}$ or $Zn^{2+}$ represents a promising strategy for raising the storage capacity of metal-organic frameworks. In particular, the construction of isostructures of the high surface area $Zn^{2+}$-based structure types using lighter divalent metals would afford a significant boost in the gravimetric storage capacity, due to the reduction of the mass of the system attributable to the framework scaffold while accommodating a comparable quantity of $H_2$ into the pores on a per-volume basis. Additionally, from a fundamental perspective, the use of these ions to prepare metal-organic frameworks is still relatively rare, potentially allowing the discovery of new structure types exhibiting unique adsorption properties (see Chapter 2).

**Polarizing Surface Functionalities.** One of the main challenges facing the use of metal-organic frameworks as adsorbents in mobile $H_2$ storage applications is the low adsorption capacities at ambient temperatures arising as a result of the weak, physisorptive interactions between $H_2$ and the surfaces of the materials. Indeed, the isosteric heat of adsorption within most metal-organic frameworks studied to date lies within the range of –5 to –7 kJ/mol, while the optimal value for an adsorbent operating between 1.5 and 100 bar at 298 K is considered to be as high as –20 to –25 kJ/mol.[17] This has prompted researchers to pursue new structure types possessing high densities of polarizing binding sites, such as exposed metal cations,[18] decorating the pores of the framework. Such metal centers would serve as strong binding sites because they represent a positive point-charge that would facilitate a dipole-induced dipole interaction that is considerably stronger than the typical dispersion-type forces that predominate within most metal-organic frameworks (see Chapter 3-5).

## 1.4 Post-Combustion Carbon Dioxide Capture

Although the transition of the existing infrastructure from carbon-based sources to cleaner alternatives would be ideal for the mitigation of $CO_2$ emissions, such a change requires considerable modifications to the current energy framework, and many of the proposed technologies are not yet sufficiently developed to facilitate large-scale industrial implementation. Thus, carbon capture and sequestration (CCS) technologies that efficiently capture $CO_2$ from existing emission sources are also expected to play a vital role until more significant modifications to the energy infrastructure can be realized.

One scenario under which $CO_2$ capture technologies could be rapidly implemented is at stationary point sources, such as coal and natural gas-fired power plants. In the United States, 41% of the total $CO_2$ emissions can be attributed to electricity generation[19] 3 (ca. 60% worldwide),[20] and hence the installation of effective post-combustion $CO_2$ capture systems to existing plant configurations could offer a large reduction in emissions. The captured $CO_2$ would then be subjected to permanent sequestration, where the $CO_2$ is injected into underground geological formations, such as depleted oil reservoirs or salt water aquifers. Here, similar technologies are already established for processes such as enhanced oil recovery (EOR), and several trial $CO_2$ sequestration sites are in construction.[21] Note that the reuse of the captured $CO_2$ as a reactant in chemical transformations presents an alternative sequestration pathway, although it would not be a viable long-term strategy owing to the tremendous scale of worldwide $CO_2$ emissions (ca. 30 Gt per year)[22] resulting in the market for any commodities prepared therefrom being rapidly saturated.

The most significant challenge for a CCS framework employing post-combustion $CO_2$ capture at present is the large energy penalty associated with the capture process. With current technologies, approximately 70% of the cost of CCS is associated with the selective capture of $CO_2$ from the power plant flue gas,[23] a value that must certainly be reduced if such an approach for $CO_2$ mitigation is to become viable. The high cost primarily arises from the large energy input required for regeneration of the capture material. Indeed, $CO_2$ capture from a post-combustion flue gas using the most highly developed current technologies involving aqueous alkanolamine solutions carries an energy penalty of roughly 30% of the output of the power plant, most of which is associated with the heating of the large volumes of water in which the amine is dissolved in order to liberate the captured $CO_2$.[23] Thus, minimization of the energy input for regeneration, through fine-tuning of the thermodynamics of the interaction between $CO_2$ and the adsorbent, for example, is one of the most crucial considerations in improving the energy efficiency of $CO_2$ capture.

As mentioned above, owing to their large capacity for the adsorption of gases and their structural and chemical tunability, metal-organic frameworks could serve as an ideal platform for the development of next-generation $CO_2$ capture materials. From the perspective of lowering the energy penalty associated with the capture step, the use of a solid adsorbent is expected to yield significant advantages over an the alkanolamine-based system due to the considerably lower heat capacity of a porous solid compared to an aqueous medium (see Appendix A). Moreover, a number of metal-organic frameworks have already been shown to exhibit a tremendously high selectivity for $CO_2$ over $N_2$,[24] which is the predominant gas separation in post-combustion $CO_2$ capture. The main challenge facing the use of these materials is the fact that they do not exhibit a sufficiently high stability or performance level in the presence of water and the other contaminants present in the flue gas.[25] This has prompted the search for new materials

possessing an enhanced stability profile, such that the performance can be retained over many thousands of cycles. In this regard, the preparation of materials possessing strong metal-ligand bonds by using high-valent metal ions, such as $Al^{3+}$, $Ti^{4+}$ or $Zr^{4+}$, and/or more basic ligand groups, such as imidazolates, pyrazolates, or triazolates, is expected to afford materials that would exhibit a sufficiently high long-term chemical and thermal robustness under the conditions of post-combustion $CO_2$ capture and material regeneration.

## 1.5 High-Throughput Strategies for the Discovery of Metal-Organic Frameworks

Despite the apparent simplicity of the modular synthesis of metal-organic frameworks, one of the greatest challenges in preparing new materials lies in optimizing the reaction conditions that lead to the desired framework in high yield and crystallinity. Slight changes in the reaction parameters employed, such as the reactant concentration, the presence of a co-solvent, solution pH, metal-to-ligand ratio, metal counteranion, reaction temperature, and reaction time, can have a considerable impact on the products that are obtained. Note that even in cases where just a single metal and ligand are combined, a large number of network connectivities may be possible, many of which are nonporous structures that are not of interest for gas storage and gas separation applications. These undesired phases can often coprecipitate with the porous phase of interest, giving rise to a mixture that is not readily separated owing to the insolubility of the components. Thus, the discovery of optimized conditions that afford the desired product can involve a large number of trial reactions in which the reaction parameters are systematically varied. Consequently, numerous studies involving the use of high-throughput technologies have appeared in recent years,[26] and as demonstrated in Chapters 3 and 6, this has prompted the development of a new methodology for the rapid discovery and characterization of new metal-organic frameworks for $H_2$ storage and $CO_2$ capture.

## 1.6 References and Notes


(1) (a) Kitagawa, S.; Kitaura, R.; Noro, S.-I. *Angew. Chem., Int. Ed.* **2004**, *43*, 2334. (b) Férey, G. *Chem. Soc. Rev.* **2008**, *37*, 191. (c) Morris, R. E.; Wheatley, P. S. *Angew. Chem., Int. Ed.* **2008**, *47*, 4966. (d) Li, J.-R.; Kuppler, R. J.; Zhou, H.-C. *Chem. Soc. Rev.* **2009**, *38*, 1477. (e) Lee, J. Y.; Farha, O. K.; Roberts, J.; Scheidt, K. A.; Nguyen, S. T.; Hupp, J. T. *Chem. Soc. Rev.* **2009**, *38*, 1450. (f) Murray, L. J.; Dincă, M.; Long, J. R. *Chem. Soc. Rev.* **2009**, *38*, 1294. (g) Kuppler, R. J.; Timmons, D. J.; Fang, Q.-R.; Li, J.-R.; Makal, T. A.; Young, M. D.; Yuan, D.; Zhao, D.; Zhuang, W.; Zhou, H.-C. *Coord. Chem. Rev.* **2009**, *253*, 3042. (h) Farrusseng, D.; Aguado, S.; Pinel, C. *Angew. Chem., Int. Ed.* **2009**, *48*, 7502. (i) Corma, A.; García, H.; Llabrés I Xamena, F. X. *Chem. Rev.* **2010**, *110*, 4606.

(2) Furukawa, H.; Ko, N.; Go, Y. B.; Aratani, N.; Choi, S. B.; Choi, E.; Yazaydin, A. O.; Snurr, R. Q.; O'Keefe, M.; Kim, J.; Yaghi, O. M. *Science* **2010**, *329*, 424.

(3) (a) Rowsell, J. L. C.; Yaghi, O. M. *J. Am. Chem. Soc.* **2006**, *128*, 1304. (b) Furukawa, H.; Kim, J.; Ockwig, N. W.; O'Keefe, M.; Yaghi, O. M. *J. Am. Chem. Soc.* **2008**, *130*, 11650. (c) Wang, Z.; Cohen, S. M. *Chem. Soc. Rev.* **2009**, *38*, 1315. (d) Tanabe, K. K.; Cohen, S. M. *Chem. Soc. Rev.* **2011**, *40*, 498.

(4) Czaja, A. U.; Trukhan, N.; Müller, U. *Chem. Soc. Rev.* **2009**, *38*, 1284.

(5) Férey, G.; Mellot-Draznieks, C.; Serre, C.; Millange, F. *Acc. Chem. Res.* **2005**, *38*, 217.

(6) Kitagawa, S.; Matsuda, R. *Coord. Chem. Rev.* **2007**, *251*, 2490.

(7) (a) Li, H.; Eddaoudi, M.; O'Keefe, M.; Yaghi, O. M. *Nature* **1999**, *402*, 276. (b) Eddaoudi, M.; Li, H.; Yaghi, O. M. *J. Am. Chem. Soc.* **2000**, *122*, 1391. (c) Kaye, S. S.; Dailly, A.; Yaghi, O. M.; Long, J. R. *J. Am. Chem. Soc.* **2007**, *129*, 14176.
(8) Eddaoudi, M.; Kim, J.; Rosi, N.; Vodak, D.; Wachter, J.; O'Keefe, M.; Yaghi, O. M. *Science* **2002**, *295*, 469.
(9) Cavka, J. H.; Jakobsen, S.; Olsbye, U.; Guillou, N.; Lamberti, C.; Bordiga, S.; Lillerud, K. P. *J. Am. Chem. Soc.* **2008**, *130*, 13850.
(10) Garibay, S. J.; Cohen, S. M. *Chem. Commun.* **2010**, *46*, 7700.
(11) Biswas, S.; Ahnfeldt, T.; Stock, N. *Inorg. Chem.* **2011**, *50*, 9518.
(12) Lin, X.; Telepeni, I.; Blake, A. J.; Dailly, A.; Brown, C. M.; Simmons, J. M.; Zoppi, M.; Walker, G. S.; Thomas, M.; Mays, T. J.; Hubberstey, P.; Champness, N. R.; Schröder, M. *J. Am. Chem. Soc.* **2009**, *131*, 2159.
(13) EERE: Hydrogen, Fuel Cells, & Infrastructure Technologies Program, http://www.eere.energy.gov/hydrogenandfuelcells/ (accessed January 2010).
(14) (a) Aceves, S. M.; Berry, G. D.; Martinez-Frias, J.; Espinosa-Loza, F. *Int. J. Hydrogen Storage* **2006**, *31*, 2274. (b) Kumar, V. S.; Raghunathan, K.; Kumar, S. *Int. J. Hydrogen Storage* **2009**, *34*, 5466.
(15) Eberle, U.; Felderhoff, M.; Schüth, F. *Angew. Chem., Int. Ed.* **2009**, *48*, 6608.
(16) (a) Furukawa, H.; Miller, M. A.; Yaghi, O. M. *J. Mater. Chem.* **2007**, *17*, 3197. (b) Latroche, M.; Surblé, S. ; Serre, C.; Mellot-Draznieks, C.; Llewellyn, P. L.; Lee, J.-H.; Chang, J.-S.; Jhung, S. H.; Férey, G. *Angew. Chem., Int. Ed.* **2006**, *45*, 8227. (c) Koh, K.; Wong-Foy, A. G.; Matzger, A. J. *J. Am. Chem. Soc.* **2009**, *131*, 4184.
(17) (a) Bhatia, S. K.; Myers, A. L. *Langmuir* **2006**, *22*, 1688. (b) Garrone, E.; Bonelli, B.; Otero Areán, C. *Chem. Phys. Lett.* **2008**, *456*, 68. (c) Otero Areán, C.; Chavan, S.; Cabello, C. P.; Garrone, E.; Palomino, G. T. *ChemPhysChem* **2010**, *11*, 3237.
(18) Dincă, M.; Long, J. R. *Angew. Chem., Int. Ed.* **2008**, *47*, 6766.
(19) U.S. Environmental Protection Agency: http://www.epa.gov/climatechange/emissions/co2_human.html.
(20) Pachauri, R. K.; Reisinger, A. IPCC Fourth Assessment Report, Intergovernmental Panel on Climate Change, 2007.
(21) Carbon Capture and Storage, Full-Scale Demonstration Progress Update: www.iea.org/G8/docs/ccs_g8july09.pdf, OECD/IEA, 2009.
(22) International Energy Agency (IEA): http://www.iea.org/index_info.asp?id=1959, 2011.
(23) Haszeldine, R. S. Science 2009, 325, 1644.
(24) (a) Caskey, S. R.; Wong-Foy, A. G.; Matzger, A. J. *J. Am. Chem. Soc.* **2008**, *130*, 10870. (b) Dietzel, P. D. C.; Johnsen, R. E.; Fjellvag, H.; Bordiga, S.; Groppo, E.; Chavan, S.; Blom, R. *Chem. Commun.* **2008**, 5125. (c) Dietzel, P. D. C.; Besikiotis, V.; Blom, R. *J. Mater. Chem.* **2009**, *19*, 7362. (d) Britt, D.; Furukawa, H.; Wang, B.; Glover, T. G.; Yaghi, O. M. *Proc. Natl. Acad. Sci. U. S. A.* **2009**, *106*, 20637. (e) Yazaydin, A. Ö.; Snurr, R. Q.; Park, T.-H.; Koh, K.; Liu, J.; LeVan, M. D.; Benin, A. I.; Jakubczak, P.; Lanuza, M.; Galloway, D. B.; Low, J. J.; Willis, R. R. *J. Am. Chem. Soc.* **2009**, *131*, 18198.
(25) Kizzie, A. C.; Wong-Foy, A. G.; Matzger, A. J. *Langmuir* **2011**, *27*, 6368.
(26) (a) Bauer, S.; Serre, C.; Devic, T.; Horcajada, P.; Marrot, J.; Férey, G.; Stock, N. *Inorg. Chem.* **2008**, *47*, 7568. (b) Biemmi, E.; Christian, S.; Stock, N.; Bein, T. *Microporous Mesoporous Mater.* **2009**, *117*, 111. (c) Ahnfeldt, T.; Guillou, N.; Gunzelmann, D.;

Margiolaki, I.; Loiseau, T.; Férey, G.; Senker, J.; Stock, N. *Angew. Chem., Int. Ed.* **2009**, *48*, 5163. (d) Palanikumar, M.; Stock, N. *Inorg. Chem.* **2011**, *50*, 5085.

# Chapter 2: Synthesis and Hydrogen Storage Properties of $Be_{12}(OH)_{12}$(1,3,5-benzenetribenzoate)$_4$

## 2.1 Introduction

Owing to their convenient modular synthesis and high surface areas, metal-organic frameworks have come under intense recent scrutiny for potential applications in gas storage.[1] The dense storage of hydrogen for use in fuel cell vehicles presents a particularly difficult challenge as a consequence of its high fugacity, which has prompted development of insulated pressure tanks for cryogenic storage.[2] For an adsorbent within such a system, $Zn_4O$(1,4-benzenedicarboxylate)$_3$ (MOF-5) offers the best known hydrogen storage properties, exhibiting a total uptake of 10 wt % and 66 g/L at 77 K and 100 bar.[3] One possible means of improving the gravimetric capacity for this type of material would be to replace the typically di- or trivalent transition metal centers with light main group ions such as $Be^{2+}$, $B^{3+}$, $Mg^{2+}$, or $Al^{3+}$.[4] For example, substitution of the lightest divalent metal, $Be^{2+}$, for the $Zn^{2+}$ ions in MOF-5 would be expected to lead to a roughly 40% increase in both surface area and gravimetric hydrogen storage capacity.[5,6] Although early experiments involving addition of dicarboxylate bridging ligands to beryllium-containing solutions were recognized as leading to three-dimensional polymeric solids (i.e., metal-organic frameworks),[7] the isolation of such materials as pure, crystalline phases has proven elusive. Herein, we report the synthesis and hydrogen storage properties of the first structurally characterized metal-organic framework based upon beryllium: $Be_{12}(OH)_{12}$(1,3,5-benzenetribenzoate)$_4$ (Be-BTB).

## 2.2 Experimental Section

Dimethylsulfoxide (DMSO) and N,N-dimethylformamide (DMF) were dried over activated 4 Å sieves prior to use. The compound 1,3,5-benzenetribenzoic acid was prepared according to the literature procedure.[1d] All other reagents were obtained from commercial vendors and used without further purification. ***Caution!*** Beryllium compounds can pose a serious health risk through skin contact and inhalation. All manipulations of solid beryllium-containing materials should be performed in a fumehood or glove bag, taking care not to generate airborne dust in the open air under any circumstances.

**$Be_{12}(OH)_{12}$(1,3,5-benzenetribenzoate)$_4$ (Be-BTB).** ***Caution!*** This reaction results in partial decomposition of DMSO, liberating toxic $SO_2$ gas, the inhalation of which should be avoided. To a borosilicate tube (1.2 mm o.d., 20 cm length) was charged 1,3,5-benzenetribenzoic acid (18 mg, 0.041 mmol) and a mixed solution of DMSO (1.9 mL) and DMF (0.1 mL). Upon dissolution of the ligand, an aqueous solution of beryllium nitrate (65 μL, 35 wt %, Aldrich) was added. The solution was degassed by the freeze-pump-thaw method (3 cycles), and the tube was subsequently flame-sealed under a reduced pressure. The tube heated in an oven at 130 °C for 10 days, after which time large (0.5 mm × 0.5 mm × 0.5 mm) colorless block-shaped single crystals were observed as a single phase. The tube was removed from the oven, cooled to room temperature, and broken open in a fumehood. The mother liquor was decanted from the sample, and the solid was washed three times with DMF, followed by dichloromethane, and collected by filtration. Activation of the sample was performed by transferring the collected product into a nitrogen-filled glove bag, where the solid was soaked in anhydrous dichloromethane (5 mL) for 8 h. The supernatant was decanted and replenished a further four times over 2 days, and after the

final wash a gentle stream of nitrogen was passed over the sample so as to remove excess solvent. The product is hygroscopic and was therefore stored in a glove box under a dinitrogen atmosphere, and final degassing was performed on a vacuum manifold. Yield: 17 mg (81%). IR (solid, ATR): 3413 (br w), 3047 (br w), 1595 (s), 1550 (m), 1519 (m), 1435 (s), 1392 (m), 1310 (w), 1252 (w), 1187 (w), 1106 (w), 1015 (m), 986 (br m), 876 (m), 854 (m), 829 (m), 783 (s), 760 (s), 712 (m), 606 (m), 539 (m), 511 (m). Anal. Calcd for $C_{27}H_{18}Be_3O_9 \cdot 3H_2O$: C, 57.14; H, 4.26. Found: C 56.85; H 3.96.

**X-ray Structure Determination.** A block-shaped single crystal of Be-BTB (0.22 mm × 0.22 mm × 0.25 mm) was coated in Paratone-N oil, attached to a Kapton loop, and mounted on a Bruker X8 APEX diffractometer equipped with a Bruker MICROSTAR Cu rotating anode X-ray source. The sample was cooled to 100 K under a stream of nitrogen, and preliminary cell data were obtained to yield a tetragonal Laue group. A full hemisphere of data was collected over a period of 24 h, after which time the crystal showed no significant decomposition or structural distortion. Data were integrated and corrected for Lorentz, polarization, and absorption effects within the APEX 2 software package. Crystal and refinement parameters are listed in Table 2.1. Space group determinations were made based on systematic absences, *E* statistics, and successful refinement of the structure. The structure solution was obtained using direct methods and the SHELXS-97 software, and expanded through successive difference Fourier maps. Thermal parameters for all non-hydrogen atoms were refined anisotropically, and hydrogen atoms were assigned to ideal positions using the appropriate AFIX commands. Complete modeling of the solvent within the pores was not possible due to disorder, hence the electron density within the cavities was masked using the SQUEEZE routine within the PLATON software package.[8]

**Accessible Surface Area Calculations.** The source code for the accessible surface area calculation program was obtained free of charge from the Internet.[9] The crystallographic information file (CIF) obtained from the single crystal X-ray structure was converted to the XYZ file format using Mercury CSD 2.0. The XYZ file and UFF force field atomic parameters[10] were used as input for the simulation (atomic diameters (Å): H 2.571, Be 2.446, C 3.431, O 3.118), and the accessible surface area was evaluated using a dinitrogen-sized probe molecule (diameter = 3.681 Å) inserted at randomized points in the unit cell, and averaging the resultant individual accessible surface area values after 5000 trials.

**Low-Pressure Gas Sorption Measurements.** Glass sample tubes of a known weight were loaded with approximately 200 mg of sample, and sealed using a TranSeal. Samples were degassed at 100 °C for 24 h on a Micromeritics ASAP 2020 analyzer until the outgas rate was no more than 1 mTorr/min. The degassed sample and sample tube were weighed precisely and then transferred back to the analyzer (with the TranSeal preventing exposure of the sample to the air after degassing). The outgas rate was again confirmed to be less than 1 mTorr/min. Adsorption isotherms were measured at 77 K in a liquid nitrogen bath for $H_2$ and $N_2$, and at 87 K in a liquid argon bath for $H_2$.

**Isosteric Heat of Adsorption Calculations.** The $H_2$ uptake isotherms obtained at 77 K and 87 K were fitted to the virial system of equations using the R statistical software package.[11] The quality of the fit was confirmed by comparing the modeled data with the experimental data.

**High-Pressure Gas Sorption Measurements.** In a typical measurement, at least 200 mg of sample was loaded in a sample holder in a glove box under an argon atmosphere. The sample was evacuated at 100 °C for 10 h under a pressure of less than $10^{-5}$ torr. Hydrogen excess adsorption measurements were performed on an automated Sieverts' apparatus (PCTPro-2000 from Hy-Energy Scientific Instruments LLC) over a pressure range of 0-100 bar. UHP-grade

hydrogen and helium (99.999% purity) were used for all measurements. Volumetric measurements at 77 K were carried out by submerging the sample holder in a liquid nitrogen bath, for which the fill-level was maintained constant throughout the experiment.

The total adsorption, $C_{tot}$ was calculated using the following relationship;

$$C_{tot} = C_{exc} + \frac{100 \times d_g V_{pore}}{1 + d_g V_{pore}} \qquad (2.1)$$

where $C_{exc}$ is the excess uptake, $d_g$ represents the density of pure $H_2$ gas calculated from an isothermal equation of state,[12] $V_{pore}$ is the pore volume of the sample. $V_{pore}$ is readily calculated from the experimental skeletal density of the sample, $d_{sk}$, and the crystallographically determined bulk density of the sample, $d_{bulk}$, using the expression below;

$$V_{pore} = \frac{d_{sk} - d_{bulk}}{d_{sk} d_{bulk}} \qquad (2.2)$$

The total volumetric uptake, $C_{vol}$, was calculated by;

$$C_{vol} = Q_{ads}\, d_{bulk} \qquad (2.3)$$

where $Q_{ads}$ represents the total $H_2$ adsorbed (in mmol/g). Alternatively, the excess volumetric uptake can be calculated if the excess quantity of $H_2$ is used in place of $Q_{ads}$.

**Other Physical Measurements.** Powder X-ray diffraction patterns were obtained on a Bruker D8 Advance diffractometer with a Cu anode ($\lambda$ = 1.5406 Å). Infrared spectra were obtained on a Perkin-Elmer Spectrum 100 Optica FTIR spectrometer furnished with an attenuated total reflectance accessory (ATR). Carbon, hydrogen, and nitrogen analyses were obtained from the Microanalytical Laboratory at the University of California, Berkeley. Thermogravimeteric analyses (TGA) were performed on a TA Instruments TGA 5000 instrument at a ramp rate of 2 °C/min under a flow of nitrogen.

***Table 2.1.*** Crystallographic parameters for the crystal structure of $Be_{12}(OH)_{12}(BTB)_4$

| Crystallographic Parameter | Observed Value |
|---|---|
| Formula | $C_{54}H_{36}Be_6O_{18}$ |
| FW | 1026.89 |
| $T$, K | 100(2) |
| Wavelength, Å | 1.54178 |
| Crystal system, space group | Tetragonal, $P\bar{4}\ c2$ |
| Z | 8 |
| $a$, Å | 24.3013(9) |
| $b$, Å | 24.3013(9) |
| $c$, Å | 54.570(3) |
| $V$, Å$^3$ | 32226.5 |
| $d_{calc}$, g/cm$^3$ | 0.412 |
| Absorption coefficient, mm$^{-1}$ | 0.259 |
| $F$(000) | 4224 |
| Crystal size, mm$^3$ | 0.22×0.22×0.25 |
| Theta range for data collection | 1.62-50.46 |
| Index range | $-21 \leq h \leq 23$, $-24 \leq k \leq 24$, $-54 \leq l \leq 54$ |
| Reflections collected ($R$(int) = 0.0257) | 16885 [R(int) = 0.0257] |
| Independent reflections | 8940 |
| Data/restraints/parameters | 16885 / 0 / 704 |
| GOF on $F^2$ | 0.961 |
| Largest diff. peak and hole, e·A$^{-3}$ | 0.06 and –0.23 |
| $R_1(wR_2)$[a], [I > $\sigma$(I)] | 0.0315 |
| $R_1(wR_2)$[a], all data | 0.0863 |

[a] $R_1 = \Sigma||F_o|-|F_c||/\Sigma|F_o|$, $wR_2 = \{\Sigma[w(F_o^2-F_c^2)^2]/\Sigma[w(F_o^2)^2]\}^{1/2}$

## 2.3 Results and Discussion

The solvated form of compound Be-BTB was obtained as colorless block-shaped crystals by heating a solution of beryllium nitrate and 1,3,5-benzenetribenzoic acid ($H_3BTB$) in a mixture of DMSO, DMF, and water at 130 °C for an extended period of 10 days. X-ray analysis of an evacuated single crystal revealed a highly porous network structure consisting of $[Be_{12}(OH)_{12}]^{12+}$ rings connected through the tritopic $BTB^{3-}$ ligands (see Figure 2.1). The saddle-shaped ring unit displayed in Figure 2.2 is composed of tetrahedrally coordinated $Be^{2+}$ ions linked around the

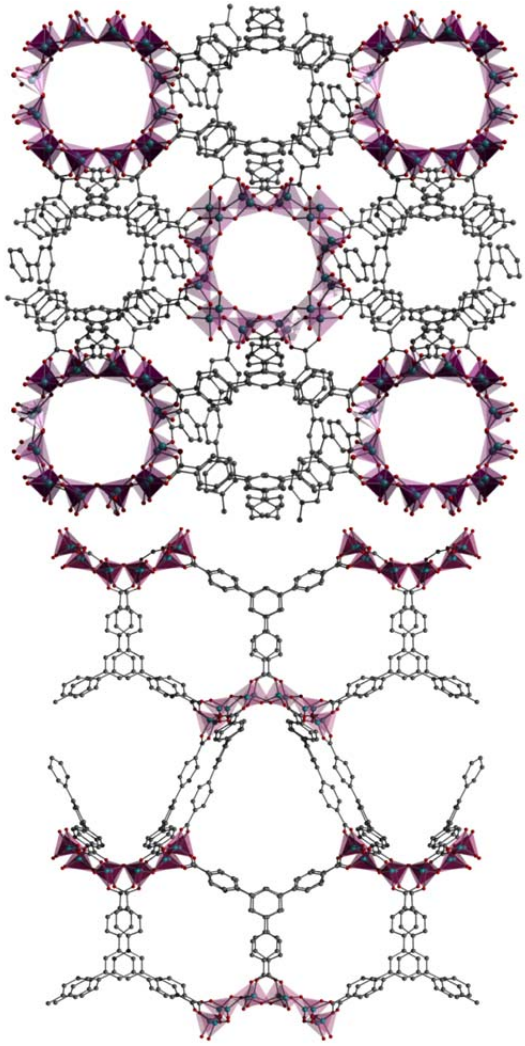

***Figure 2.1.*** A portion of the crystal structure of $Be_{12}(OH)_{12}(BTB)_4$ (Be-BTB), as viewed down the [001] (upper) and [010] (lower) directions. Turquoise, gray, and red spheres represent Be, C, and O atoms, respectively, while purple tetrahedra highlight the $BeO_4$ units; H atoms are omitted for clarity. Selected interatomic distances (Å) and angles (deg): Be-$O_{OH}$ 1.485(3)-1.662(2), Be-$O_{BTB}$ 1.561(2)-1.721(2), Be-$O_{OH}$-Be 114.7(1)-123.9(1), $O_{OH}$-Be-$O_{BTB}$ 105.0(1)-117.1(1), $O_{BTB}$-Be-$O_{BTB}$ 101.6(1)-107.7(2), Be-O-C 122.4(1)-129.8(1).

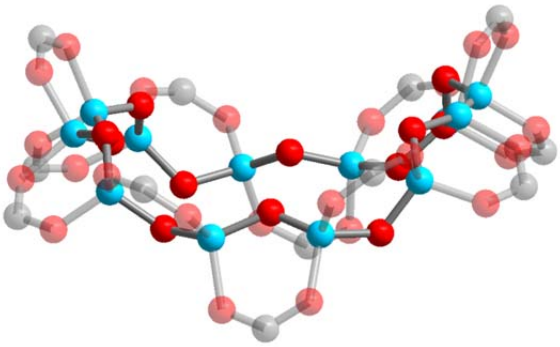

***Figure 2.2.*** The $[Be_{12}(OH)_{12}]^{12+}$ moiety as viewed from the side, with hydrogen atoms omitted, and faded peripheral carboxylate groups, for clarity. Turquoise, grey and red spheres represent Be, C, and O atoms, respectively.

inside edge via bridging hydroxide anions and around the periphery via bridging benzoate groups. These rings are observed every 27 Å along the [001] direction in the structure and reside on a $\bar{4}$ symmetry site. Each benzoate group is disposed approximately 90° to its neighboring benzoate groups, alternating in an up and down fashion around the ring. To the best of our knowledge, this twelve-metal ring structure is without precedent in beryllium chemistry, or indeed in any other metal-carboxylate chemistry.

The overall network structure of Be-BTB consists of an unprecedented 3,12 net, in which 12-connected $[Be_{12}(OH)_{12}]^{12+}$ ring nodes are linked through 3-connected $BTB^{3-}$ ligand nodes. The resulting framework contains large pear-shaped cavities that are approximately 27 Å along their long axis and 21 Å in diameter at the widest portion of their base. These pores can be accessed through three different types of openings: $[Be_{12}(OH)_{12}]^{12+}$ rings with a diameter of ca. 6 Å (based on van der Waals radii), 7 Å wide hexagonal rings formed by two $BTB^{3-}$ ligands and two $[Be_2(OH)]^{3+}$ segments, and larger 14 × 9 $Å^2$ arrow head-shaped rings involving three $BTB^{3-}$ ligands, two $Be^{2+}$ ions, and a $[Be_2(OH)]^{3+}$ segment. The solvent-accessible volume calculated from the crystal structure using the PLATON routine[8] is 77%, highlighting the extremely porous nature of the framework.

Low-pressure $N_2$ adsorption measurements performed on 1 at 77 K afforded a Type I isotherm characteristic of a microporous solid. Fits to the data gave a BET surface area of 4030 $m^2/g$ and a Langmuir surface area of 4400 $m^2/g$. These values lie slightly above the accessible surface area of 3600 $m^2/g$ calculated from the crystal structure,[13] indicating complete evacuation of the pores. Although the BET surface area of 1 exceeds the 3800 $m^2/g$ observed for MOF-5, it is still somewhat below that obtained for $Zn_4O(BTB)_2$ (MOF-177; 4750 $m^2/g$)[1d] and at least two other frameworks with larger pore openings.[1g,14] Nevertheless, it represents the highest value yet reported for a main group metal-organic framework or covalent organic framework.

The low-pressure $H_2$ adsorption isotherms for 1 at 77 and 87 K are shown in Figure 2.3. The total $H_2$ uptake of 1.6 wt % at 77 K and 1 bar is completely reversible, and the gradual rise of the isotherm indicates a small adsorption enthalpy. Indeed, as shown in Figure 2.4, a fit to the data yields an initial isosteric heat of adsorption of –5.5 kJ/mol, which gradually decreases with loading. Hence, the $[Be_{12}(OH)_{12}]^{12+}$ rings do not serve as strong binding sites for $H_2$, resulting in a flat adsorption profile. Note that this behavior is actually favorable for a cryogenic storage

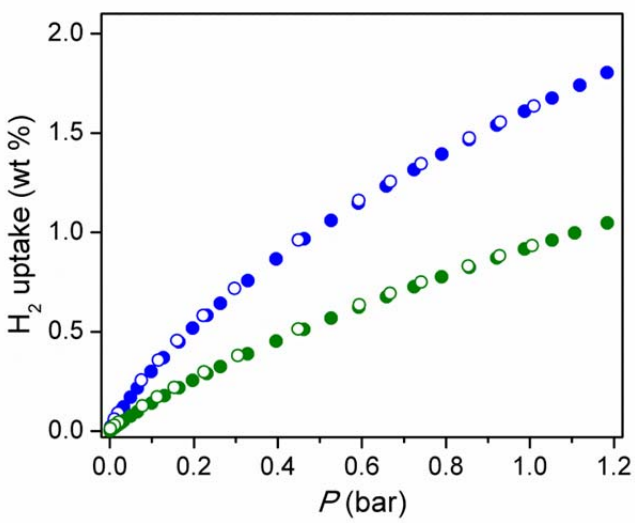


***Figure 2.3.*** Low-pressure region of the $H_2$ adsorption isotherms of Be-BTB recorded at 77 K (blue) and 87 K (green), with filled and open symbols representing adsorption and desorption data, respectively.

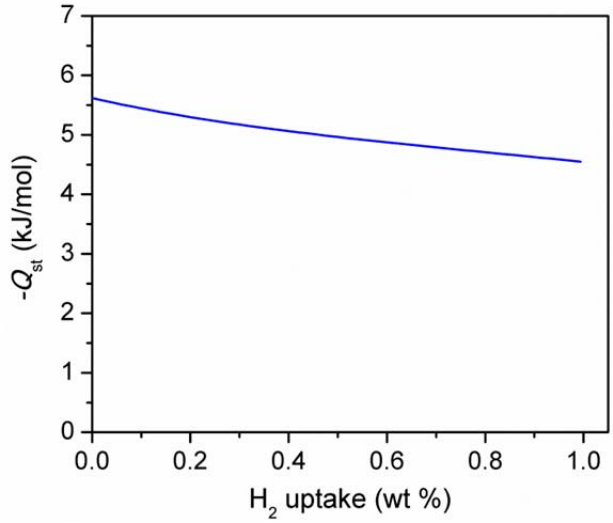


***Figure 2.4.*** Isosteric heat of adsorption for Be-BTB calculated from a virial-type fitting to the low-pressure $H_2$ adsorption data.

material, since operation of the fuel cell at pressures above 1.5 bar means that $H_2$ retained at lower pressures would not ordinarily be utilized.

Consistent with its high surface area, compound Be-BTB shows excellent performance as a hydrogen storage material at higher pressures (see Figure 2.5). At 77 K, the excess $H_2$ uptake reaches a maximum of 6.0 wt % at 20 bar, while the total uptake climbs to 9.2 wt % and 43 g/L at 100 bar. Although these capacities are among the highest recorded to date for a metal-organic framework,[1h] the volumetric storage density is still considerably below the 66 g/L achieved in MOF-5.[3] This is due to the larger pores of Be-BTB, wherein a significant amount of $H_2$ gas can reside far from the influence of the framework walls. Interestingly, while the $H_2$ storage capacity is dramatically reduced at 298 K, reaching 2.3 wt % and 11 g/L at 95 bar, the combined values are arguably better than those of any other metal-organic framework. To our knowledge, only

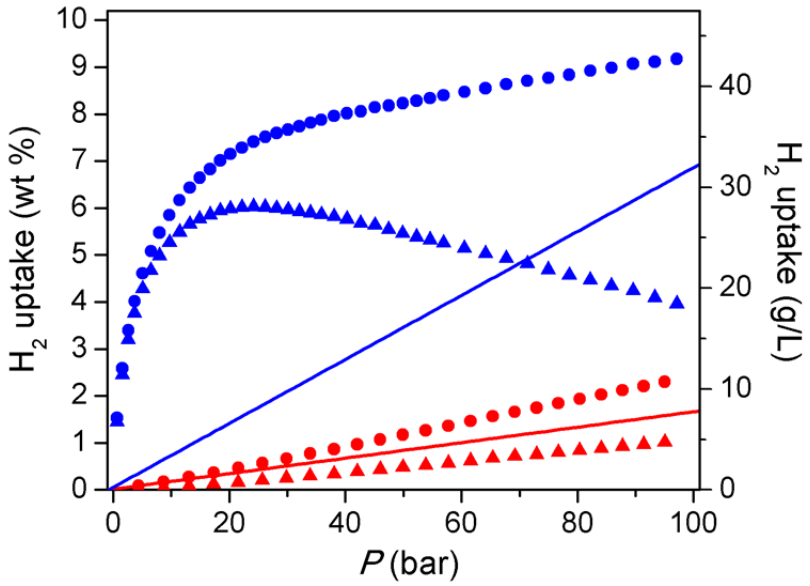


***Figure 2.5.*** Higher-pressure $H_2$ uptake in Be-BTB measured at 77 K (blue) and 298 K (red). Triangles and circles represent excess and total $H_2$ uptake, respectively, while the solid lines show the density of pure $H_2$.

$Mn_3[(Mn_4Cl)_3(BTT)_8(MeOH)_{10}]_2$ ($BTT^{3-}$ = 1,3,5-benzenetristetrazolate), which possesses open metal coordination sites, has a higher volumetric capacity of 12 g/L at 90 bar and 298 K, although its gravimetric uptake is just 1.5 wt %.[15] Here, the relatively good performance of Be-BTB is likely a consequence of its structure, which contains many rings near the 7 Å diameter calculated as ideal for achieving a high storage density at 298 K.[16]

## 2.4 Outlook

The foregoing results demonstrate reaction conditions under which the first pure, crystalline beryllium-based metal-organic framework could be isolated. It is likely that similar conditions may now supply a range of new beryllium-based frameworks exhibiting exceptionally high surface areas. In particular, the use of 1,4-benzenedicarboxylate as a linker can be expected to afford frameworks with pore sizes near the 10 Å diameter sought for high-density hydrogen storage at cryogenic temperatures.[16]

## 2.5 Acknowledgments

This research was funded by DoE Grant DE-FG36-05GO15002. I thank Fulbright New Zealand for partial financial support, and Dr. A. DiPasquale, Dr. F. Hollander, Prof. S. Batten, and Prof. T. Düren for helpful discussions.

## 2.6 References and Notes

(1) (a) Eddaoudi, M.; Kim, J.; Rosi, N.; Vodak, D.; Wachter, J.; O'Keeffe, M.; Yaghi, O. M. *Science* **2002**, *295*, 469. (b) Matsuda, R.; Kitaura, R.; Kitagawa, S.; Kubota, Y.; Belosludov, R. V.; Kobayashi, T. C.; Sakamoto, H.; Chiba, T.; Takata, M.; Kawazoe, Y.; Mita, Y.

*Nature* **2005**, *436*, 238. (c) Millward, A. R.; Yaghi, O. M. *J. Am. Chem. Soc.* **2005**, *127*, 17998. (d) Furukawa, H.; Miller, M. A.; Yaghi, O. M. *J. Mater. Chem.* **2007**, *17*, 3197. (e) Ma, S.; Sun, D.; Simmons, J. M.; Collier, C. D.; Yuan, D.; Zhou, H. C. *J. Am. Chem. Soc.* **2008**, *130*, 1012. (f) Morris, R. E.; Wheatley, P. S. *Angew. Chem. Int. Ed.* **2008**, *47*, 4966. (g) Llewellyn, P. L.; Bourrelly, S.; Serre, C.; Vimont, A.; Daturi, M.; Hamon, L.; De Weireld, G.; Chang, J.-S.; Hong, D.-Y.; Hwang, Y. K.; Jhung, S. H.; Férey, G. *Langmuir* **2008**, *24*, 7245. (h) Murray, L. J.; Dinca, M.; Long. J. R. *Chem. Soc. Rev.* **2009**, *38*, 1294 and references therein.

(2) (a) Aceves, S. M.; Berry, G. D.; Martinez-Frias, J.; Espinosa-Loza, F. *Int. J. Hydrogen Storage* **2006**, *31*, 2274. (b) Kumar, V. S.; Raghunathan, K.; Kumar, S. *Int. J. Hydrogen Storage* **2009**, *34*, 5466.

(3) Kaye, S. S.; Dailly, A.; Yaghi, O. M.; Long, J. R. *J. Am. Chem. Soc.* **2007**, *129*, 14176.

(4) (a) Férey, G.; Latroche, M.; Serre, C.; Millange, F.; Loiseau, T.; Percheron-Guégan, A. *Chem. Commun.* **2003**, 2976. (b) Dinca, M.; Long. J. R. *J. Am. Chem. Soc.* **2005**, *127*, 9376. (c) Caskey, S. R.; Wong-Foy, A. G.; Matzger, A. J. *J. Am. Chem. Soc.* **2008**, *130*, 10870. (d) Senkovska, I.; Hoffmann, F.; Froba, M.; Getzschmann, J.; Bohlmann, W.; Kaskel, S. *Microporous Mesoporous Mater.* **2009**, *122*, 93. (e) Furukawa, H.; Yaghi, O. M. *J. Am. Chem. Soc.* **2009**, *131*, 8879. (f) Ahnfeldt, T.; Guillou, N.; Gunzelmann, D.; Margiolaki, I.; Loiseau, T.; Férey, G.; Senker, J.; Stock, N. *Angew. Chem. Int. Ed.* **2009**, *48*, 5163.

(5) Note that carboxylate-terminated tetrahedral $[Be_4O]^{6+}$ units have long been known as molecular species: (a) Bragg, W. H. *Nature*, **1923**, *111*, 532. (b) Pauling, L.; Sherman, J. *Proc. Nat. Acad. Sci. USA* **1934**, *20*, 340.

(6) (a) Han, S. S.; Deng, W.-Q.; Goddard, W. A. *Angew. Chem. Int. Ed.* **2007**, *46*, 6289. (b) Babarao, R.; Jiang, J. *Langmuir* **2008**, *24*, 6270.

(7) (a) Tanatar, S.; Kurowski, E. *J. Rus. Phys. Chem. Soc.* **1907**, *39*, 936. (b) Meyer, J.; Mantel, E. *Z. Anorg. Allg. Chem.* **1922**, *123*, 43. (c) Marvel, C. S.; Martin, M. M. *J. Am. Chem. Soc.* **1958**, *80*, 619.

(8) Spek, A. L. *J. Appl. Crystallogr.* **2003**, *36*, 7.

(9) Accessible Surface Area Calculation Program, http://www.see.ed.ac.uk/~tduren/research/surface_area/, (accessed August 2009).

(10) Rappe, A. K.; Casewit, C. J.; Colwell, K. S.; Goddard, W. A.; Skiff, W. M. *J. Am. Chem. Soc.* **1992**, *114*, 10024.

(11) Download, instructions, and further details on the use and capabilities of this software package area available online at http://www.r-project.org.

(12) Lemmon, E. W.; McLinden, M. O.; Friend, D. G. Thermophysical Properties of Fluid Systems. In *NIST Chemistry WebBook, NIST Standard Reference Database Number 69*; Linstrom, P. J., Mallard, W. G., Eds.; National Institute of Standards and Technology, Gaithersburg MD; http://webbook.nist.gov (retrieved August 26, 2009).

(13) Düren, T.; Millange, F.; Férey, G.; Walton, K. S.; Snurr, R. Q. *J. Phys. Chem. C* **2007**, *111*, 15350.

(14) Koh, K.; Wong-Foy, A. G.; Matzger, A. J. *J. Am. Chem. Soc.* **2009**, *131*, 4184.

(15) Dinca, M.; Long, J. R. *J. Am. Chem. Soc.* **2007**, *129*, 11172.

(16) Rzepka, M.; Lamp, P.; de la Casa-Lillo, M. A. *J. Phys. Chem. B* **1998**, *102*, 10894.

# Chapter 3: Hydrogen Storage and Carbon Dioxide Capture in an Iron-Based Sodalite-Type Metal–Organic Framework (Fe-BTT) Discovered *via* High-Throughput Methods

## 3.1 Introduction

Metal–organic frameworks have recently come under intense investigation for gas storage and separation applications, owing to their high internal surface areas, convenient modular synthesis, and chemical tunability.[1] In the area of cryogenic hydrogen storage, gravimetric and/or volumetric capacities that approach the U.S. Department of Energy targets[2] for mobile hydrogen storage systems have been demonstrated within the highest-surface area materials.[1e,3] However, at room temperature, these materials typically exhibit little or no improvement over the density of pure compressed hydrogen gas as a result of the weak dispersion-type (physisorptive) interactions that predominate as the mode of gas uptake. Indeed, the isosteric heat of adsorption within these materials usually lies within a range of –5 to –7 kJ/mol, which is far below the estimated optimal value of ca. –15 kJ/mol for storage at 298 K.[1j,4] This value applies to the whole adsorption range for an adsorbent operating between 1.5 and 100 bar, highlighting the need for materials that not only possess binding sites of the appropriate adsorption enthalpy, but also have a high concentration of these sites in order to maximize the quantity of usable hydrogen.

One strategy for improving the room temperature hydrogen storage performance of metal–organic frameworks is through the generation of exposed metal cation sites on the framework surface.[5,6] Previously, we have reported a number of metal-organic frameworks in which removal of a solvent molecule from the coordination sphere of the framework metal cations yields strong adsorption sites for $H_2$. Indeed, zero-coverage isosteric heats of $H_2$ adsorption of –10.1 and –9.5 kJ/mol were observed in the cubic sodalite-type frameworks $Mn_3[(Mn_4Cl)_3(BTT)_8(MeOH)_{10}]_2$ (Mn-BTT, $BTT^{3-}$ = 1,3,5-benzenetristetrazolate)[5f] and $HCu[(Cu_4Cl)_3(BTT)_8]\cdot 3.5HCl$ (Cu-BTT),[5h] which remarkably retain their structures upon desolvation. One possibility for improving the isosteric heat of adsorption within this structure type would be through the replacement of the $Mn^{2+}$ or $Cu^{2+}$ ions in the structure with $M^{2+}$ cations having a smaller radius. The greater charge density of the exposed metal cations on the framework surface should then be more effective at inducing a dipole in $H_2$, leading to stronger binding. Metal–organic frameworks with unsaturated metal cation sites are also of potential utility as separation materials for the capture of $CO_2$ from flue gas streams.[5j,7] While some frameworks have been shown to have tremendous capacities for $CO_2$ at high pressures,[1d,i] most of these materials exhibit low uptake in the pressure region of interest of 0.1–0.2 bar for flue gas separations. Perhaps most importantly, for a framework to be viable as a separation material, a high selectivity for $CO_2$ over the other components of the gas stream, primarily $N_2$, is required. Exposed metal cations can provide polarizing sites that interact selectively with $CO_2$, which has a greater polarizability than $N_2$. Thus, tuning of the pore surface charge through variation of the metal cation may be one route toward optimized $CO_2$ capture materials that exhibit reversible capture at minimal energy cost. From a fundamental perspective, systematic studies of the gas sorption properties of isostructural materials containing unsaturated coordination sites are currently limited to a small number of systems, such as $M_2$(DOBDC) (M = Mg, Mn, Co, Ni, Zn; $H_4$DOBDC = 2,5-dihydroxyterephthalic acid).[5j,7,8] The study of a larger number of systems is needed in order to understand more fully the effects of metal substitution on crucial gas

adsorption properties, such as the isosteric heat of adsorption for $H_2$, or the separation factor for $CO_2$ over $N_2$. Moreover, the extent to which other metal cations can adopt the Mn- and Cu-BTT structure type is currently unknown, which prompted our attempts to expand the library of these materials. While a number of $Fe^{3+}$-based porous metal–organic frameworks have been reported to date,[9] the preparation of the $Fe^{2+}$-based frameworks has been relatively rare.[10] Most importantly, to our knowledge, no compounds with accessible, open $Fe^{2+}$ coordination sites have been studied for gas adsorption. Herein, we report the synthesis and characterization of the iron-based sodalite-type metal-organic framework $Fe_3[(Fe_4Cl)_3(BTT)_8(MeOH)_4]_2$ (Fe-BTT), in which exposed $Fe^{2+}$ cations indeed serve as strong adsorption sites for $H_2$ and $CO_2$.

### 3.2 High-Throughput Methodology

The modular synthesis of metal–organic frameworks, wherein a metal salt and an organic bridging ligand are combined under solventothermal conditions, is a tremendously versatile approach for the discovery of new materials. While convenient, the optimal synthetic procedures affording a desired porous phase in pure crystalline form are frequently discovered only following the survey of a large number of reaction conditions. This is in part due to the considerable impact that subtle changes in the reaction parameters can have on the resulting products. Indeed, for a given combination of metal salt and bridging ligand, numerous different crystalline phases are often possible. Furthermore, the undesired side-products are frequently extended network solids that are insoluble in organic solvents, and prove to be inseparable from the desired phase by conventional solution techniques. Thus, the identification and optimization of the synthetic conditions for a new metal–organic framework typically involves the systematic variation of many reaction parameters, including the metal salt, metal-to-ligand ratio, solvent composition, acid/base content, reaction temperature, and reaction time.

A thorough survey of so many different reaction parameters means that the total number of screening reactions quickly becomes unwieldy. In such cases, high-throughput methodologies, which have been successfully implemented in the synthesis and characterization of a variety of inorganic materials,[11] are of potential benefit. In fact, very recently, a number of metal-organic framework systems have been studied by high-throughput approaches, showing that the development of solventothermal syntheses of this class of materials can be well-suited to automated methods.[9b,12]

The high-throughput methodology employed in this work was performed using an automated solid- and liquid-dispensing robotic module mounted within a glove box under a dinitrogen atmosphere. The system allows rapid dispensing of reagents and solvents into individual reaction vials (1, 2, 4, 8, or 20 mL capacity), and depending on the vial size, up to 96 reactions can be performed on a single vial plate. The composition of each reaction mixture is programmed through a computer interface, that also allows the experimental variables, such as reaction temperature, ramping and cooling rate, and reaction time, to be precisely set and monitored. Once the individual reactions are prepared and sealed, the synthesis is performed under static conditions on the robot deck. The product formed within each reaction vial can be imaged using a camera installed on the robot deck, allowing for rapid identification of the reaction conditions leading to sizable single crystals. Additionally, the solids precipitated within each reaction vial can be isolated and automatically dispensed onto a glass plate for high-throughput powder X-ray diffraction measurements. The experimental data, such as the actual

quantities of reagents dispensed, powder X-ray diffraction patterns, and image data, are collectively recorded within a centralized database for analysis and comparison.

The following section describes the optimized synthesis and characterization of Fe-BTT. Note that although this iron-based metal–organic framework is isostructural with Mn- and Cu-BTT, a large number of screening reactions were required in order to obtain the material in pure form. Significantly, initial attempts to synthesize Fe-BTT using reaction conditions similar to those under which the other analogues could be prepared proved unsuccessful. Thus, the optimized conditions were developed following successive refinements of the reaction parameters using small-scale reactions (typically 1 or 2 mL-scale reactions). Most importantly, the resulting optimized conditions were vastly different from those for Mn-BTT and Cu-BTT, highlighting the benefit of systematic combinatorial screening performed using an automated high-throughput system.

### 3.3 Experimental Section

Unless otherwise stated, all manipulations were performed under an inert dinitrogen or helium atmosphere. 1,3,5-Tris(2*H*-tetrazol-5-yl)benzene hydrochloride ($H_3BTT{\cdot}2HCl$) was prepared according to the literature procedure.[5f] All other reagents were obtained from commercial vendors and used without further purification. ***Caution***. Tetrazolate compounds are potentially explosive, and should be handled with care. While we did not encounter any difficulties in handling the free ligand $H_3BTT{\cdot}2HCl$ or the frameworks derived therein, care should be taken to avoid generating sparks or creating friction on the material. In particular, a teflon-lined spatula should be used when handling the desolvated form of Fe-BTT.

**$Fe_3[(Fe_4Cl)_3(btt)_8]_2{\cdot}22DMF{\cdot}32DMSO{\cdot}11H_2O$ (solvated Fe-BTT).** Anhydrous ferrous chloride (76 mg, 0.59 mmol), $H_3BTT{\cdot}2HCl$ (58 mg, 0.20 mmol), DMF (5 mL), and DMSO (5 mL) were added to a 20 mL scintillation vial, and the vial was tightly sealed with a teflon-lined cap. The reaction mixture was heated on a hotplate at 110 °C for 24 h, after which time small, pale yellow crystals were formed on the vial walls. The solid was filtered and washed with DMF, and isolated as a pale yellow-green solid (42 mg, 32%). IR (neat): 3391 (m br), 3002 (w), 2920 (w), 1654 (s), 1498 (w), 1435 (m), 1412 (s), 1389 (m), 1314 (w), 1253 (w), 1227 (w), 1194 (w), 1102 (w), 1014 (s), 951 (s), 904 (m), 788 (s), 749 (m), 661 (w). Anal. Calcd for $C_{274}H_{416}Cl_6Fe_{27}N_{214}O_{65}S_{32}$: C, 31.36; H, 4.00; N, 28.56. Found: C, 31.19; H, 4.05; N, 28.32. The solvent composition was deduced using a combination of elemental analysis data and thermogravimetric analysis. The DMF-solvated framework was generated by suspending **1** within DMF at 80 °C for 24 h, with exchanging of the solvent for fresh DMF each 8 h. IR (neat): 3178 (br s), 2927 (m), 2857 (m), 1656 (s) 1498 (m), 1437 (m), 1408 (s), 1385 (s), 1254 (m), 1090 (s), 1062 (m), 951 (w), 907 (w), 865 (w), 788 (m), 749 (w), 696 (w), 678 (w), 658 (s). The methanol-solvated framework was generated by suspending the DMF-solvated material in MeOH at 100 °C for 48 h, exchanging the solvent for fresh MeOH each 8 h. IR (neat): 3178 (br s), 2943 (m), 2831 (m), 1416 (s), 1231 (w), 1194 (w), 1133 (w), 1069 (w), 1012 (s), 902 (w), 789 (s), 750 (m), 688 (w), 645 (w). The sample is air- and moisture-sensitive, and was stored in a solvent-free glove box under dinitrogen.

**High-Throughput Experiments.** High-throughput experiments were performed using a robotic Symyx Core Module System equipped with powder- and liquid-dispensing functionality. The recipes for the screening reactions were programmed from a client computer terminal using Symyx Library Studio version 7.1.7.14, and the automated dispensing protocols were executed

through Symyx Automation Studio version 1.1.1.8. These client-side software applications communicate to the Core Module through a central server, which maintains a database containing all experimental parameters. The Core Module is loaded within a Braun glovebox under a dinitrogen atmosphere, and the pneumatic valves were operated using a dinitrogen supply with a pressure maintained at 80 psi.

Powder dispensing was performed by loading finely-ground metal salts and ligands into plastic powder-dispensing hoppers. The solid was dispensed by automatic transfer of the individual vials onto a Sartorius LP 1200.S balance on the Core Module deck with a measurement error of less than 0.1 mg. Stability of the balance was achieved through sealing of the balance headspace using a polymer membrane with a circular opening that allows for lowering of the powder hopper to a position just above the aperture of the vial. Following taring of the weight of the empty vial, the appropriate quantity of solid was dispensed by the robot arm. The discrepancy between the mass dispensed and the programmed mass was typically within 2%.

Liquid dispensing was achieved by firstly placing vials filled with neat solvents on the robot deck in positions as input in the Automation Studio protocol. The vials were sealed with scepta to avoid cross-contamination or evaporation of the solvents. The liquids were aspirated through a needle that is located on the right arm, and is connected to a series of three syringe pumps with volumes of 0.5 mL, 3 mL, and 5 mL, respectively. The syringe used depended upon the quantity of the liquid to be dispensed. Once the liquid is aspirated, the needle is moved to the appropriate vials through movements of the right arm. The protocol was such that the needle was thoroughly washed with methylene chloride following each solvent, to avoid cross-contamination.

Automated dispensing of the products onto glass plates for powder X-ray analysis was achieved by a protocol that firstly aspirates the mother liquid from the reaction product, and replenishes it with fresh DMF. This procedure was repeated three times, followed by a similar washing procedure using methylene chloride. The crystals were then pulverized using the automated shaker system on the robot deck with small ball bearings, and the resulting slurry was dispensed into individual wells of a crystallizer block attached to a glass plate. The methylene chloride was then allowed to evaporate, and the crystallizer block was removed from the glass plate. The plate was then mounted onto a metal frame, and subsequently transferred to the high-throughput powder diffractometer.

**X-ray Structure Determination.** A block-shaped single-crystal of solvated Fe-BTT (0.1 mm × 0.1 mm × 0.1 mm) was coated in Paratone-N oil, attached to a Kapton loop, and mounted on a Bruker X8 APEX diffractometer equipped with a Bruker MICROSTAR Cu rotating anode X-ray source. The sample was cooled to 100 K under a stream of nitrogen, and preliminary cell data were obtained to yield a cubic Laue group. A full hemisphere of data was collected over a period of 24 h, after which time the crystal showed no significant decomposition or structural distortion. Data were integrated and corrected for Lorentz, polarization, and absorption effects within the APEX 2 software package. Crystal and refinement parameters are listed in Table 3.1. Space group determinations were made based on systematic absences, *E* statistics, and successful refinement of the structure. The structure solution was obtained using direct methods and the SHELXS-97 software, and expanded through successive difference Fourier maps. Thermal parameters for all non-hydrogen atoms were refined anisotropically, and hydrogen atoms were assigned to ideal positions using the appropriate AFIX commands. Complete modeling of the solvent within the pores was not possible due to disorder, hence the electron density within the cavities was masked using the SQUEEZE routine within the PLATON software package.[13]

**Accessible Surface Area Calculation.** The source code for the accessible surface area calculation program was obtained free of charge from the Internet.[14] The crystallographic information file (CIF) obtained from the single crystal X-ray structure was converted to the XYZ file format using Mercury CSD 2.0. The XYZ file and UFF force field atomic parameters[15] were used as input for the simulation (atomic diameters (Å): H 2.571, C 3.431, N 3.260, O 3.118, Fe 2.594, Cl 3.516), and the accessible surface area was evaluated using a dinitrogen-sized probe molecule (diameter = 3.681 Å) inserted at randomized points in the unit cell, and averaging the resultant individual accessible surface area values after 5000 trials.

**Mössbauer Spectroscopy.** The Mössbauer spectrum of Fe-BTT was measured at various temperatures between 10 and 295 K in a Janis Supervaritemp cryostat with a constant-acceleration spectrometer which utilized a rhodium matrix cobalt-57 source, and was calibrated at 295 K with $\alpha$-iron powder. The absorber contained 32 mg/cm$^2$ of powder mixed with boron nitride. The absorber was prepared and inserted into the cryostat under dry dinitrogen. The relative statistical errors associated with the isomer shifts, quadrupole splittings, line widths, percent areas, and absolute areas measured between 10 to 225 K was ±0.005, ±0.01, ±0.01 mm/s, 0.2 %, and 0.3 (%$\varepsilon$)(mm/s), respectively; these statistical errors are approximately twice as large between 260 and 295 K. The absolute errors of these parameters were approximately twice the statistical errors.

**Powder Neutron Diffraction Experiments.** Neutron powder diffraction data were collected on the High Resolution Neutron Powder Diffractometer BT-1 at the NIST Center for Neutron Research (NCNR) with a Ge-(311) monochromator and using in-pile collimation of 15 min of arc, corresponding to a wavelength of 2.0787 Å. Measurements were taken as a function of deuterium loading at a temperature of 4 K with measurement times of ca. 9 h for the bare framework and $D_2$ loadings of 4.1, 8.0 $D_2$ molecules per formula unit, and ca. 5 h for all higher $D_2$ loadings.

All sample transfers were performed in a helium-filled glovebox equipped with water and oxygen monitors. Initial sample activation was performed in a glass tube with a packless bellows valve attached. The sample was evacuated using a turbomolecular pump ($10^{-5}$ Torr) and heated to 135 °C with a ramp speed of ca. 0.5 °C per minute. After degassing at 135 °C for 16 h, the sample was cooled and transferred to a cylindrical vanadium can (i.d. 0.95 cm) equipped with a capillary gas line and a packless valve, and sealed with a lead O-ring. The sample was mounted onto a sample stick equipped with a stainless-steel gas line with an additional valve for a top-loading closed-cycle helium refrigerator. The sample was further degassed in situ for ca. 20 min under high vacuum. During the experiments, a known amount of hydrogen (deuterium) gas was loaded into the sample (813 mg), which was maintained at a temperature of 60 K until no pressure drop was observed for at least 1 min. The sample was then cooled down to the base temperature of 3.5 K over a period of 1 h in order to perform measurements. In all cases, the outgas pressure reading was zero well before reaching 25 K.

A diffraction pattern was collected for Fe-BTT prior to dosing with $D_2$. Subsequent Rietveld analysis indicated the existence of extra neutron density close to the $Fe^{2+}$ ions in the framework skeleton, as expected due to the presence of residual methanol molecules. Accordingly, the extra neutron density was modeled using a partial occupancy of methanol O and C atoms, and this corrected "bare" model was used as a baseline for all subsequent measurements involving $D_2$. A significant quantity of nuclear density was observed in a position approximately 4.23 Å above the chloride ion, which could be modeled as extraframework Fe atoms with the correct occupancy to fulfill charge balance of the anionic framework.

Neutron scattering diffraction patterns were analyzed using the Rietveld refinement method. The program EXPGUI incorporating the Rietveld program GSAS[16] was used to perform all refinements. The model of the bare material was refined first, and it was used as the starting point for subsequent refinements of the $D_2$-loaded samples. Deuterium molecules are treated as point scatters with double occupancy since they are expected to be quantum mechanically averaged in the ground state. As mentioned, during the refinement of the model for the bare material, extra C and O atoms were introduced to account for the scattering intensities from the residual methanol molecules bound to the intraframework $Fe^{2+}$ ions. The information on the extra atoms was obtained from the diffraction pattern of the bare material and was fixed at these values when analyzing the cases with deuterium molecules loaded. The coordinates of all other atoms and the Debye-Waller factors were allowed to vary during the refinement of each deuterium loading case. Based on the structure obtained from the diffraction pattern of the bare material, the diffraction patterns of the first $D_2$-loaded case (4 $D_2$ molecules/formula unit) was analyzed by firstly neglecting the $D_2$ molecules. The Fourier difference maps were calculated, clearly indicating the positions of $D_2$ adsorption sites. Accurate values for the $D_2$ locations and occupancy numbers were then obtained by Rietveld refinement. For each successive $D_2$ loading, the Fourier difference map was calculated on the basis of the results of the previous $D_2$ loading and used to identify new $D_2$ adsorption sites.

**Inelastic Neutron Scattering Experiments.** Inelastic neutron scattering data were collected on the Filter Analyzer Neutron Spectrometer (FANS) BT-4 at the NCNR. The same sample can from the diffraction experiment was used and was cooled in the same manner as the neutron diffraction experiments.

**Low-Pressure Gas Sorption Measurements.** Glass sample tubes of a known weight were loaded with approximately 200 mg of sample, and sealed using a TranSeal. Samples were degassed at 135 °C for 24 h on a Micromeritics ASAP 2020 analyzer until the outgas rate was no more than 1 mTorr/min. The degassed sample and sample tube were weighed precisely and then transferred back to the analyzer (with the TranSeal preventing exposure of the sample to the air after degassing). The outgas rate was again confirmed to be less than 1 mTorr/min. Adsorption isotherms were measured at 77 K in a liquid nitrogen bath for $H_2$ and $N_2$, and at 87 K in a liquid argon bath for $H_2$.

**High-Pressure Gas Sorption Measurements.** In a typical measurement, at least 200 mg of sample was loaded in a sample holder in a glove box under an argon atmosphere. The sample was evacuated at 130 °C for 10 h under a pressure of less than $10^{-5}$ torr. Hydrogen excess adsorption measurements were performed on an automated Sieverts' apparatus (PCTPro-2000 from Hy-Energy Scientific Instruments LLC) over a pressure range of 0-100 bar. UHP-grade hydrogen and helium (99.999% purity) were used for all measurements. Volumetric measurements at 77 K were carried out by submerging the sample holder in a liquid nitrogen bath, for which the fill-level was maintained constant throughout the experiment. The total gravimetric and volumetric adsorption was calculated as described in Chapter 2.2.

**Other Physical Measurements.** Powder X-ray diffraction patterns were obtained on a Bruker D8 Advance diffractometer with a Cu anode ($\lambda$ = 1.5406 Å), or in the case of the high-throughput experiments a Bruker D8 Discover with GADDS. Infrared spectra were obtained on a Perkin-Elmer Spectrum 100 Optica FTIR spectrometer furnished with an attenuated total reflectance accessory (ATR). Carbon, hydrogen, and nitrogen analyses were obtained from the Microanalytical Laboratory at the University of California, Berkeley. Thermogravimeteric

analyses (TGA) were performed on a TA Instruments TGA 5000 instrument at a ramp rate of 2 °C/min under a flow of nitrogen.

***Table 3.1.*** Crystallographic parameters for the crystal structure of Fe-BTT.

| Crystallographic Parameter | Observed Value |
|---|---|
| Formula | $C_{12}H_4Cl_{0.5}Fe_2N_{16}O_2$ |
| FW | 533.74 |
| $T$, K | 100(2) |
| Wavelength, Å | 1.54178 |
| Crystal system, space group | Cubic, $Pm$–3$m$ |
| Z | 6 |
| $a$, Å | 18.8235(11) |
| $V$, Å$^3$ | 6669.6(7) |
| $d_{calc}$, g/cm$^3$ | 0.797 |
| Absorption coefficient, mm$^{-1}$ | 5.719 |
| $F$(000) | 1587 |
| Crystal size, mm$^3$ | 0.10 × 0.10 × 0.10 |
| Theta range for data collection | 2.35-65.41 |
| Index range | $-20 \leq h \leq 20$, $-21 \leq k \leq 22$, $-14 \leq l \leq 20$ |
| Reflections collected | 22659 |
| Independent reflections | 1207 |
| Data/restraints/parameters | 1207 / 0 / 47 |
| GOF on $F^2$ | 1.075 |
| Largest diff. peak and hole, e·A$^{-3}$ | 0.60 and –0.26 |
| $R_1$, [I>2σ(I)] | 3.53 |
| $R_1$($wR_2$)[a], all data | 3.72 (9.90) |

[a] $R_1 = \Sigma||F_o|-|F_c||/ \Sigma|F_o|$, $wR_2 = \{\Sigma[w(F_o^2-F_c^2)^2]/ \Sigma[w(F_o^2)^2]\}^{1/2}$

### 3.4 Results and Discussion

The reaction between $FeCl_2$ and $H_3BTT$ in a 3:1 mole ratio in a mixture of DMF and DMSO leads to the formation of $Fe_3[(Fe_4Cl)_3(BTT)_8]_2 \cdot 22DMF \cdot 32DMSO \cdot 11H_2O$ (solvated Fe-BTT) as pale-yellow cubic crystals. X-ray structural analysis of a single crystal revealed the expected porous cubic (space group: $Pm\bar{3}\,m$, $a$ = 8.8235(11) Å) framework structure consisting of chloride-centered $[Fe_4Cl]^{7+}$ square units connected via triangular $BTT^{3-}$ ligands to form a 3,8-net (Figure 3.1). Here, six $[Fe_4Cl]^{7+}$ fragments and eight $BTT^{3-}$ ligands combine to form a truncated octahedral, sodalite-like cage with an internal diameter of approximately 10.3 Å (based on van der Waals radii). Adjacent cages share square faces to form a cubic, anionic framework with a three-dimensional channel system with pore openings of approximately 9 Å in diameter. Despite significant residual electron density observed within the sodalite cages and in the channels of the framework, the X-ray data did not allow a clear determination of the location of the charge-balancing $Fe^{2+}$ cations within the pores of the solvated structure. However, their presence within the pores could be identified by Mössbauer spectroscopy (see below). Activation of Fe-BTT for gas adsorption experiments was performed by first exchanging the solvent molecules within the pores and bound to the $Fe^{2+}$ metal centers with methanol, followed by heating of the solid at 135 ºC under dynamic vacuum for 24 h. While the outgas rate after this

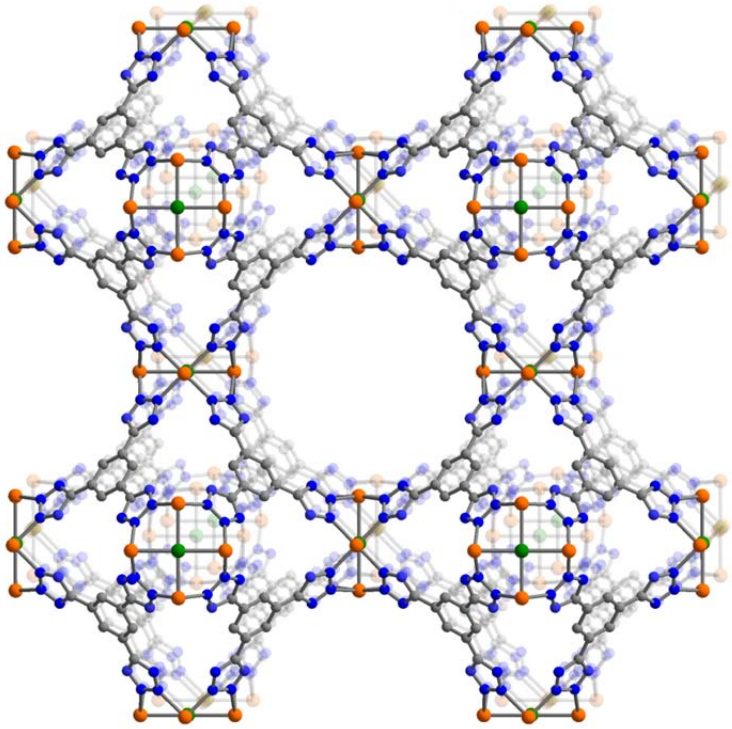

***Figure 3.1.*** A portion of the single-crystal X-ray structure of Fe-BTT. Orange, green, gray, and blue spheres represent Fe, Cl, C, and N atoms, respectively. Solvent molecules, H atoms, and charge-balancing cations are omitted for clarity. Selected interatomic distances (Å) and angles (°): Fe–Cl 2.649(1), Fe–N 2.132(2), Fe/Fe 3.746(2), Fe–Cl–Fe 90.0, N–Fe–N 87.4(1), 91.7(1), Fe–N–N 124.7(1), 125.6(1).

time was <2 mTorr/min, powder neutron diffraction data (discussed below) indicate that approximately 30% of the framework $Fe^{2+}$ centers retain a bound methanol molecule. The ensuing formulation of $Fe_3[(Fe_4Cl)_3(BTT)_8(MeOH)_4]_2$ for Fe-BTT is indeed consistent with elemental analysis and infrared spectroscopy. Unfortunately, attempts to utilize higher activation temperatures to remove all of the residual solvent resulted in decomposition of the framework. This observation is consistent with thermogravimetric analysis data for methanol-exchanged Fe-BTT, which display a rapid drop in mass above 150 ºC.

Low-pressure $N_2$ adsorption measurements performed on Fe-BTT at 77 K revealed a type-I adsorption isotherm characteristic of a microporous solid. Fits to the data yielded a BET surface area[17] of 2010 $m^2/g$, and a Langmuir surface area of 2200 $m^2/g$. These values are close to the accessible surface area of 2195 $m^2/g$ calculated from the fully-desolvated crystal structure.[18] Note that the BET surface area of Fe-BTT lies slightly below the corresponding value for Mn-BTT (2100 $m^2/g$) and above that obtained for Cu-BTT (1710 $m^2/g$). The differences correlate with the unit cell volumes of the three isostructures (Mn-BTT, 6985(1)$Å^3$; Fe-BTT, 6670(1) $Å^3$; Cu-BTT: 6430(4) $Å^3$). The unit cell volume is directly related to the ionic radii of the three metal ions (high-spin $Mn^{2+}$: 0.83 Å; $Fe^{2+}$: 0.78 Å; $Cu^{2+}$: 0.73 Å) and the resulting distances for the metal–chloride and metal–nitrogen bonds.

### 3.4.1 Mössbauer Spectra

The sample used for Mössbauer spectroscopy was prepared by immersing the as-synthesized form of Fe-BTT in DMF, thereby generating a material in which all of the DMSO and water molecules within the pores had been replaced by DMF molecules. Selected Mössbauer spectra of this sample obtained between 10 and 295 K are shown in Figure 3.2, and the corresponding hyperfine parameters are given in Table 3.2. The Mössbauer spectrum at 10 K was used to determine the optimal stoichiometry of the DMF-solvated material by identifying a component doublet, shown in red in Figure 3.2, that is assigned to $[Fe(DMF)_6]^{3+}$ complexes within the pores. The relative areas of the spectral components then lead to the formulation $[Fe^{III}(DMF)_6]_{0.63}[Fe^{II}(DMF)_6]_{0.56}[(Fe^{II}{}_4Cl)_3(BTT)_8]\cdot n$DMF. The relative areas of the spectral components were constrained to be consistent with this stoichiometry at all temperatures. Relaxation of this constraint led to at most minor changes in the relative areas. In these fits, the hyperfine parameters of the doublet assigned to $[Fe(DMF)_6]^{2+}$, shown in black in Figure 3.2, have been constrained to the parameters reported for $[Fe(DMF)_6](ClO_4)_2$ in the solid state.[19] Note that while the preparation of Fe-BTT utilized $Fe^{2+}$ ions, we envisage the origin of the $[Fe^{III}(DMF)_6]^{3+}$ signal to be a result of oxidation during sample work-up or transfer to the spectrometer.

The first unusual feature of the Mössbauer spectra is the broad nature of the spectral component associated with the $Fe^{2+}$ ions in the $[Fe_4Cl]^{7+}$ units of the framework. Crystallographically, the four $Fe^{2+}$ centers are equivalent, but a broad absorption profile, rather than the expected single quadrupole doublet is observed. This broadening occurs because of a distribution in the positions of the DMF, $[Fe(DMF)_6]^{3+}$, and $[Fe(DMF)_6]^{2+}$ species that, at least at lower temperatures, are frozen within the pores. This distribution of local environments has been

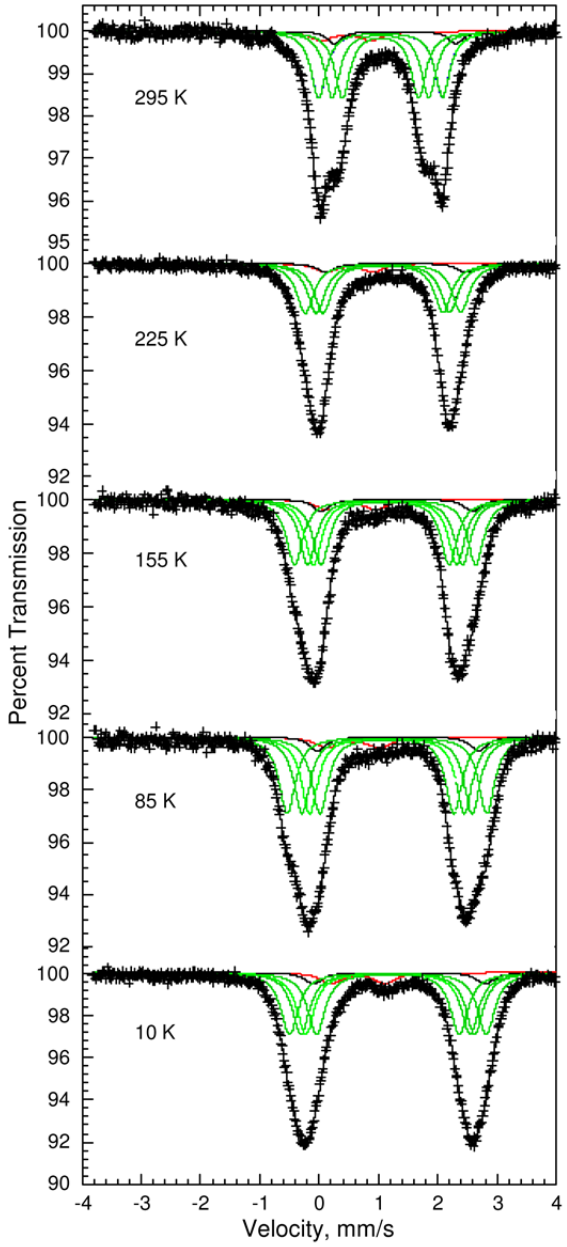


***Figure 3.2.*** Mössbauer spectra collected between 10 and 295 K for a sample of DMF-solvated Fe-BTT. The four green doublets are attributed to the high-spin $Fe^{2+}$ ions in the $[Fe_4Cl]^{7+}$ units of the framework, and the black and red doublets to charge-balancing high-spin $Fe^{2+}$ and $Fe^{3+}$ ions within the pores.

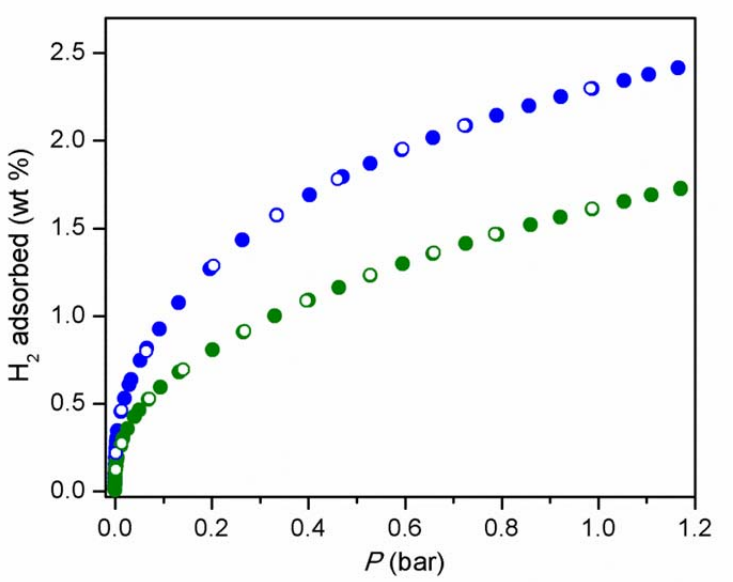


***Figure 3.3.*** Low-pressure $H_2$ adsorption isotherms in Fe-BTT recorded at 77 K (blue) and 87 K (green). Closed and open symbols represent adsorption and desorption, respectively.

fit with the four high-spin $Fe^{2+}$ quadrupole doublets shown in green. The second unusual feature found in the spectra is the narrowing at 225 K and above of the distribution of local environments of the $Fe^{2+}$ ions in the framework. This narrowing occurs because at 225 K and above the mobility of the DMF molecules in the pores increases dramatically, consistent with the melting point of 212 K for bulk DMF. In addition, there should also be an increase in the mobility of the $[Fe^{III}(DMF)_6]^{3+}$ and $[Fe^{II}(DMF)_6]^{2+}$ complexes within the pores at some temperature above 155 K, leading to an averaging of the local environments. This increased mobility within the pores averages the local structural perturbations at an $Fe^{2+}$ site and the framework $Fe^{2+}$ ions therefore become electronically and structurally more similar.

### 3.4.2 Hydrogen Storage Properties

Low-pressure $H_2$ adsorption isotherms for an activated sample of Fe-BTT were collected at 77 and 87 K, and the plots are shown in Figure 3.3. The adsorption of 2.3 wt % at 77 K, and 1.6 wt % at 87 K, is completely reversible, and the steep initial portion of each isotherm is indicative of the presence of strongly-polarizing binding sites with a high affinity for $H_2$. A virial type fitting to the data recorded at the two temperatures allowed the calculation of the isosteric heat of adsorption as a function of $H_2$ coverage, as shown in Figure 3.4. Indeed, the steep rise in the isotherms translates to a zero-coverage isosteric heat of adsorption of –11.9 kJ/mol, which is among the largest recorded for $H_2$ binding in a metal–organic framework.[20] As the loading of $H_2$ is increased, the isosteric heat decreases in magnitude, corresponding to the strongest binding sites becoming saturated and subsequent population of weaker binding sites. At an uptake of 1 wt %, the isosteric heat reaches –7 kJ/mol, whereafter more typical dispersive interactions dominate as the binding mode.

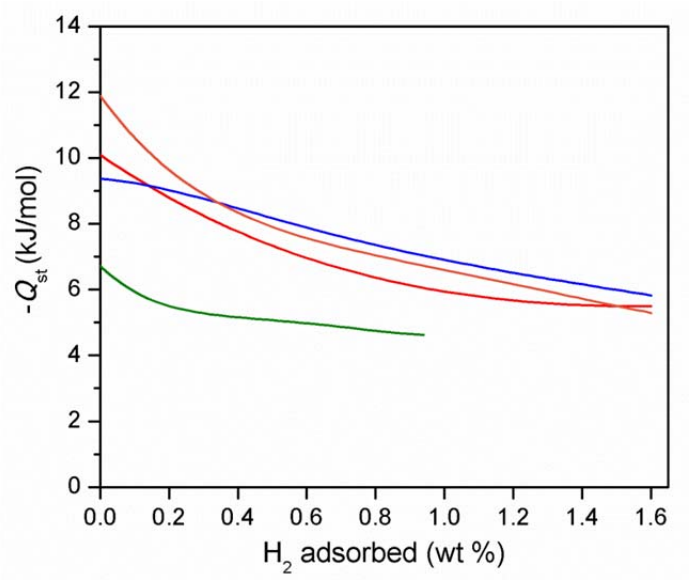


***Figure 3.4.*** Plots of the isosteric heat of adsorption as a function of hydrogen uptake in Fe-BTT (orange), Mn-BTT (red),[5f] Cu-BTT (blue),[5h] and $Zn_4O$(1,4-benzenedicarboxylate)$_3$ (green).[3b]

Comparison of the initial isosteric heat of adsorption for Fe-BTT to that observed for Mn-BTT (–10.1 kJ/mol) reveals a significant increase as a result of metal substitution. This is consistent with the higher charge-to-radius ratio for $Fe^{2+}$ compared to $Mn^{2+}$, leading to a more polarizing binding site at the metal ion. Furthermore, in the case of Cu-BTT, although $Cu^{2+}$ is a smaller ion than $Fe^{2+}$, it has an anisotropic electron distribution that reduces the charge at the open coordination site, leading to a longer $Cu^{2+}$–$H_2$ interaction distance.[5e] This longer distance translates to a lower initial isosteric heat of adsorption of –9.5 kJ/mol. However, beyond 0.4 wt % uptake, the isosteric heat of adsorption for Cu-BTT overtakes that of Fe-BTT. This is likely due to the greater number of desolvated $M^{2+}$ ions in Cu-BTT, whereas Fe-BTT retains some bound methanol molecules.

The higher-pressure adsorption isotherms recorded at 77 K and 298 K are shown in Figure 3.5. At 77 K, Fe-BTT exhibits a maximum excess adsorption of 3.7 wt %. The total adsorption was calculated using the experimental pore volume measured by argon porosimetry, which yielded a value of 0.715 $cm^3/g$. This result is close to the idealistic pore volume calculated from the crystallographic data (0.724 $cm^3/g$). The total uptake, which is more relevant for assessment of the system sorption properties, reaches 4.1 wt % and 35 g/L at 95 bar. Surprisingly, these values are below the corresponding total adsorption values recorded for Mn-BTT (6.9 wt %, 60 g/L at 90 bar),[5f] and Cu-BTT (5.7 wt %, 53 g/L at 90 bar).[5h] Nevertheless, the total uptake in Fe-BTT at 95 bar constitutes a 16% increase in volumetric density compared to that of pure $H_2$ gas at the same pressure.

At 298 K, the total $H_2$ uptake in Fe-BTT reaches 1.0 wt % and 8.4 g/L owing to the high isosteric heat of adsorption at the unsaturated metal centers. This is still somewhat lower than the uptake observed for Mn-BTT, which is likely due to the differences in the unit cell, in particular the position of the extraframework cations, observed for the desolvated structures. The volumetric uptake still, however, ranks among the highest observed at room temperature for

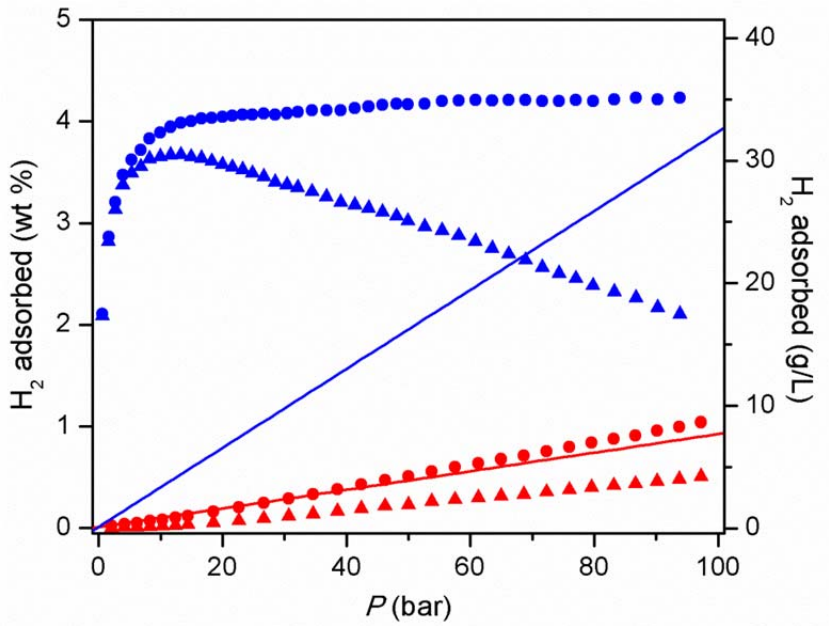


***Figure 3.5.*** High-pressure $H_2$ adsorption isotherms in Fe-BTT recorded at 77 K (blue) and 298 K (red). Triangles and circles represent excess and total uptake, while the solid lines show the density of pure $H_2$ gas.

metal–organic frameworks, highlighting the importance of open coordination sites for high-density $H_2$ storage.[1j]

### 3.4.3 Powder Neutron Diffraction Data

Powder neutron diffraction experiments using the high resolution diffractometer BT1 at the National Institute of Standards and Technology Center for Neutron Research (NCNR) have directly confirmed that the large isosteric heat of adsorption for $H_2$ in Fe-BTT is associated with the presence of open $Fe^{2+}$ coordination sites associated with the $[Fe_4Cl]^{7+}$ clusters of the framework. Prior to $D_2$ loadings, the neutron diffraction pattern of the evacuated form of Fe-BTT was collected using the Ge(311) monochromator and an in-pile collimation of 15 min of arc corresponding to a wavelength of 2.0878 Å. The subsequent structure determination and Rietveld analysis[21] allowed two important structural features of the evacuated material to be elucidated. Firstly, the position of the charge-balancing $Fe^{2+}$ ions could be refined at the expected occupancy of 1/8 for a position approximately 4.23 Å directly above the chloride anion of the $[Fe_4Cl]^{7+}$ cluster in a bowl-like binding site (see Figure 3.6). Interestingly, this is in contrast to the desolvated structures of Mn-BTT and Cu-BTT, wherein the extra-framework cations were observed between two tetrazolate rings in a chelated coordination geometry. Detailed analysis of the neutron diffraction data for Fe-BTT indicated an absence of nuclear scattering density at the analogous chelate site. Secondly, a partial occupancy of approximately 30% of methanol was detected bound to the framework $Fe^{2+}$ ions. Note that throughout the diffraction experiments, there was no evidence for any superlattice or magnetic Bragg reflections and the data could be entirely described from the nuclear structure indicating lack of long-range magnetic order.

The binding sites for $D_2$ within Fe-BTT were located by taking the nuclear density Fourier difference maps between the loaded and bare materials, and allowing the positions and occupancies of $D_2$ to freely refine while fixing the methanol location and composition. The evacuated framework was sequentially dosed with quantities of approximately 4, 8, 20, 33, 65, and 98 $D_2$ molecules per formula unit. A portion of the neutron diffraction pattern obtained at 4 K at a loading of 8 $D_2$ molecules per formula unit is shown in Figure 3.7. The first position in the structure to be occupied by $D_2$, labeled I in Figure 3.8, corresponds to the strongest adsorption site and lies at a remarkably short 2.17(5) Å from the framework $Fe^{2+}$ ion. This is indeed consistent with the higher initial isosteric heat of adsorption for $H_2$ compared to Mn-BTT and Cu-BTT, which exhibited metal–$D_2$ distances of 2.27 and 2.47 Å, respectively.[5e,g] To our knowledge, this constitutes the shortest metal–$D_2$ distance yet observed in a metal–organic framework. The close approach of the hydrogen molecules to the surface is essential for achieving a high storage density. Interestingly, the extra-framework cations do not appear to act as high-affinity binding sites, since no nuclear density was observed in the proximity of these sites at low loadings. This
demonstrates that the greater isosteric heat of adsorption observed at zero-coverage is primarily provided by the unsaturated metal sites of the $[Fe_4Cl]^{7+}$ cluster.

At higher $D_2$ loadings, additional adsorption sites become more prominent. The next strongest binding position, labeled II in Figure 3.8, is situated approximately 3.44 Å above the chloride ion of the $[Fe_4Cl]^{7+}$ units. Four tetrazolate rings are also within 3.60 Å of this site, forming a bowl-like adsorption pocket with a negative surface charge. Up to a loading of 8 $D_2$ molecules per formula unit, only sites I and II are occupied, suggesting that the binding enthalpy at these two sites is considerably higher than the subsequently occupied sites. At a loading of 20 $D_2$ molecules per formula unit, two further sites, labeled III and IV, become occupied. Site III

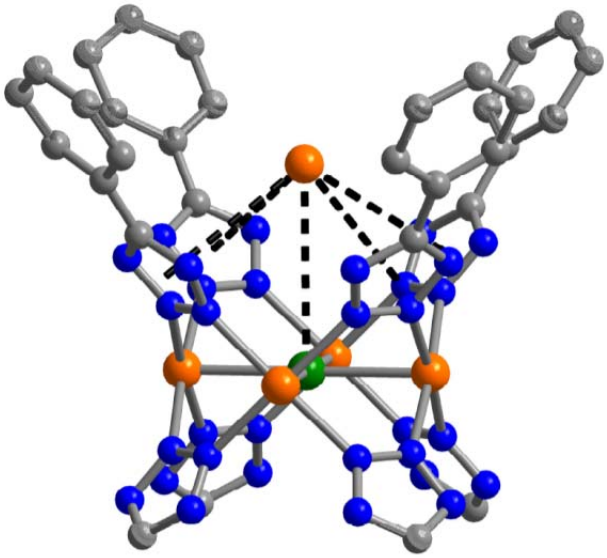

***Figure 3.6.*** The location of the extraframework ions within Fe-BTT as determined by neutron diffraction. Orange, green, blue, and gray spheres represent Fe, Cl, N, and C atoms, respectively. Hydrogen atoms have been omitted for clarity. The occupancy of the extra-framework ions is approximately 1/8.

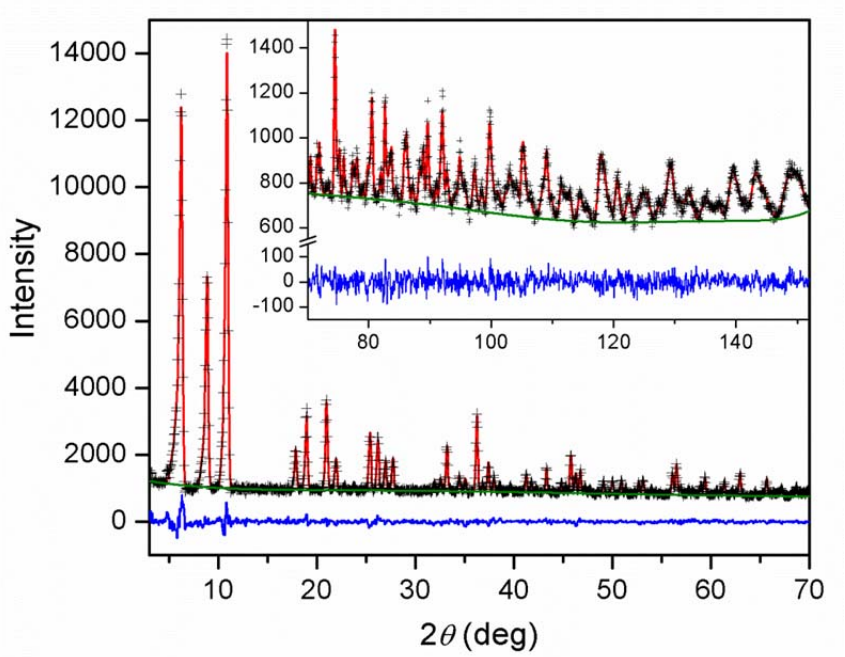


***Figure 3.7.*** Powder neutron data for Fe-BTT loaded with 8 $D_2$ molecules per formula unit. Green lines, crosses, and red lines represent the background, experimental, and calculated diffraction patterns, respectively. The blue line represents the difference between experimental and calculated patterns. The final Rietveld goodness-of-fit parameter was $\chi^2 = 1.063$.

places the $D_2$ molecules at the openings of the sodalite-type cages, allowing interactions with the $N_2$ atoms of four tetrazolate ligands at a distance of approximately 3.45 Å. Site IV is located in the channels of the structure, with the $D_2$ centroid 3.16 Å from the plane of two tetrazolate rings. All subsequently occupied sites, while localized, are typical for physisorbed hydrogen, as reflected in a framework–$D_2$ distance of greater than 3.6 Å.

Comparison of the $D_2$ adsorption sites of Fe-BTT and its analogues reveals a number of differences. Most notably, site III is not occupied within Mn-BTT and Cu-BTT until much higher $D_2$ loadings. The third binding site in the other frameworks corresponds to a position analogous to that of site IV in Fe-BTT, while the position of the fourth occupied site, which places the $D_2$ molecule in close contact with the aromatic ring of the $BTT^{3-}$ ligand, is not occupied in Fe-BTT until higher loadings. These differences presumably reflect changes associated with the slightly differing unit cell dimensions and the distinct position of the extraframework cations in Fe-BTT compared to Mn-BTT and Cu-BTT.

### 3.4.4 Inelastic Neutron Scattering Spectra

The $H_2$ loading characteristics of Fe-BTT have been further probed by inelastic neutron scattering[51,22] using the FANS spectrometer at the NCNR.[23] Spectra were obtained by subjecting the compound to a collimated and monochromated neutron beam, and determining the energy transferred to the sample at a bank of $^3$He detectors after passing the scattered neutrons through a lowenergy band-pass filter consisting of polycrystalline Bi, Be, and graphite. Data were collected at approximately the same loading levels as for the neutron diffraction experiments to allow the

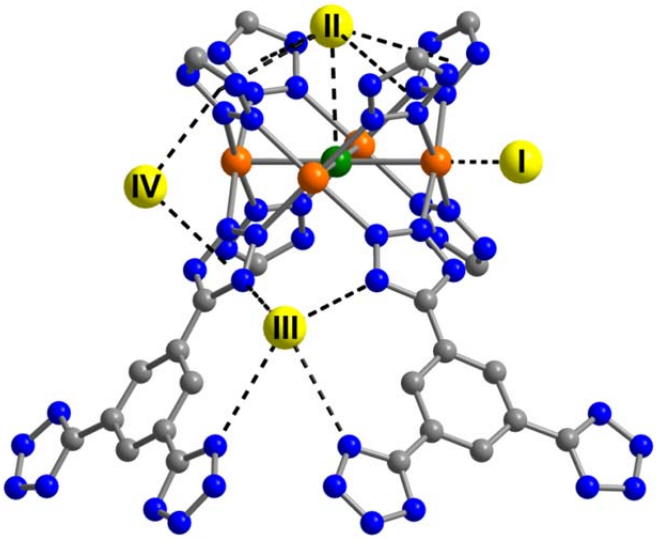


***Figure 3.8.*** The first four $D_2$ binding sites within Fe-BTT determined from Rietveld analysis of the powder neutron diffraction data. Yellow, orange, green, blue, and gray spheres represent $D_2$, iron, chlorine, nitrogen, and carbon, respectively. Hydrogen atoms have been omitted for clarity.

best opportunity for correlation of the FANS spectra with the binding sites observed crystallographically. Routine data reduction and subtraction of the evacuated Fe-BTT spectrum was performed,[24] and selected spectra are shown in Figure 3.9. In the lowest loading data (< 0.5 wt %), there is an absence of a rotational line at 14.7 meV corresponding to the first rotational transition of free hydrogen. This is indicative of a strong rotational hindering potential of the binding sites occupied at these levels, consistent with the large initial isosteric heat of $H_2$ adsorption. At 0.25 wt %, a loading at which sites I and II are populated, two lines are observed at approximately 13.2 and 19.7 meV. These peaks gain intensity upon increasing the loading to 0.5 wt% of $H_2$, and can be assigned as rotational lines that correspond to a rotational barrier of approximately 15 meV.

Upon increasing the loading to 1.25 wt %, sites III and IV become occupied at approximately 50% occupancy. The rotational lines associated with these sites presumably give rise to the new distinct peaks around the energy of free $H_2$, implying a lower rotational barrier. Further increases in the loading to 2.0 wt % increase the intensities of these lines, which corresponds to increasing the population of these sites, as well as the population of an additional site that is a dispersive $H_2$–framework interaction. The highest loading data of 4.0 and 6.0 wt % exhibit very broad indistinct features at higher energy (> 20 meV), adopting the character of molecular recoil from weakly bound hydrogen. The overall intensity of the spectral features scale well with the loading level for all spectra. Furthermore, at a loading of 6 wt %, there is the additional appearance of a shoulder on the most intense peak, which is at a frequency characteristic of bulk hydrogen as would be typical of weakly adsorbed hydrogen on a carbon surface. Comparison of the spectra for normal-$H_2$ (*n*-$H_2$) and para-$H_2$ (*p*-$H_2$) at a loading of 4 wt % reveals a scaling factor of 1.2. The composition of *n*-$H_2$ at room temperature is 25% *p*-$H_2$, and 75% ortho-$H_2$ (*o*-$H_2$). No significant change in this composition is expected upon lowering of the temperature of the gas, unless the conversion between the two forms is catalyzed by a

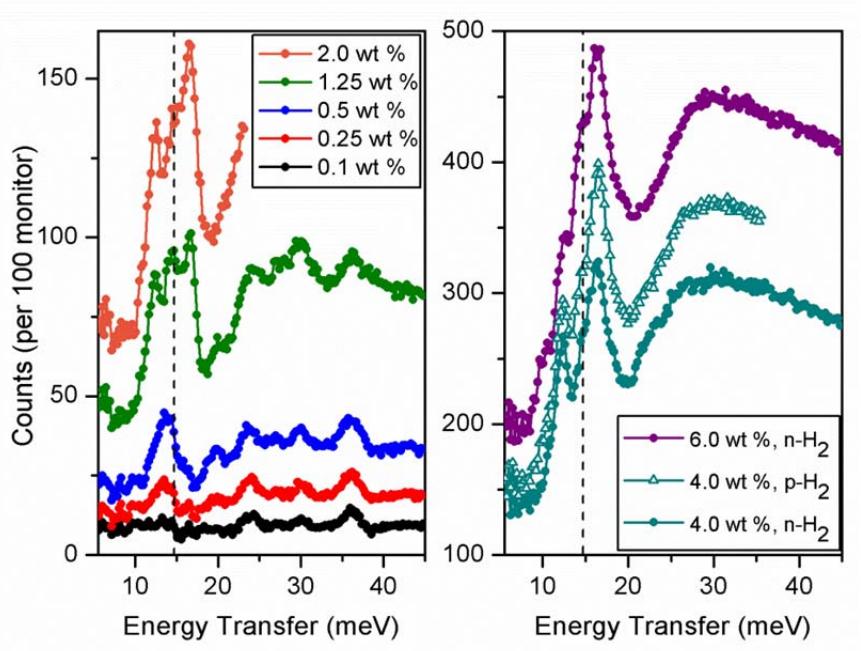


***Figure 3.9.*** Inelastic neutron spectra at several hydrogen loadings following subtraction of the spectrum of evacuated Fe-BTT. Filled circles and open triangles represent data for normal hydrogen ($n$-$H_2$) and para-hydrogen ($p$-$H_2$), respectively. Left: lowest $n$-$H_2$ data up to 2.0 wt %. Right: higher $n$-$H_2$ loadings up to 6 wt %, and $p$-$H_2$ at 4 wt %. In both panels, the dashed line represents the expected energy transfer of 14.7 meV corresponding to the first rotational transition ($J = 0 \rightarrow 1$) for free hydrogen.

paramagnetic material. Indeed, the small scaling factor between the two spectra is indicative of the conversion of $o$-$H_2$ to $p$-$H_2$ by Fe-BTT. This is presumably due to the $H_2$ coming into close proximity with a paramagnetic high-spin $Fe^{2+}$ center following dosing of $H_2$ at approximately 50 K, initiating interconversion between the two forms. However, as the sample is cooled to the final temperature of 4 K, the hydrogen mobility and access to the $Fe^{2+}$ centers becomes sufficiently hindered such that the para–ortho ratio becomes frozen. Evidence for catalytic conversion by solely the $Fe^{2+}$ centers also comes from the dependence of the scaling factor on the loading level. Indeed, as the loading level of $p$-$H_2$ is decreased, the scaling factor approaches 1, consistent with a greater fraction of $H_2$ molecules being able to interact with the $Fe^{2+}$ centers. At a loading of 0.1 wt %, the $p$-$H_2$ and $n$-$H_2$ become virtually superimposable due to the $H_2$ being completely accommodated at the unsaturated coordination site.

### 3.4.5 Selective $CO_2$ Adsorption

Figure 3.10 displays the $CO_2$ and $N_2$ adsorption isotherms obtained for Fe-BTT at 298 K. The initial steep portion of the $CO_2$ isotherm likely corresponds to the strong binding of $CO_2$ to the exposed $Fe^{2+}$ cation sites. The uptake of approximately 3.8 wt % reached in this steep portion is consistent with the interaction of 0.4 $CO_2$ molecules per available $Fe^{2+}$ cation. At 1 bar, the $CO_2$ uptake reaches 13.5 wt %. The near-linear adsorption profile for $N_2$ is indicative of its low affinity for the open metal sites, as expected from its relatively low polarizability. Indeed, this

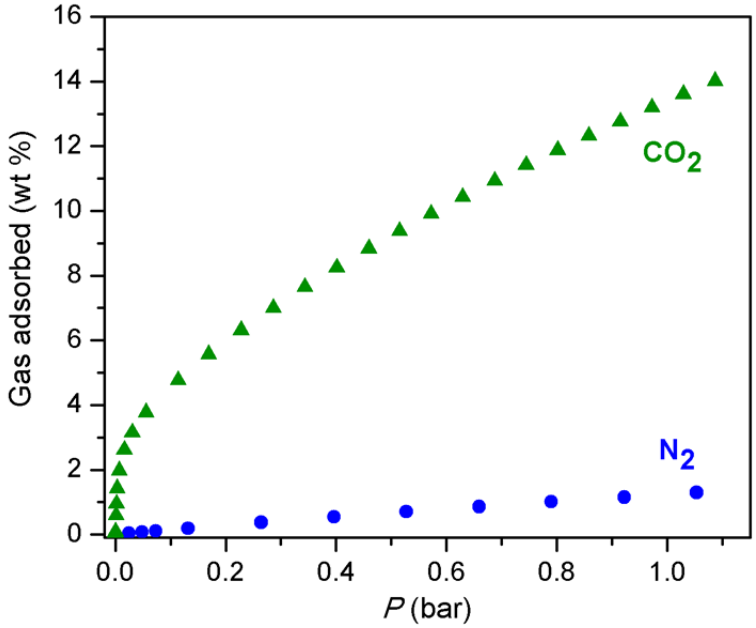


***Figure 3.10.*** Adsorption isotherms for Fe-BTT for the uptake of $CO_2$ (green triangles) and $N_2$ (blue circles) recorded at 298 K.

leads to an $N_2$ uptake of just 1.0 wt % at 1 bar. This is also reflected in the uptake ratio by weight for $CO_2$ over $N_2$, which reaches 30.7 : 1 at 0.1 bar, and 10.8 : 1 at 1.0 bar.

Assessing the utility of an adsorbent for capture of $CO_2$ using single-component isotherms requires that the relative pressures of the gases in a flue gas be taken into account. A typical flue gas has a total pressure of approximately 1 bar, and consists of primarily $N_2$ (70–75 wt %), $CO_2$ (15–16 wt %), and $H_2O$ (5–7 wt %).[25] This converts to partial pressures of approximately 0.15 and 0.75 bar for $CO_2$ and $N_2$, respectively. The separation factor calculated from the experimental uptakes at these partial pressures is approximately 5.5 : 1. For comparison with other metal–organic frameworks investigated for $CO_2$ capture, we note that the uptake of 4.8 wt % at 0.1 bar of $CO_2$ is surpassed only by the compounds $M_2$(DOBDC) (M = Mg, Co, Ni Zn), which possess a higher concentration of open metal cation sites.[5j,7] While these compounds are also favored for their exceptional water stability,[26] it is possible that the larger pore openings within Fe-BTT could provide an advantage in terms of gas diffusion rates.

## 3.5 Outlook

The foregoing results demonstrate the successful use of a high-throughput methodology for the synthesis of a new sodalite-type metal–organic framework, Fe-BTT, featuring open $Fe^{2+}$ cation sites. Gas adsorption measurements combined with neutron diffraction data and inelastic neutron scattering spectroscopy show that these sites provide a strong interaction with $H_2$, drawing it close to the surface to afford an enhanced storage capacity at 298 K. The exposed cation sites further lead to selective adsorption of $CO_2$ over $N_2$ at 298 K, rendering it of potential interest for $CO_2$ capture from flue gas. We anticipate that this powerful synthetic methodology will now provide access to a broad range of isostructural materials, for which the greater polarizing power of cations such as $Mg^{2+}$, $Co^{2+}$, and $Ni^{2+}$ can be expected to give rise to improved $H_2$ storage and $CO_2$ capture properties. In addition, compounds of this type

incorporating triazolate or pyrazolate groups in place of tetrazolate can be expected to exhibit enhanced thermal and chemical stability.[27] Such improvements in stability are deemed essential for enabling the complete desolvation of the metal cation sites, and improving the suitability of these metal–organic frameworks for real-world applications.

### 3.6 Acknowledgments

This research was funded by the General Motors Company, the US Defense Logistics Agency, and the Center for Gas Separations Relevant to Clean Energy Technologies, an Energy Frontier Research Center funded by the U.S. Department of Energy, Office of Science, Office of Basic Energy Sciences under award number DE-SC0001015. Work at NIST was partially supported by the U.S. Department of Energy within the Hydrogen Sorption Center of Excellence. I acknowledge Fulbright New Zealand for partial financial support, and thank Dr M. T. Sougrati for assistance in obtaining some of the Mössbauer spectra, Dr T. Boussie, Dr C. Yuan, and Dr R. Rosen of Symyx Technologies for assistance with setting up the high-throughput apparatus, and Dr A. G. DiPasquale for helpful discussions.

***Table 3.2***. Mössbauer Spectral Parameters for DMF-solvated Fe-BTT

| *T*, K | $\delta$, mm/s[b] | $\Delta E_Q$, mm/s | $\Gamma$, mm/s | *Area,*[c] *%* | *Area,* (%$\varepsilon$)(mm/s) | Assignment |
|---|---|---|---|---|---|---|
| 295 | 0.45 | 0.84 | 0.45 | 4.75 | 6.04 | $[Fe^{III}(DMF)_6]^{3+}$ |
| | 1.28 | 2.05 | 0.300(3) | 4.27 | - | $[Fe^{II}(DMF)_6]^{2+}$ |
| | 1.038(1) | 1.772(4) | 0.300(3) | 90.98 | - | $[(Fe^{II}{}_4Cl)_3(BTT)_8]^{3-}$ |
| 277 | 0.47 | 0.83 | 0.45 | 4.75 | 7.22 | $[Fe^{III}(DMF)_6]^{3+}$ |
| | 1.28 | 2.15 | 0.37(1) | 4.27 | - | $[Fe^{II}(DMF)_6]^{2+}$ |
| | 1.046(3) | 1.94(2) | 0.37(1) | 90.98 | - | $[(Fe^{II}{}_4Cl)_3(BTT)_8]^{3-}$ |
| 260 | 0.49 | 0.82 | 0.45 | 4.75 | 7.78 | $[Fe^{III}(DMF)_6]^{3+}$ |
| | 1.29 | 2.25 | 0.41(1) | 4.27 | - | $[Fe^{II}(DMF)_6]^{2+}$ |
| | 1.060(2) | 2.09(3) | 0.41(1) | 90.98 | - | $[(Fe^{II}{}_4Cl)_3(BTT)_8]^{3-}$ |
| 225 | 0.51 | 0.80 | 0.45 | 4.75 | 8.71 | $[Fe^{III}(DMF)_6]^{3+}$ |
| | 1.29 | 2.35 | 0.357(5) | 4.27 | - | $[Fe^{II}(DMF)_6]^{2+}$ |
| | 1.077(1) | 2.29(4) | 0.357(5) | 90.98 | - | $[(Fe^{II}{}_4Cl)_3(BTT)_8]^{3-}$ |
| 155 | 0.54 | 0.84 | 0.45 | 4.75 | 10.88 | $[Fe^{III}(DMF)_6]^{3+}$ |
| | 1.18 | 2.01 | 0.336(1) | 4.27 | - | $[Fe^{II}(DMF)_6]^{2+}$ |
| | 1.113(5) | 2.560(5) | 0.336(1) | 90.98 | - | $[(Fe^{II}{}_4Cl)_3(BTT)_8]^{3-}$ |
| 85 | 0.58 | 0.88 | 0.45(3) | 4.75 | 12.84 | $[Fe^{III}(DMF)_6]^{3+}$ |
| | 1.33 | 2.72 | 0.329(5) | 4.27 | - | $[Fe^{II}(DMF)_6]^{2+}$ |
| | 1.144(2) | 2.774(5) | 0.329(5) | 90.98 | - | $[(Fe^{II}{}_4Cl)_3(BTT)_8]^{3-}$ |
| 60 | 0.65 | 0.85 | 0.44(2) | 4.75 | 13.64 | $[Fe^{III}(DMF)_6]^{3+}$ |
| | 1.35 | 2.94 | 0.350(4) | 4.27 | - | $[Fe^{II}(DMF)_6]^{2+}$ |
| | 1.152(1) | 2.812(4) | 0.350(4) | 90.98 | - | $[(Fe^{II}{}_4Cl)_3(BTT)_8]^{3-}$ |
| 10 | 0.65 | 0.92 | 0.43(2) | 4.75 | 14.48 | $[Fe^{III}(DMF)_6]^{3+}$ |
| | 1.35 | 2.90 | 0.353(5) | 4.27 | - | $[Fe^{II}(DMF)_6]^{2+}$ |
| | 1.158(1) | 2.857(6) | 0.353(5) | 90.98 | - | $[(Fe^{II}{}_4Cl)_3(BTT)_8]^{3-}$ |

[a]Statistical errors are given and the absence of an error indicates that the parameter was constrained to the value given in the final refinement. The average parameters are given for the $[(Fe^{II}{}_4Cl)_3(BTT)_8]^{3-}$ anion. [b]The isomer shifts are given relative to 295 K $\alpha$-iron powder. [c]The relative areas have been constrained to the values observed at 10 K and have a statistical accuracy of ±0.2 %.

## 3.7 References and Notes


(1) (a) Eddaoudi, M.; Kim, J.; Rosi, N.; Vodak, D.; Wachter, J.; O'Keeffe, M.; Yaghi, O. M. *Science*, **2002**, *295*, 469. (b) Kitagawa, S.; Kitaura, R.; Noro, S.-I. *Angew. Chem., Int. Ed.* **2004**, *43*, 2334. (c) Matsuda, R.; Kitaura, R.; Kitagawa, S.; Kubota, Y.; Belosludov, R. V.; Kobayashi, T. C.; Sakamoto, H.; Chiba, T.; Takata, M.; Kawazoe, Y. *Nature*, **2005**, *436*, 238. (d) Millward, A. R.; Yaghi, O. M. *J. Am. Chem. Soc.* **2005**, *127*, 17998. (e) Furukawa, H.; Miller, M. A.; Yaghi, O. M. *J. Mater. Chem.* **2007**, *17*, 3197. (f) Férey G. *Chem. Soc. Rev.* **2008**, *37*, 191. (g) Ma, S.; Sun, D.; Simmons, J. M.; Collier, C. D.; Yuan, D.; Zhou, H.-C. *J. Am. Chem. Soc.* **2008**, *130*, 1012. (h) Morris, R. E.; Wheatley, P. S. *Angew. Chem., Int. Ed.* **2008**, *47*, 4966. (i) Llewellyn, P. L.; Bourrelly, S.; Serre, C.; Vimont, A.; Daturi, M.; Hamon, L.; De Weireld, G.; Chang, J.-S.; Hong, D.-Y.; Hwang, Y. K.; Jhung, S. H.; Férey, G. *Langmuir* **2008**, *24*, 7245. (j) Murray, L. J.; Dincă, M.; Long, J. R. *Chem. Soc. Rev.* **2009**, *38*, 1294. (k) Horike, S.; Shimomura, S.; Kitagawa, S. *Nat. Chem.* **2009**, *1*, 695.

(2) EERE: Hydrogen, Fuel Cells, & Infrastructure Technologies Program, http://www.eere.energy.gov/hydrogenandfuelcells, (accessed January 2010).

(3) (a) Latroche, M.; Surblé, S. ; Serre, C.; Mellot-Draznieks, C.; Llewellyn, P. L.; Lee, J.-H.; Chang, J.-S.; Jhung, S. H.; Férey, G. *Angew. Chem., Int. Ed.* **2006**, *45*, 8227. (b) Kaye, S. S.; Dailly, A.; Yaghi, O. M.; Long, J. R. *J. Am. Chem. Soc.* **2007**, *129*, 14176. (c) Sumida, K.; Hill, M. R.; Horike, S.; Dailly, A.; Long, J. R. *J. Am. Chem. Soc.* **2009**, *131*, 15120. (d) Koh, K.; Wong-Foy, A. G.; Matzger, A. J. *J. Am. Chem. Soc.* **2009**, *131*, 4184.

(4) Bhatia, S. K.; Myers, A. L. *Langmuir* **2006**, *22*, 1688.

(5) (a) Dietzel, P. D. C.; Morita, Y.; Blom, R.; Fjellvag, H. *Angew. Chem., Int. Ed.* **2005**, *44*, 6354. (b) Dincă M.; Long, J. R. *J. Am. Chem. Soc.* **2005**, *127*, 9376. (c) Rosi, N. L.; Kim, J.; Eddaoudi, M.; Chen, B.; O'Keeffe, M.; Yaghi, O. M. *J. Am. Chem. Soc.* **2005**, *127*, 1504. (d) Vimont, A.; Goupil, J.-M.; Lavalley, J.-C.; Daturi, M.; Surblé, S.; Serre, C.; Millange, F.; Férey, G. Audebrand, N. *J. Am. Chem. Soc.* **2006**, *128*, 3218. (e) Moon, H. R.; Kobayashi, N.; Suh, M. P. *Inorg. Chem.* **2006**, *45*, 8672. (f) Dincă, M.; Dailly, A.; Liu, Y.; Brown, C. M.; Neumann, D. A.; Long, J. R. *J. Am. Chem. Soc.* **2006**, *128*, 16876. (g) Dietzel, P. D. C.; Panella, B.; Hirscher, M.; Blom, R.; Fjellvag, H. *Chem. Commun.* **2006**, 959. (h) Dincă, M.; Han, W. S.; Liu, Y.; Dailly, A.; Brown, C. M.; Long, J. R. *Angew. Chem., Int. Ed.* **2007**, *46*, 1419. (i) Dincă, M.; Long, J. R. *Angew. Chem., Int. Ed.* **2008**, *47*, 6766. (j) Caskey, S. R.; Wong-Foy, A. G.; Matzger, A. J. *J. Am. Chem. Soc.* **2008**, *130*, 10870. (k) Dietzel, P. D. C.; Blom, R.; Fjellvag, H. *Eur. J. Inorg. Chem.* **2008**, 3624. (l) Liu, Y.; Kabbour, H.; Brown, C. M.; Neumann , D. A.; Ahn, C. C. *Langmuir* **2008**, *24*, 4772.

(6) Unsaturated metal sites within inorganic and hybrid materials have previously been shown to facilitate hydrogen adsorption: (a) Forster, P. M.; Eckert, J.; Chang, J.-S.; Park, S.-E.; Férey, G.; Cheetham, A. K. *J. Am. Chem. Soc.* **2003**, *125*, 1309. (b) Hartman, M. R.; Peterson, V. K.; Liu, Y.; Kaye, S. S.; Long, J. R. *Chem. Mater.* **2006**, *18*, 3221. (c) Forster, P. M.; Eckert, J.; Heiken, B. D.; Parise, J. B.; Yoon, J. W.; Jhung, S. H.; Chang, J.-S.; Cheetham, A. K. *J. Am. Chem. Soc.* **2006**, *128*, 16846.

(7) (a) Dietzel, P. D. C.; Johnsen, R. E.; Fjellvag, H.; Bordiga, S.; Groppo, E.; Chavan, S.; Blom, R. *Chem. Commun.* **2008**, 5125. (b) Dietzel, P. D. C.; Besikiotis, V.; Blom, R. *J. Mater. Chem.* **2009**, *19*, 7362. (c) Britt, D.; Furukawa, H.; Wang, B.; Glover, T. G.; Yaghi,

O. M. *Proc. Natl. Acad. Sci. U. S. A.* **2009**, *106*, 20637. (d) Yazaydin, A. Ö.; Snurr, R. Q.; Park, T.-H.; Koh, K.; Liu, J.; LeVan, M. D.; Benin, A. I.; Jakubczak, P.; Lanuza, M.; Galloway, D. B.; Low, J. J.; Willis, R. R. *J. Am. Chem. Soc.* **2009**, *131*, 18198.

(8) Zhou, W.; Wu, H.; Yildirim, T. *J. Am. Chem. Soc.* **2008**, *130*, 15268.

(9) (a) Whitfield, T. R.; Wang, X.; Liu, L.; Jacobson, A. J. *Solid State Sci.* **2005**, *7*, 1096. (b) Bauer, S.; Serre, C.; Devic, T.; Horcajada, P.; Marrot, J.; Férey, G.; Stock, N. *Inorg. Chem.* **2008**, *47*, 7568. (c) Volkringer, C.; Popov, D.; Loiseau, T.; Férey, G.; Burghammer, M.; Riekel, C.; Haouas, M.; Taulelle, F. *Chem. Mater.* **2009**, *21*, 5695. (d) Horcajada, P.; Chalati, T.; Serre, C.; Gillet, B.; Sebrie, C.; Baati, T.; Eubank, J. F.; Heurtaux, D.; Clayette, P.; Kreuz, C.; Chang, J.-S.; Hwang, Y. K.; Marsaud, V.; Bories, P.-N.; Cynober, L.; Gil, S.; Férey, G.; Couvreur, P.; Gref, R. *Nat. Mater.* **2010**, *9*, 172.

(10) (a) Halder, G. J.; Chapman, K. W.; Neville, S. M.; Moubaraki, B.; Murray, K. S.; Létard, J.-F.; Kepert, C. J. *J. Am. Chem. Soc.* **2008**, *130*, 17552. (b) Ma, S.; Yuan, D.; Chang, J.-S.; Zhou, H.-C. *Inorg. Chem.* **2009**, *48*, 5398.

(11) (a) Choi, K.; Gardner, D.; Hilbrandt, N.; Bein, T. *Angew. Chem., Int. Ed.* **1999**, *38*, 2891. (b) Klein, J.; Lehmann, C. W.; Schmidt, H.-W.; Maier, W. F. *Angew. Chem., Int. Ed.* **1998**, *37*, 3369. (c) Zhang, L.; Yao, J.; Zeng, C.; Xu, N. *Chem. Commun.* **2003**, 2232. (d) Koinuma, H.; Takeuchi, I. *Nat. Mater.* **2004**, *3*, 429. (e) Corma, A.; Moliner, M.; Serra, J. M.; Serna, P.; Díaz-Cabañas, M. J.; Baumes, L. A. *Chem. Mater.* **2006**, *18*, 3287.

(12) (a) Banerjee, R.; Phan, A.; Wang, B.; Knobler, C.; Furukawa, H.; O'Keeffe, M.; Yaghi, O. M. *Science*, **2008**, *319*, 939. (b) Sonnauer, A.; Hoffmann, F.; Fröba, M.; Kienle, L.; Duppel, V.; Thommes, M.; Serre, C.; Férey, G.; Stock, N. *Angew. Chem., Int. Ed.* **2009**, *48*, 3791.

(13) Spek, A. L. *J. Appl. Crystallogr.* **2003**, *36*, 7.

(14) Accessible Surface Area Calculation Program, website address (August 2009): http://www.see.ed.ac.uk/~tduren/research/surface_area/.

(15) Rappe, A. K.; Casewit, C. J.; Colwell, K. S.; Goddard, W. A.; Skiff, W. M. *J. Am. Chem. Soc.* **1992**, *114*, 10024.

(16) Larson, A. C.; Von Dreele, R. B. *General Structure Analysis System (GSAS)*, Los Alamos National Laboratory Report LAUR 86-748 (2000).

(17) Walton, K. S.; Snurr, R. Q. *J. Am. Chem. Soc.* **2007**, *129*, 8552.

(18) Düren, T.; Millange, F.; Férey, G.; Walton, K. S.; Snurr, R. Q. *J. Phys. Chem. C* **2007**, *111*, 15350.

(19) Linert, W.; Gutmann, V.; Baumgartner, O.; Wiesinger, G.; Kirchmayr, H. *Inorg. Chim. Acta* **1983**, *74*, 123.

(20) The greatest isosteric heat of adsorption at zero-coverage yet observed for a metal–organic framework is –15.1 kJ/mol in $Co_4(H_2O)_4(MTB)_2$ ($H_4MTB$ = methanetetrabenzoic acid), which features exposed $Co^{2+}$ cations: Cheon, Y. E.; Suh, M. P. *Chem. Commun.* **2009**, 2296. Moreover, a site-specific binding enthalpy of –13.5 kJ/mol has been observed in $Ni_2(DOBDC)$ ($H_4DOBDC$ = 2,5-dihydroxyterephthalic acid), which possesses exposed $Ni^{2+}$ cations: Vitillo, J. G.; Gegli, L.; Chavan, S.; Ricchiardi, G.; Spoto, G.; Dietzel, P. D. C.; Bordiga, S.; Zecchina, A. *J. Am. Chem. Soc.* **2008**, *130*, 8386.

(21) Toby, B. H. *J. Appl. Crystallogr.* **2001**, *34*, 210.

(22) A number of inelastic neutron scattering studies of hydrogen adsorption in metal–organic frameworks have been reported recently: (a) Rowsell, J.; Eckert, J.; Yaghi, O. M. *J. Am. Chem. Soc.* **2005**, *127*, 14904. (b) Liu, Y.; Brown, C. M.; Neumann, D. A.; Peterson V. K.; Kepert, C. J. *J. Alloys Compd.* **2007**, *446–447*, 385. (c) Mulder, F. M.; Dingemans, T. J.;

Schimmel, H. G.; Ramirez-Cuesta, A. J.; Kearley, G. J. *Chem. Phys.* **2008**, *351*, 72. (d) Brown, C. M.; Liu, Y.; Yildirim, T.; Peterson, V. K.; Kepert, C. J. *Nanotechnology* **2009**, *20*, 204025.

(23) Udovic, T. J.; Brown, C. M.; Leao, J. B.; Brand, P. C.; Jiggetts, R. D.; Zeitoun, R.; Pierce, T. A.; Peral, I.; Copley, J. R. D.; Huang, Q.; Neumann, D. A.; Fields, R. J. *Nucl. Instrum. Methods Phys. Res. Sect. A* **2008**, *588*, 406.

(24) Azuah, R. T.; Kneller, L. R.; Qiu, Y.; Tregenna-Piggott, P. L. W.; Brown, C. M.; Copley, J. R. D.; Dimeo, R. M. *J. Res. Natl. Inst. Stand. Technol.* **2009**, *114*, 241.

(25) Trachtenberg, M. C.; Cowan, R. M.; Smith, D. A. in Proceedings of the Sixth Annual Conference on Carbon Capture & Sequestration, Pittsburgh, USA, **2007**.

(26) Low, J. J.; Benin, A. I.; Jakubczak, P.; Abrahamian, J. F.; Faheem, S. A.; Willis, R. R. *J. Am. Chem. Soc.* **2009**, *131*, 15834.

(27) Demessence, A.; D'Alessandro, D. M.; Foo, M. L.; Long, J. R. *J. Am. Chem. Soc.* **2009**, *131*, 8784.

# Chapter 4: Hydrogen Storage Properties and Neutron Scattering Studies of $Mg_2$(dobdc) – A Metal-Organic Framework with Open $Mg^{2+}$ Adsorption Sites

## 4.1 Introduction

Owing to their high permanent porosity, exceptional structural and chemical tunability, and convenient modular synthesis, metal-organic frameworks have recently come under intensive study for use as solid-state sorbents in gas storage applications.[1] With regard to cryogenic hydrogen storage, gravimetric and/or volumetric hydrogen storage capacities that approach the U.S. Department of Energy targets[2] for mobile systems have been demonstrated in the highest surface area materials.[1c,3] However, the performance of these materials is greatly diminished at ambient temperature due to the weak, physisorptive interactions between the internal pore surface and the hydrogen molecules. Indeed, the isosteric heat of $H_2$ adsorption within these materials typically lies in the range of –5 to –7 kJ/mol, which is well below the –15 kJ/mol that is considered optimal for a sorbent operating between 1.5 and 30 bar at 298 K.[4,5] The study of metal‑organic frameworks with exposed metal cation sites represents one promising avenue for achieving stronger framework‑$H_2$ interactions, and is of particular interest for light cations with a high charge density.[6,7] Herein, we report the hydrogen storage properties of $Mg_2$(dobdc) (MOF-74(Mg); dobdc$^{4-}$ = 2,5-dioxido-1,4-benzenedicarboxylate),[7d,e] which possesses pores that are decorated with unsaturated $Mg^{2+}$ coordination sites (see Figure 4.1). Importantly, rigorous study of the adsorption properties via adsorption experiments, variable-temperature infrared spectroscopy, and neutron scattering methods affords a detailed description of the loading characteristics, which is crucial for the design of next-generation materials.

## 4.2 Experimental Section

All reagents were obtained from commercial vendors and used without further purification. All manipulations, unless otherwise stated, were performed in the air.

**Synthesis and activation of $Mg_2$(dobdc).** The literature procedure[7d] was adapted. $H_4$dobdc (0.56 g, 2.8 mmol), $Mg(NO_3)_2{\cdot}6H_2O$ (2.4 g, 9.3 mmol), DMF (220 mL), ethanol (15 mL), and water (15 mL) were added to a 500 mL conical flask, and the mixture was sonicated until dissolution of the solid reagents. The mixture was then dispensed into 25 × 20 mL scintillation vials, and tightly capped with Teflon-lined caps. The vials were then placed on a hot plate at 120 °C, and heated for a period of 8 h. The resulting solid was then combined, and transferred to a dinitrogen-filled glove box. The material was submerged in anhydrous DMF (50 mL), and heated at 80 °C for a period of 2 days, replacing the DMF each 12 h. The DMF was decanted, and replaced with methanol (50 mL). The suspension was heated to 100 °C for a period of 3 days, replacing the methanol each 12 h. The material was activated by heating the solid *in vacuo* to a temperature of 180 °C at a ramp rate of 0.2 °C/min to afford 0.35 g (51 %) of desolvated product.

**Infrared Spectra.** A thin self-supported wafer of solvated $Mg_2$(dobdc) was prepared and activated under high vacuum (residual pressure $<10^{-4}$ mbar) at 433 K for 18 h. Transmission FTIR spectra were collected at 2 $cm^{-1}$ resolution on a Bruker Equinox-55 FTIR spectrometer equipped with an MCT detector. The measurements were performed using a custom-made cryogenic cell that allows: (i) *in-situ* high-temperature activation of the sample under a high

vacuum and (ii) variable-temperature infrared spectroscopy of the adsorbed species while simultaneously measuring temperature and equilibrium pressure. A series of IR absorption spectra recorded over a sufficiently large temperature range while simultaneously measuring temperature and equilibrium pressure of the adsorbed gas, allows the standard adsorption enthalpy and entropy to be determined by following the variable-temperature infrared method. Here, integrated absorbance ($A$) of an infrared absorption band characteristic of a gas adsorption complex, temperature ($T$) and equilibrium pressure ($p$) are considered to be interrelated by the Langmuir type equation:

$$\theta = A/A_{\mathrm{M}} = K(T)p/[1 + K(T)p] \qquad (1)$$

where $\theta$ stands for the fractional coverage of (localized) adsorption sites, $A_{\mathrm{M}}$ is the integral IR absorbance corresponding to full coverage ($\theta$ = 1), and $K$ is the adsorption equilibrium constant at temperature, $T$. Combination of eq. 1 with the van't Hoff (eq. 2) leads to eq. 3 below;

$$K(T) = \exp(-\Delta H^0/RT)\exp(\Delta S^0/R) \qquad (2)$$

$$\ln[A/(A_{\mathrm{M}} - A)p] = (-\Delta H^0/RT) + (\Delta S^0/R) \qquad (3)$$

After determining the relative band intensity from the integrated infrared absorbance as a function of $T$ and $p$, eq. 3 gives direct access to the standard adsorption enthalpy ($\Delta H^0$) and entropy ($\Delta S^0$). It should be noted, however, that knowledge of $A_{\mathrm{M}}$ is needed. From that approximate value (for each of the adsorbed gases), we obtained the corresponding refined values of $A_{\mathrm{M}}$ by following the iteration procedure described elsewhere.[28]

**Powder Neutron Diffraction.** The powder diffraction patterns were measured at 4 K using the BT-1 diffractometer at the National Institute of Standards and Technology Center for Neutron Research (NCNR). An activated sample of $Mg_2$(dobdc) (1.89 g) was loaded in a vanadium cell equipped with a capillary gas line and a packless valve, and sealed with an indium O-ring. The sample was mounted onto a sample stick, equipped with a stainless-steel gas line with an additional valve for a top loading closed-cycle helium refrigerator (CCR). Using a wavelength of 2.078 Å and collimation of 15', powder patterns were recorded for the bare material and at nominal loading values of 0.6 $D_2$, 1.2 $D_2$, and 2.4 $D_2$ per $Mg^{2+}$ site. During the experiments, a known amount of hydrogen (deuterium) gas was loaded into the sample, which was maintained at a temperature of 70 K until no pressure drop could be observed for at least 1 minute. The sample was then cooled down to the base temperature of the CCR (4 K) over one hour in order to perform measurements. In all cases the outgas pressure reading was zero well before reaching 25 K. Data collection times at 4 K were for approximately 11 h.

Neutron scattering diffraction patterns were analyzed using the Rietveld refinement method with the program EXPGUI.[9] The model of the bare material, based on that of previous work,[10] was refined first and it was used as the starting point for subsequent refinements of the $D_2$-loaded samples. Fourier difference maps were used to successively determine the missing nuclear density from the added $D_2$. In the refinements, deuterium molecules are treated as point scatters with double occupancy since they are quantum mechanically rotationally averaged in the ground state.[11] The deuterium adsorbed at the metal site was able to be refined with anisotropic thermal parameters, while the higher adsorption sites were refined isotropically. Final

refinements at the highest loading were performed with anisotropic thermal parameters for all deuterium.

**Inelastic Neutron Scattering (INS).** The INS spectra were measured at 4 K using the pyrolytic graphite monochromator and 20'-20' collimation options on the BT-4 filter analyzer neutron spectrometer (FANS)[12] at the NCNR. The sample (1.286 g) was sealed in a cylindrical aluminum cell suitable for *in-situ* gas loading while cooled in a CCR.

Hydrogen gas was used during the measurements to take advantage of its large incoherent neutron scattering cross section. A $H_2$ molecule is a very good quantum rotor due to its light mass and consists of two indistinguishable fermions (protons) that require the wavefunction to be *anti*-symmetric. If the nuclear spins of two protons are anti-parallel, $H_2$ is said to be in a *para* state (*p*-$H_2$); otherwise, it is in an *ortho* state (*o*-$H_2$). The quantum rotation number, $J$, of a $H_2$ molecule thus has to be even for a *para*-$H_2$ and odd for an *ortho*-$H_2$. At room temperature, only one fourth of $H_2$ molecules are in the *para* state. Usually, the conversion rate between states is very slow, but can be greatly accelerated in the presence of a fluctuation magnetic moment. Normal hydrogen (*n*-$H_2$) consisting of 25 % *p*-$H_2$ and 75% *o*-$H_2$ was used in these experiments.

A neutron scattered by a $H_2$ molecule can induce the required nuclear spin flip to convert a *para*/*ortho* $H_2$ to an *ortho*/*para* $H_2$. This *para-ortho* or *ortho-para* transition is associated with the change of the rotational quantum number, $J$, from even/odd to odd/even, and has a large neutron scattering cross-section that is proportional to the incoherent neutron scattering cross-section of the proton. INS spectra of the adsorbed $H_2$ were obtained by subtracting the INS spectrum of the bare materials. For a free hydrogen molecule, the *para-ortho* transition is usually associated with the $J = 0$ to $J = 1$ excitation occurring with an energy of 14.7 meV, which can be directly measured by INS but not optical spectroscopies. The local potential of a host material will generate rotational barriers for the adsorbed $H_2$ which typically cause the $J = 1$ state to split into its three sublevels. Additionally, the translation excitations of the $H_2$ molecule may be coupled to the rotational transition and complicate the observed spectra. Hence, the INS spectra of adsorbed $H_2$ may show complex features with multiple peaks in the spectrum containing rich information about the host material and the hydrogen interactions.

Loadings of 0.2, 0.4 and 0.6 *n*-$H_2$ per $Mg^{2+}$ site were performed at 70 K with data collection at 4 K. Additional measurement at 0.2, 0.4, 0.6 and 1.2 loadings were also performed using *p*-$H_2$ after evacuating the system of $H_2$ at room temperature. Data were collected for approximately 9 h per loading. The energy resolution is between 1.2 meV to 2.0 meV over the energy transfer ranges accessible.

Background measurements of unloaded and activated parent $Mg_2$(dobdc) and $Zn_2$(dobdc) compounds were made to higher energy transfers (35 meV to 125 meV) using a copper monochromator with 20'-20' collimation before and after the monochromator resulting in an energy resolution that degrades from 1.2 meV to 3 meV with increasing energy transfer. Data from the two monochromators are normalized to merge around 37 meV. Data reduction, including the subtraction of the bare $Mg_2$(dobdc) spectrum from the hydrogen loaded spectra, and peak fitting were performed within the DAVE software suite.[13]

**Quasielastic Neutron Scattering (QENS).** The QENS spectra were measured using the Disk Chopper Spectrometer (DCS)[14] at the NCNR. QENS measurements using an instrument configured for the highest neutron flux at a wavelength of 5.0 Å. With detectors masked that contained Bragg peaks, and grouped in momentum transfer ($Q$) with 0.2 $Å^{-1}$ bins, this instrument

configuration allows for an accessible $Q$ range of 0.27 Å$^{-1}$ to 2.27 Å$^{-1}$ with an elastic energy resolution of approximately 110 meV.

An activated sample of $Mg_2$(dobdc) sample (1.286 g) was mounted in a CCR. As with the other experiments, the sample can was connected with a stainless steel capillary line to a gas-handling unit consisting of a reference volume and a high-resolution pressure transducer. Normal hydrogen loading was performed at 77 K at select pressures along the hydrogen isotherm. These correspond to $H_2$:Mg loadings of 0.33, 0.86, 0.95, 1.21, 1.42 and 1.57. Scattering from $Mg_2$(dobdc) without $H_2$ was also measured at 77 K to serve as a background and subtracted from the loaded data.

An additional series of data were collected at a shorter wavelength of 1.81 Å using the medium resolution configuration of the disk chopper slits. The accessible Q-range is grouped in bins of 0.3 Å$^{-1}$ between 0.75 Å$^{-1}$ to 5.82 Å$^{-1}$ with an elastic energy resolution of approximately 1 meV. In this case data were collected at 4 K for the bare $Mg_2$(dobdc) and the same after loading with 1.2, 2.0, and 2.6 $p$-$H_2$ per Mg site. Data reduction, including vanadium normalization, the subtraction of the bare $Mg_2$(dobdc) spectrum from the hydrogen loaded spectra, masking of detectors containing Bragg peaks, and peak fitting were performed within the DAVE software suite.[7]

**Accessible Surface Area Calculation.** The source code for the accessible surface area calculation program was obtained free of charge from the Internet.[15] The crystallographic information file (CIF) obtained from the single crystal X-ray structure was converted to the XYZ file format using Mercury CSD 2.0. The XYZ file and UFF force field atomic parameters[16] were used as input for the simulation (atomic diameters (Å): H 2.571, C 3.431, N 3.260, O 3.118, Mg 2.691), and the accessible surface area was evaluated using a dinitrogen-sized probe molecule (diameter = 3.681 Å) inserted at randomized points in the unit cell, and averaging the resultant individual accessible surface area values after 5000 trials.

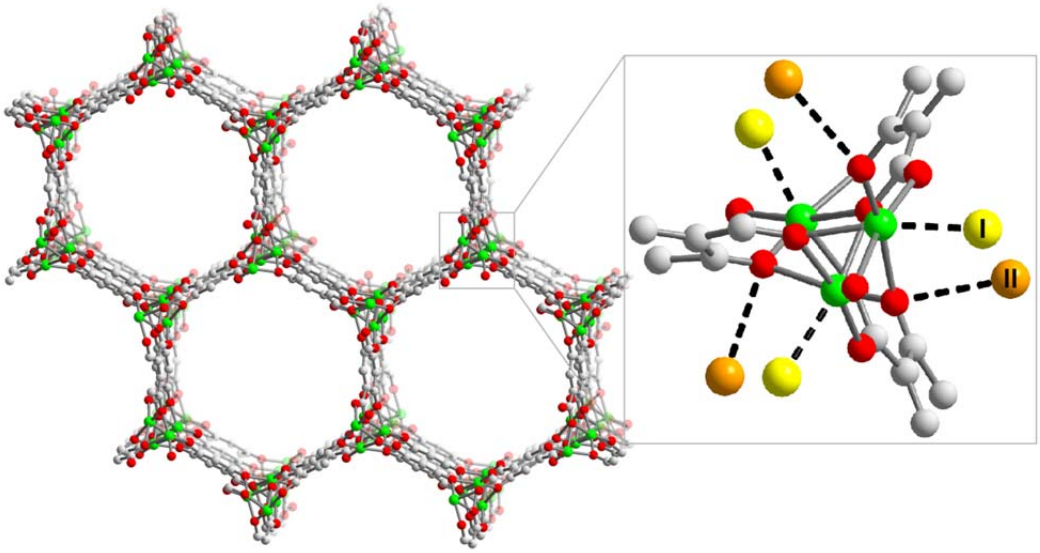


***Figure 4.1.*** A portion of the crystal structure of $Mg_2$(dobdc) as viewed down the [001] direction. Green, gray, and red spheres represent Mg, C, and O atoms, respectively; H atoms omitted for clarity. Inset:$D_2$ binding sites (site I: yellow, site II: orange) as determined by neutron diffraction.

## 4.3 Results and Discussion

The solvated form of $Mg_2$(dobdc) was prepared using a synthesis adapted from the literature procedure.[7d] Activation was performed by heating the material in anhydrous DMF followed by anhydrous methanol, and heating the material in vacuo at 180 °C. The BET surface area[17] of 1510(5) $m^2/g$ for a material activated under the optimized conditions is close to the accessible surface area[18] of 1705 $m^2/g$, indicating the full evacuation of the pores.

The lower-pressure $H_2$ adsorption isotherms for an activated sample of $Mg_2$(dobdc) are presented in Figure 4.2. Remarkably, the $H_2$ uptake at 77 K reaches 1 wt % at just 0.02 bar, presumably due to the high density of open metal sites within the structure. In addition, the relatively high surface area leads to the $H_2$ uptake (1 bar) of 2.2 wt % and 1.7 wt % at 77 K and 87 K, respectively. The zero-coverage isosteric heat of adsorption ($Q_{st}$) of –10.3(2) kJ/mol evaluated using a virial-type fitting to the isotherm data is indicative of the polarizing nature of the exposed $Mg^{2+}$ cations, and the gradual decrease of $Q_{st}$ to –7.9(2) kJ/mol at an adsorption level of 1 wt % is consistent with the gradual saturation of these sites.

The corresponding high-pressure $H_2$ adsorption isotherms recorded at 77 K and 298 K are shown in Figure 4.3. At 77 K, the excess adsorption saturates at a maximum of 3.2 wt % at 15 bar, and the total adsorption reaches 4.9 wt % and 45 g/L at 100 bar. The volumetric storage capacity at 100 bar constitutes a 44% increase over the corresponding density of pure $H_2$ gas, and is a result of the close approach of $H_2$ to the framework surface facilitated by the $Mg^{2+}$ centers. Surprisingly, despite the high density of unsaturated metal sites, the total adsorption at 298 K is

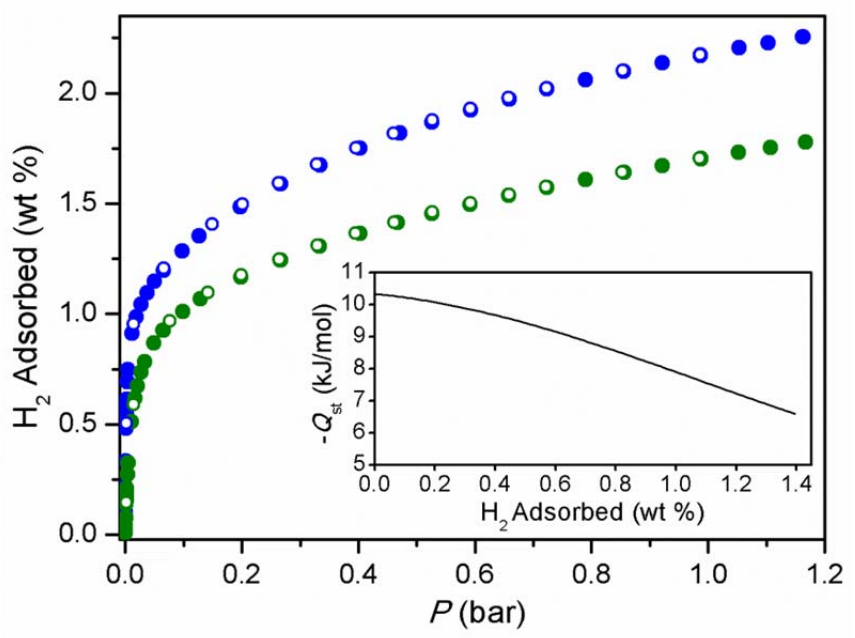


***Figure 4.2.*** Lower-pressure $H_2$ isotherms recorded at 77 K (blue) and 87 K (green). Filled and open symbols represent adsorption and desorption, respectively. Inset: Isosteric heat of adsorption ($Q_{st}$) as a function of $H_2$ adsorbed.

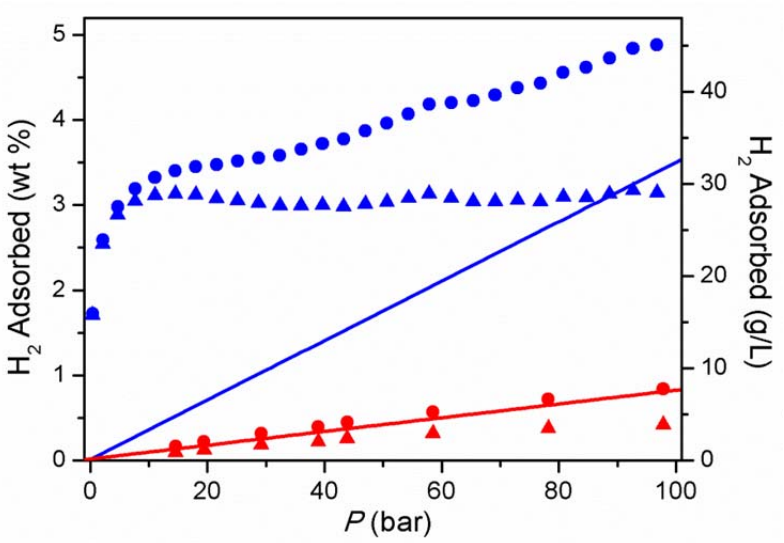


***Figure 4.3.*** High-pressure $H_2$ isotherms recorded at 77 K (blue) and 298 K (red). Triangles and circles represent excess and total uptake, while the solid lines show the density of pure $H_2$ gas.

just 0.8 wt % and 7.5 g/L1 at 100 bar, representing just a marginal improvement over the corresponding storage density of compressed $H_2$ gas.

The site-specific binding enthalpy at the open $Mg^{2+}$ adsorption site was probed through variable-temperature infrared spectroscopy. Upon cooling of a sample of $Mg_2$(dobdc) exposed to $H_2$, the evolution of two absorption bands centered at 4091 and 4085 $cm^{-1}$ is observed as shown in Figure 4.4. These bands can be, respectively, assigned to para-$H_2$ (*p*-$H_2$) and ortho-$H_2$ (*o*-$H_2$) owing to their expected frequency difference (6 $cm^{-1}$ for gas phase $H_2$), and by the observation of a spectral change at low temperature (ca. 20 K) and decreased equilibrium pressure. The integrated infrared absorbance was used to generate a van't Hoff-type plot, from which the standard adsorption enthalpy ($\Delta H^0$ = –12.1 ± 1.0 kJ/mol) and entropy ($\Delta S^0$ = –137 ± 10 J/(K·mol)) could be determined. The large magnitude of $\Delta H^0$ is consistent with the close approach of $H_2$ to the exposed $Mg^{2+}$ cations. Note that this value lies slightly below the corresponding value of –13.5 kJ/mol for $Ni_2$(dobdc),[19] likely as a result of the slightly larger ionic radius (and lower charge density) of $Mg^{2+}$ (0.72 Å) compared to $Ni^{2+}$ (0.69 Å). Meanwhile, the negative sign of $\Delta S^0$ is presumably a result of the more efficient packing and limited mobility of the adsorbed molecules compared to the bulk gas, owing to the close approach and localized adsorption of $H_2$.[20]

The loading-dependent $H_2$ adsorption characteristics were probed using powder neutron diffraction experiments performed at the BT-1 high-resolution diffractometer at the National Institute of Standards and Technology Center for Neutron Research (NCNR). At a loading of 0.6 $D_2$ per $Mg^{2+}$ site, the nuclear density map indicates the highest-affinity adsorption site to be just 2.45(4) Å from the metal center (see Figure 4.1). Note that this distance is in close agreement with the theoretically calculated distance of 2.50 Å evaluated using density functional theory.[21] At the same loading, a secondary binding site approximately 3.5 Å from the oxido group of the organic linker could be identified. Two further sites were located within the structure at higher loadings, although their distance from the framework surface (>4.0 Å) suggests only very weak

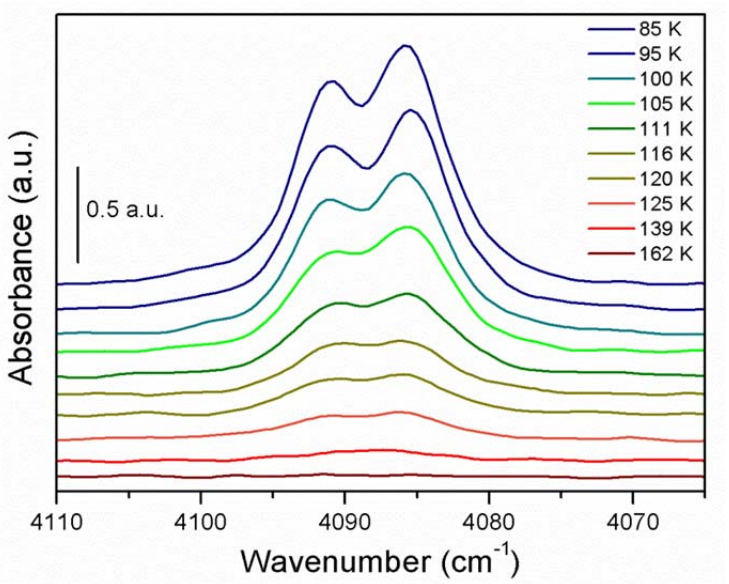


***Figure 4.4.*** Variable-temperature infrared spectra of $H_2$ adsorbed on activated $Mg_2$(dobdc) in the temperature range of 85 to 162 K.

interactions that are physisorptive in nature. These observations are also supported by the infrared spectra collected at similarly low temperatures.

Selected inelastic neutron scattering spectra collected at the BT-4 filter analyzer neutron spectrometer[12] (FANS) at the NCNR are shown in Figure 4.5. The spectrum recorded at 4 K for the evacuated material is dominated by vibrational modes of the ligand, and bears close resemblance to the corresponding spectrum of $Zn_2$(dobdc).[22] The material was then dosed with 0.6 *p*-$H_2$ per $Mg^{2+}$ site, resulting in three new features in the spectra at approximately 6.8, 10.4, and 24.1 meV. These new peaks are attributed to the splitting of the $J = 1$ rotational level of $H_2$ upon association with the open metal site. Upon increasing the loading to 1.2 *p*-$H_2$ per $Mg^{2+}$ site, additional features between 15 and 20 meV are observed, and are attributable to $H_2$ adsorbed at site II.[22] The analogous data for normal-$H_2$ (*n*-$H_2$), which is a mixture of approximately 75% *o*-$H_2$ and 25% *p*-$H_2$, reveal three additional peaks at 14.1, 18.0, and 27.3 meV, respectively. These peaks are presumably a result of the coupling of $H_2$ in the $J = 1$ rotational state with the hydrogen phonons.

The corrected neutron scattering data[13] collected on the disk-chopper spectrometer[14] (DCS) at the NCNR for a loading of 1.2 *n*-$H_2$ per $Mg^{2+}$ site are displayed in Figure 4.6. As reported recently,[7f] the rotational lines observed in neutron energy loss at 6.8 meV and 10.2 meV are not symmetrical, and only a single peak at –6.5 meV is observed with an intensity reduced by a factor of 9.[23] In the previous work, the absence of the peak at approximately –10 meV was ascribed to the presence of multiple binding sites at the $Mg^{2+}$ site. However, we note that there is a quantum-mechanically allowed thermal population of the $J = 1$ sub-levels, wherein the lowest J = 1 sub-level is populated at 4 K. Such an interpretation allows the INS data to be described with just one type of $H_2$ adsorption site at the $Mg^{2+}$ center, which is in agreement with the powder neutron diffraction data. The diffusional behavior of $H_2$ within the one-dimensional channels of $Mg_2$(dobdc) was studied by quasielastic neutron scattering (QENS). Surprisingly, at a dosing of 0.33 *n*-$H_2$ per $Mg^{2+}$ site, a QENS signal that is virtually indistinguishable from the resolution function of the instrument was obtained. This suggests the absence of $H_2$ diffusion on the

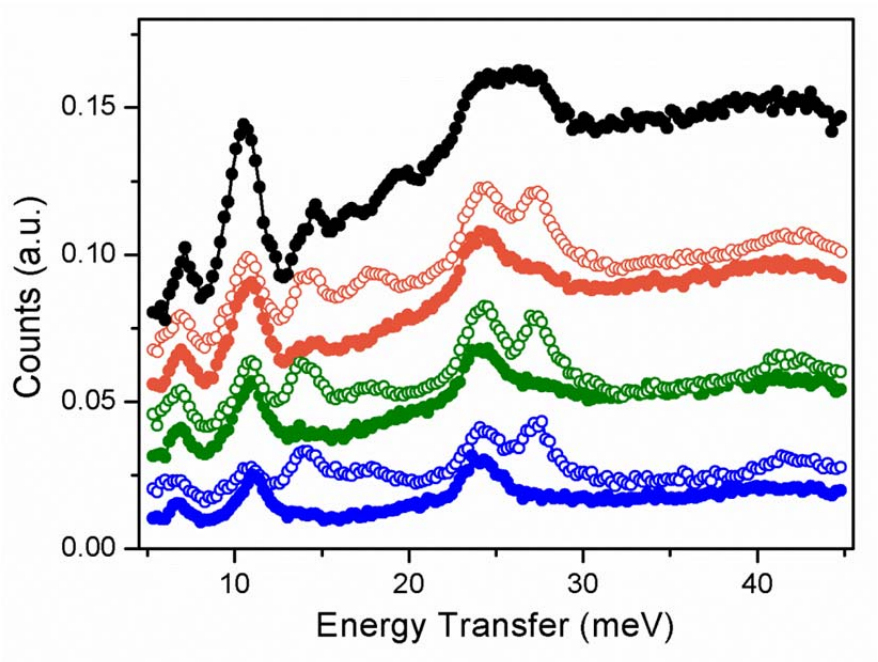


***Figure 4.5.*** Selected INS spectra recorded at 4 K following subtraction of the spectrum of evacuated $Mg_2(dobdc)$ for loadings of 0.2 (blue), 0.4 (green), 0.6 (orange), and 1.2 (black) $H_2$ molecules per $Mg^{2+}$ site. Filled and open symbols represent data for *p*-$H_2$ and *n*-$H_2$, respectively.

picosecond timescale owing to the strong interaction between $H_2$ and the exposed $Mg^{2+}$ cations. However, the spectrum becomes successively broadened at higher loadings, indicative of the diffusion of $H_2$ associated with the weaker binding sites and bulk $H_2$ within the channels, respectively.

The Q-dependent spectra were fit to a hydrogen diffusion model composed of two Lorentzian functions (narrow and broad) along with an elastic contribution that was convoluted with the instrument resolution function. The elastic response partially originates from stationary $H_2$, the narrow function originates from $H_2$ diffusing along the pore surface, and the broad function arises from bulk-like gas diffusing through the one-dimensional pores. The extracted line widths of the narrow component are indicative of a liquid-like jump-diffusion with no distinct spatial orientation of the jump direction as observed in other studies of $H_2$ within porous media.[24] Interestingly, the diffusion coefficients ($D$ = 1.2(1) × $10^{-8}$ $m^2/s$ at low loading; $D$ = 0.51(2) × $10^{-8}$ $m^2/s$ at 1 bar) derived from the fittings is an order of magnitude lower than the one-dimensional diffusion of $H_2$ in Cr(OH)(bdc) ($bdc^{2-}$ =1,4-benzenedicarboxylate; MIL-53(Cr)) and VO(bdc) (MIL-47(V)) under similar conditions,[25] and of similar magnitude to $H_2$ diffusing on a carbon surface.

## 4.4 Outlook

The foregoing results describe the hydrogen storage properties of $Mg_2(dobdc)$ as studied by adsorption experiments, infrared spectroscopy, and neutron scattering studies. The complementary nature of these techniques has afforded a complete picture of the $H_2$ adsorption

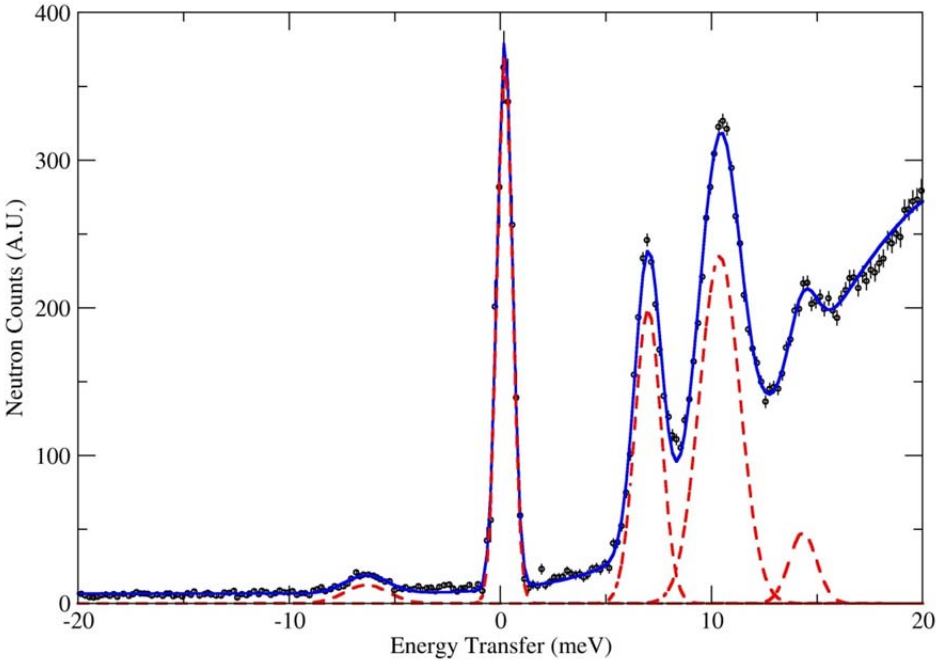


***Figure 4.6.*** DCS data measured at 1.81 Å for 1.2 n-$H_2$ per $Mg^{2+}$ site (black symbols) fit (blue line) to a series of Gaussian peaks (dashed red line) and a quadratic background. Vertical error bars indicate one standard deviation from counting statistics.

within the material, and has revealed an alternative interpretation to the INS data recently reported, in which the data can be completely described by a single type of adsorption site at the exposed $Mg^{2+}$ cation. We envisage that further studies of this type will afford a clearer understanding of the effect of the chemical and structural features of metal‑organic frameworks on the $H_2$ storage properties at ambient temperatures.

## 4.5 Acknowledgments

This work was supported by the Department of Energy under Contract No. DE-AC02-05CH11231. I thank Fulbright New Zealand for partial financial support.

## 4.6 References and Notes


(1) (a) Eddaoudi, M.; Kim, J.; Rosi, N.; Vodak, D.; Wachter, J.; O'Keeffe, M.; Yaghi, O. M. *Science* **2002**, *295*, 469. (b) Kitagawa, S.; Kitaura, R.; Noro, S.-I. *Angew. Chem., Int. Ed.* **2004**, *43*, 2334. (c) Millward, A. R.; Yaghi, O. M. *J. Am. Chem. Soc.* **2005**, *127*, 17998. (d) Furukawa, H.; Miller, M. A.; Yaghi, O. M. *J. Mater. Chem.* **2007**, *17*, 3197. (e) Férey, G. *Chem. Soc. Rev.* **2008**, *37*, 191. (f) Ma, S.; Sun, D.; Simmons, J. M.; Collier, C. D.; Yuan, D.; Zhou, H.-C. *J. Am. Chem. Soc.* **2008**, *130*, 1012. (g) Morris, R. E.; Wheatley, P. S. *Angew. Chem., Int. Ed.* **2008**, *47*, 4966. (h) Murray, L. J.; Dincă, M.; Long, J. R. *Chem. Soc. Rev.* **2009**, *38*, 1294 and references therein.

(2) EERE: Hydrogen, Fuel Cells, & Infrastructure Technologies Program: http://www.eere.energy.gov/hydrogenandfuelcells, (accessed August 2010).

(3) (a) Latroche, M.; Surblé, S.; Serre, C.; Mellot-Draznieks, C.; Llewellyn, P. L.; Lee, J.-H.; Chang, J.-S.; Jhung, S. H.; Férey, G. *Angew. Chem., Int. Ed.* **2006**, *45*, 8227. (b) Kaye, S. S.; Dailly, A.; Yaghi, O. M.; Long, J. R. *J. Am. Chem. Soc.* **2007**, *129*, 14176. (c) Sumida, K.; Hill, M. R.; Horike, S.; Dailly, A.; Long, J. R. *J. Am. Chem. Soc.* **2009**, *131*, 15120. (d) Koh, K.; Wong-Foy, A. G.; Matzger, A. J. *J. Am. Chem. Soc.* **2009**, *131*, 4184.

(4) Bhatia, S. K.; Myers, A. L. *Langmuir* **2006**, *22*, 1688.

(5) Note that the consideration of an enthalpy–entropy correlation for H2 adsorption in metal–organic frameworks results in an even greater magnitude for the optimal enthalpy of adsorption (–20 to –25 kJ/mol): (a) Garrone, E.; Bonelli, B.; Otero Areán, C. *Chem. Phys. Lett.* **2008**, *456*, 68. (b) Otero Areán, C.; Chavan, S.; Cabello, C. P.; Garrone, E.; Palomino, G. T. *ChemPhysChem* **2010**, *11*, 3237.

(6) (a) Dincă, M.; Long, J. R. *J. Am. Chem. Soc.* **2005**, *127*, 9376. (b) Vimont, A.; Goupil, J.-M.; Lavalley, J.-C.; Daturi, M.; Surblé, S.; Serre, C.; Millange F.; Férey, G.; Audebrand, N. *J. Am. Chem. Soc.* **2006**, *128*, 3218. (c) Moon, H. R.; Kobayashi, N.; Suh, M. P. *Inorg. Chem.* **2006**, *45*, 8672. (d) Dincă, M.; Dailly, A.; Liu, Y.; Brown, C. M.; Neumann, D. A.; Long, J. R. *J. Am. Chem. Soc.* **2006**, *128*, 16876. (e) Sumida, K.; Horike, S.; Kaye, S. S.; Herm, Z. R.; Queen, W. L.; Brown, C. M.; Grandjean, F.; Long, G. J.; Dailly, A.; Long, J. R. *Chem. Sci.* **2010**, *1*, 184.

(7) (a) Dietzel, P. D. C.; Morita, Y.; Blom, R.; Fjellvag, H. *Angew. Chem., Int. Ed.* **2005**, *44*, 6354. (b) Rosi, N. L.; Kim, J.; Eddaoudi, M.; Chen, B.; O'Keeffe, M.; Yaghi, O. M. *J. Am. Chem. Soc.* **2005**, *127*, 1504. (c) Dietzel, P. D. C.; Panella, B.; Hirscher, M.; Blom, R.; Fjellvag, H. *Chem. Commun.* **2006**, 959. (d) Caskey, S. R.; Wong-Foy, A. G.; Matzger, A. J. *J. Am. Chem. Soc.* **2008**, *130*, 10870. (e) Dietzel, P. D. C.; Blom, R.; Fjellvag, H. *Eur. J. Inorg. Chem.* **2008**, 3624. (f) Dietzel, P. D. C.; Georgiev, P. A.; Eckert, J.; Blom, R.; Strässle, T.; Unruh, T. *Chem. Commun.* **2010**, *46*, 4962.

(8) Garrone, E.; Arean C. O. *Chem. Soc. Rev.* **2005**, *34*, 846.

(9) Toby, B. H. *J. Appl. Cryst*. **2001**, *34*, 210.

(10) Liu, Y.; Kabbour, H.; Brown, C. M.; Neumann, D. A.; Ahn, C. C. *Langmuir* **2008**, *24*, 4772.

(11) Brown, C. M.; Liu, Y.; Yildirim, T.; Peterson, V. K.; Kepert, C. J. *Nanotechnology* **2009**, 204025.

(12) Udovic, T. J.; Brown, C. M.; Leao, J. B.; Brand, P. C.; Jiggetts, R. D.; Zeitoun, R.; Pierce, T. A.; Peral, I.; Copley, J. R. D.; Huang, Q.; Neumann, D. A.; Fields, R. J. *Nuclear Inst. and Methods in Physics Research, A* **2008**, *588*, 406.

(13) Azuah, R. T.; Kneller, L. R.; Qiu, Y.; Tregenna-Piggott, P. L. W.; Brown, C. M.; Copley, J. R. D.; Dimeo, R. M. *J. Res. Natl. Inst. Stan. Technol.* **2009**, *114*, 241.
(14) Copley, J. R. D.; Cook, J. C. *Chem. Phys.*, **2003**, *292*, 477.
(15) Accessible Surface Area Calculation Program (accessed August 2009): http://www.see.ed.ac.uk/~tduren/research/surface_area/.
(16) Rappe, A. K.; Casewit, C. J.; Colwell, K. S.; Goddard, W. A.; Skiff, W. M. *J. Am. Chem. Soc.* **1992**, *114*, 10024.
(17) Walton, K. S.; Snurr, R. Q. *J. Am. Chem. Soc.* **2007**, *129*, 8552.
(18) Düren, T.; Millange, F.; Férey, G.; Walton, K. S.; Snurr, R. Q. *J. Phys. Chem. C* **2007**, *111*, 15350.
(19) Vitillo, J. G.; Regli, L.; Chavan, S.; Ricchiardi, G.; Spoto, G.; Dietzel, P. D. C.; Bordiga, S.; Zecchina, A. *J. Am. Chem. Soc.* **2008**, *130*, 8386.
(20) Liu, Y.; Kabbour, H.; Brown, C. M.; Neumann, D. A.; Ahn, C. C. *Langmuir* **2008**, *24*, 4772.
(21) Zhou, W.; Wu, H.; Yildirim, T. *J. Am. Chem. Soc.* **2008**, *130*, 15268.
(22) Kong, L.; Román-Pérez, G.; Soler, J. M.; Langreth, D. C. *Phys. Rev. Lett.* **2009**, *103*, 096103.
(23) Young, J. A.; Koppel, J. U. *Phys. Rev. A* **1964**, *135*, 603.
(24) (a) Bienfait, M.; Zeppenfeld, P.; Ramos, R. C.; Gay, J. M.; Vilches, O. E.; Coddens, G. *Phys. Rev. B* **1999**, *60*, 1773. (b) Narehood, D. G.; Pearce, J. V.; Eklund, P. C.; Sokol, P. E.; Lechner, R. E.; Pieper, J.; Copley, J. R. D.; Cook, J. C. *Phys. Rev. B* **2003**, *67*, 5. (c) Haas, O. E.; Simon, J. M.; Kjelstrup, S.; Ramstad, A. L.; Fouquet, P. *J. Phys. Chem. C* **2008**, *112*, 3121.
(25) Salles, F.; Kolokolov, D. I.; Jobic, H.; Maurin, G.; Llewellyn, P. L.; Devic, T.; Serre, C.; Férey, G. *J. Phys. Chem. C* **2009**, *113*, 7802.

# Chapter 5: Neutron Scattering and Spectroscopic Studies of Hydrogen Adsorption in $Cr_3(BTC)_2$ – A Metal-Organic Framework with Exposed $Cr^{2+}$ Sites

## 5.1 Introduction

Metal-organic frameworks have attracted significant interest in recent years, in part owing to their potential applications in gas storage, molecular separations, and heterogeneous catalysis.[1] In particular, the ability to construct these materials from the combination of a judiciously selected metal ion and organic bridging unit may provide a versatile platform for the preparation of materials possessing physical and chemical properties that are finely-tuned for specific applications. With regard to hydrogen storage for mobile applications, gravimetric and volumetric storage densities approaching those prescribed by the U. S. Department of Energy[2] have been observed within the highest surface-area metal-organic frameworks at cryogenic temperatures.[3] However, the storage capacity within these materials greatly diminishes at ambient temperature owing to the weak physisorptive interactions that predominate between $H_2$ and the framework surface. Indeed, the zero-coverage isosteric heat of adsorption within these materials typically lies in the range of –5 to –7 kJ/mol, which is far below the –15 kJ/mol considered optimal for an adsorbent operating between 1.5 and 30 bar at 298 K.[4] Furthermore, the inclusion of an enthalpy-entropy correlation increases this magnitude even further, suggesting an optimal enthalpy of adsorption in the range –20 to –25 kJ/mol.[5]

One strategy for improving the isosteric heat of $H_2$ adsorption within metal-organic frameworks is the synthesis of materials possessing open metal cation sites on the pore surface.[6] Here, the charge of the cation serves to induce a dipole on the $H_2$ molecule, resulting in an

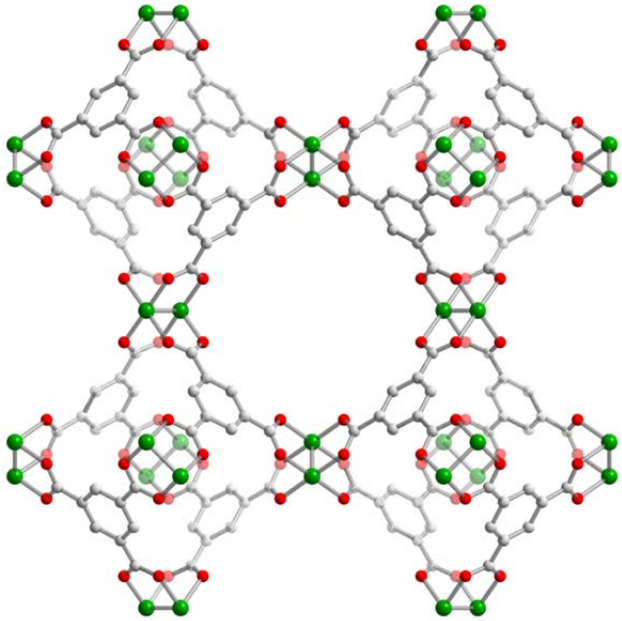

***Figure 5.1.*** A portion of the crystal structure of evacuated $Cr_3(BTC)_2$. Green, gray, and red spheres represent Cr, C, and O atoms, respectively. Hydrogen atoms have been omitted for clarity.

electrostatic interaction that is stronger than the dispersion-type interactions that predominate for physisorbed molecules.[6,7] Indeed, a zero-coverage isosteric heat of $H_2$ adsorption as high as –15.1 kJ/mol has been demonstrated within the material $Co_4(H_2O)_4(MTB)_2$ ($H_4MTB$ = methanetetrabenzoic acid), which features unsaturated $Co^{2+}$ sites following activation.[8] However, in this case the isosteric heat rapidly decreases as a function of surface coverage, indicating that the density of strong binding sites is a crucial factor in facilitating large $H_2$ storage capacities at 298 K.[9] Thus, increasing the density of open metal sites remains a significant synthetic challenge, and a substantial body of recent computational work has been devoted to identifying potential candidate materials.[10]

The microporous metal-organic framework $Cr_3(BTC)_2$ (Figure 5.1, $H_3BTC$ = 1,3,5-benzenetribenzoic acid),[11] features a cubic network (space group: *Fm*–3*m*) of dinuclear paddlewheel units linked by triangular $BTC^{3-}$ organic bridging units to form a (3,4)-net that is isostructural with $Cu_3(BTC)_2$ (HKUST-1).[12] Here, six paddlewheel units and four $BTC^{3-}$ ligands form octahedral cages that share vertices to form a three-dimensional pore system resembling the boracite net topology. Upon desolvation of the solid by heating *in vacuo*, the material possesses unsaturated $Cr^{2+}$ sites at the paddlewheel units. The presence of these sites has recently been demonstrated to afford tremendous adsorption selectivity for $O_2$ over $N_2$, owing to the ability of the metal centers to engage in a partial electron transfer with $O_2$, but not $N_2$.[8] Although such an interaction was not expected to occur with $H_2$, the high charge density at these coordination sites could still be of benefit for $H_2$ adsorption. Herein, we report the $H_2$ storage properties of $Cr_3(BTC)_2$, as probed through low-pressure adsorption experiments, infrared spectroscopy, and neutron scattering studies. The complementary nature of the experiments offers a greater depth in the description of $H_2$ adsorption within the material, and results in a more complete understanding of the influence of various chemical and structural features on the adsorption properties.

## 5.2 Experimental Section

**General Considerations.** $Cr_3(BTC)_2$ was synthesized and activated according to the literature procedure.[11] All reagents were obtained from commercial vendors, and used without further purification. All powder X-ray diffraction patterns were collected using a Bruker D8 Advance diffractometer (Cu $K_\alpha$; $\lambda$ = 1.5406 Å) equipped with a capillary stage. Owing to the air- and moisture-sensitivity of $Cr_3(BTC)_2$, all manipulations were performed within a glove box under a dinitrogen or argon atmosphere. Note that even brief exposure of the compound to the air induces an immediate color change of the solid to a dark forest green color, which is accompanied by a loss of crystallinity and porosity. The isosteric heat of $H_2$ adsorption was calculated using the method reported previously.[6f]

**Low-Pressure Gas Sorption Measurements.** Glass sample tubes of a known weight were loaded with approximately 100 mg of sample, and sealed using a TranSeal. Samples were degassed at 160 °C for 24 h on a Micromeritics ASAP 2020 analyzer until the outgas rate was no more than 1 mTorr/min. The degassed sample and sample tube were weighed precisely and then transferred back to the analyzer. The outgas rate was again confirmed to be less than 1 mTorr/min. $H_2$ adsorption isotherms were measured at 77 K in a liquid nitrogen bath, and at 87 K in a liquid argon bath. The isosteric heat of adsorption was obtained using a virial-type fitting to the data as described previously.

**Neutron Powder Diffraction Measurements.** Neutron powder diffraction data were collected on the high resolution neutron powder diffractometer BT-1 at the National Institute of Standards and Technology (NIST) Center for Neutron Research (NCNR) with a Ge-(311) monochromator and using in-pile collimation of 15 min of arc, corresponding to a wavelength of 2.0782 Å. Measurements were taken as a function of deuterium loading (0.5, 1.0, 1.5, 2.0, and 3.0 $D_2$ molecules per $Cr^{2+}$ site, loading performed at ca. 60 K) at a temperature of ca. 4 K with a measurement time of ca. 9 h.

All sample transfers were performed in a helium-filled glovebox equipped with water and oxygen monitors. Initial sample activation was performed in a glass tube with a packless bellows valve attached. The sample was evacuated using a turbomolecular pump ($10^{-5}$ Torr) and heated to 150 °C for 48 h, after which time the sample was cooled and transferred to a cylindrical vanadium can equipped with a capillary gas line and a packless valve, and sealed with an indium O-ring. The sample was mounted onto a sample stick equipped with a stainless-steel gas line with an additional valve for a top-loading closed-cycle helium refrigerator. The sample was further degassed *in-situ* under high vacuum to remove residual helium. During the experiments, a known amount of hydrogen (deuterium) gas was loaded into the sample (1.174 g), which was typically maintained at a temperature of 60 K (CCR) until no pressure drop was observed for at least 1 min. The sample was then cooled down to the base temperature of 3.5 K over a period of 1 h in order to perform measurements. In all cases, the outgas pressure reading was zero well before reaching 25 K.

Neutron powder diffraction patterns were analyzed using the Rietveld refinement method. The program EXPGUI[13] incorporating the Rietveld program GSAS[14] was used to perform all refinements. The model of the bare material was refined first, and was used as the starting point for subsequent refinements of the $D_2$-loaded samples. In all cases, $D_2$ molecules were treated as point scatters with double occupancy in accord with the rotationally-disordered quantum mechanical molecule.[15] The coordinates of all other atoms and the displacement parameters were allowed to vary during the refinement of each $D_2$ loading case. Based on the structure obtained from the diffraction pattern of the bare material, the diffraction patterns of the first $D_2$-loaded case (0.5 $D_2$ molecules per $Cr^{2+}$) was analyzed by firstly neglecting the $D_2$ molecules. The Fourier difference maps were calculated, clearly indicating the positions of $D_2$ adsorption sites. Accurate values for the $D_2$ locations and occupancy numbers were then obtained by Rietveld refinement after incorporating the $D_2$ molecules into the structure model. For each successive $D_2$ loading, the Fourier difference map was calculated on the basis of the results of the previous $D_2$ loading and used to identify new $D_2$ adsorption sites.

**Inelastic Neutron Scattering (INS) Spectroscopy.** The INS spectra were measured at 4 K using the pyrolytic graphite monochromator and 20'-20' collimation options on the BT-4 filter analyzer neutron spectrometer (FANS)[16] at the NCNR. The sample (1.174 g) was sealed in a cylindrical aluminum cell suitable for *in-situ* gas loading while cooled in a CCR. $H_2$ gas was used during the measurements to take advantage of its large incoherent neutron scattering cross section. Note that the $H_2$ molecule is a very good quantum rotor due to its light mass and consists of two indistinguishable fermions (protons) that require the wavefunction to be antisymmetric. If the nuclear spins of two protons are anti-parallel, $H_2$ is said to be in a *para* state (*p*-$H_2$); otherwise, it is in an *ortho* state (*o*-$H_2$). The quantum rotation number, $J$, of a $H_2$ molecule thus has to be even for a *para*-$H_2$ and odd for an *ortho*-$H_2$. At room temperature, only one fourth of $H_2$ molecules are in the *para* state. Usually, the conversion rate between states is very slow, but

can be greatly accelerated in the presence of a fluctuating magnetic moment. Both *p*-$H_2$ and normal $H_2$ (*n*-$H_2$), which consists of 25 % *p*-$H_2$ and 75% *o*-$H_2$, were used in these experiments.

A neutron scattered by a $H_2$ molecule can induce the required nuclear spin flip to convert a *para*/*ortho* $H_2$ to an *ortho*/*para* $H_2$. This *para-ortho* or *ortho-para* transition is associated with the change of the rotational quantum number, *J*, from even/odd to odd/even, and has a large neutron scattering cross-section that is proportional to the incoherent neutron scattering cross-section of the proton. INS spectra of the adsorbed $H_2$ were obtained by subtracting the INS spectrum of the bare materials. For a free hydrogen molecule, the *para-ortho* transition is usually associated with the $J = 0$ to $J = 1$ excitation occurring with an energy of 14.7 meV, which can be directly measured by INS but not optical spectroscopies. The local potential of a host material will generate rotational barriers for the adsorbed $H_2$ which typically cause the $J = 1$ state to split into its three sub-levels. Additionally, the translation excitations of the $H_2$ molecule may be coupled to the rotational transition and complicate the observed spectra. Hence, the INS spectra of adsorbed $H_2$ may show complex features with multiple peaks in the spectrum containing rich information about the host material and the hydrogen interactions.

Loadings of 0.5, 1.0, 2.0, and 3.0 *p*-$H_2$ and *n*-$H_2$ per $Cr^{2+}$ site were performed at 70 K with data collection at 4 K. Data were collected for approximately 9 h per loading. The energy resolution is between 1.2 meV to 2.0 meV over the energy transfer ranges accessible. Data reduction, including the subtraction of the bare $Cr_3(BTC)_2$ spectrum from the $H_2$-loaded spectra, and peak fitting, were performed within the DAVE software suite.[17]

**Infrared Spectroscopy.** Infrared spectra were acquired using a Bomem DA3 Michelson interferometer equipped with a quartz-halogen source, $CaF_2$ beamsplitter and a liquid nitrogen cooled mercury-cadmium-telluride detector. A custom-built diffuse reflectance system[18] with a sample chamber that allows both the temperature and atmosphere of the material to be controlled was utilized for all experiments. Powder samples of $Cr_3(BTC)_2$ (ca. 10 mg) were transferred under inert atmosphere to a cup affixed to a copper slab providing thermal contact to a cold-finger cryostat (Janis ST-300T). The sample temperature was monitored by a Si-diode thermometer placed directly within the sample cup. Prior to introduction of the hydrogen gas,

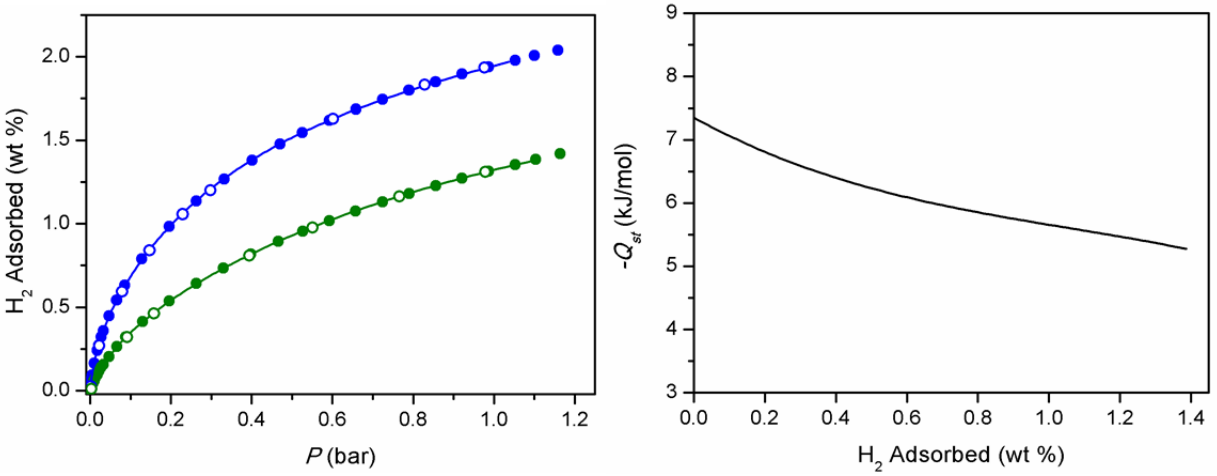


***Figure 5.2.*** (a) Lower-pressure $H_2$ isotherms in $Cr_3(BTC)_2$ collected at 77 K (blue) and 87 K (green). Closed and open symbols represent adsorption and desorption, respectively, and the solid lines represent a virial-type fitting to the data. (b) A plot of the isosteric heat of adsorption as a function of $H_2$ coverage.

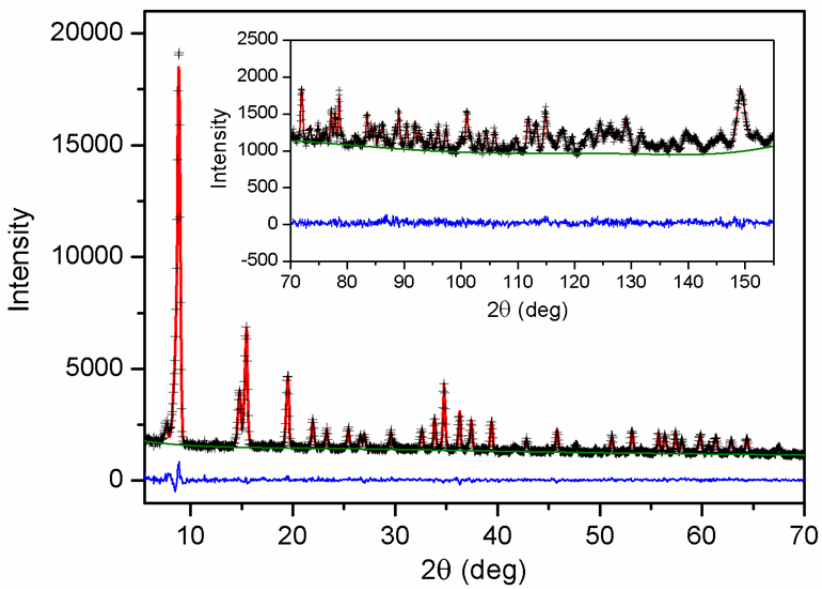


***Figure 5.3.*** Representative neutron powder diffraction data, collected for $Cr_3(BTC)_2$ following a dosing of 0.5 $D_2$ molecules per $Cr^{2+}$ site. Green lines, crosses, and red lines represent the background, experimental, and calculated diffraction patterns, respectively. The blue line represents the difference between experimental and calculated patterns. The final Rietveld goodness-of-fit parameter was $\chi^2 = 0.9329$.

the samples were evacuated for several hours at room temperature. Known quantities of research grade (99.9999% purity) $H_2$ was dispensed from a calibrated gas manifold by monitoring the change in pressure.

## 5.3 Results and Discussion

**$H_2$ Adsorption Isotherms.** The $H_2$ adsorption isotherms collected for an activated sample of $Cr_3(BTC)_2$ are presented in Figure 5.2. The relatively high BET surface area of 1810 $m^2/g$ facilitates a reversible adsorption (1 bar) of 1.9 wt % and 1.3 wt % at 77 K and 87 K, respectively. The zero-coverage isosteric heat of adsorption ($Q_{st}$) for $H_2$ obtained from a virial-type fitting to the isotherm data of –7.4(2) kJ/mol represents just a slight increase in the magnitude of $Q_{st}$ compared to materials that do not feature exposed cation sites. As discussed below, the neutron powder diffraction data reveal that the $Cr^{2+}$ sites are occupied only at high loadings following a slight elongation of the Cr-Cr distance within the paddlewheel unit. As a result, this leads to the occupation of a single binding site that facilitates short contacts with the organic component of the framework at low coverage, which is consistent with the relatively small magnitude of $Q_{st}$. Note that this serves to highlight one of the primary disadvantages of the analysis of bulk isotherm data, as is often performed in adsorption studies, since conclusions regarding the binding environment of $H_2$ within the framework cannot be deduced directly, particularly in cases where the site-specific adsorption enthalpies of two or more sites within the unit cell are quite similar. Nevertheless, the value of $Q_{st}$ at zero-coverage is comparable to the corresponding value reported for $Cu_3(BTC)_2$ (–6.8 kJ/mol).[19] Consistent with the successive

occupancy of the strongest binding sites within $Cr_3(BTC)_2$, the magnitude of $Q_{st}$ gradually decreases to –5.7(2) kJ/mol at a $H_2$ uptake of 1.0 wt %. A complete analysis of the coverage-dependent adsorption characteristics and binding sites within the material is explored in detail below in the context of neutron powder diffraction, inelastic neutron scattering spectroscopy, and infrared spectroscopy.

**Neutron Powder Diffraction Data.** Rietveld analysis of the bare $Cr_3(BTC)_2$ material revealed the expected cubic network of dinuclear paddlewheel secondary building units bridged by 3-connected organic linkers (Figure 5.1). Significantly, the Cr-Cr distance of 2.06(2) Å is indicative of the presence of a metal-metal quadruple bond, and results in the $Cr^{2+}$ being situated approximately 0.11(2) Å below the four-atom mean plane formed by the oxygen atoms of the carboxylate ligands. We note that in the fully evacuated state, no nuclear density was observed on the axial coordination sites on the $Cr^{2+}$ centers, reflecting the removal of all of the coordinated solvent molecules, and full activation of the pores.

The $D_2$ binding sites within $Cr_3(BTC)_2$ were determined by successively dosing the evacuated material with $D_2$ at loadings corresponding to 0.5, 1.0, 1.5, 2.0, and 3.0 $D_2$ molecules per $Cr^{2+}$ center, and taking nuclear density Fourier difference maps between the loaded and evacuated materials. Any new locations were added to the Rietveld process where the final positions and occupancies of the $D_2$ molecules were allowed to refine freely. Note that at each loading level, the total refined occupancy of $D_2$ assigned from the neutron density map agrees well with the expected total occupancy, indicating full assignment of all of the binding sites within the unit

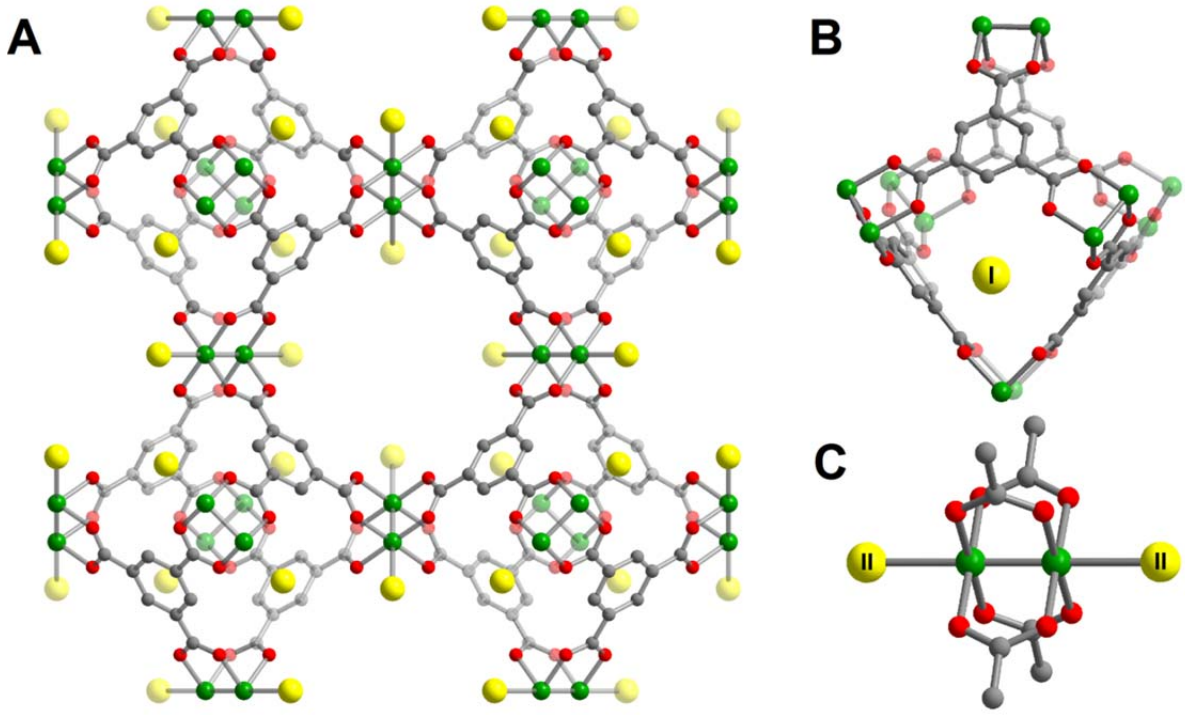


***Figure 5.4.*** A portion of the structure of $Cr_3(BTC)_2$ showing the first two $D_2$ binding sites, where green, red, and gray spheres represent, Cr, O, and C atoms, respectively, while large yellow spheres represent $D_2$ molecules (A). The first occupied position (site I) is located at the apertures of the octahedral cages (B), while at higher loadings, the unsaturated $Cr^{2+}$ center (site II) is occupied (C).

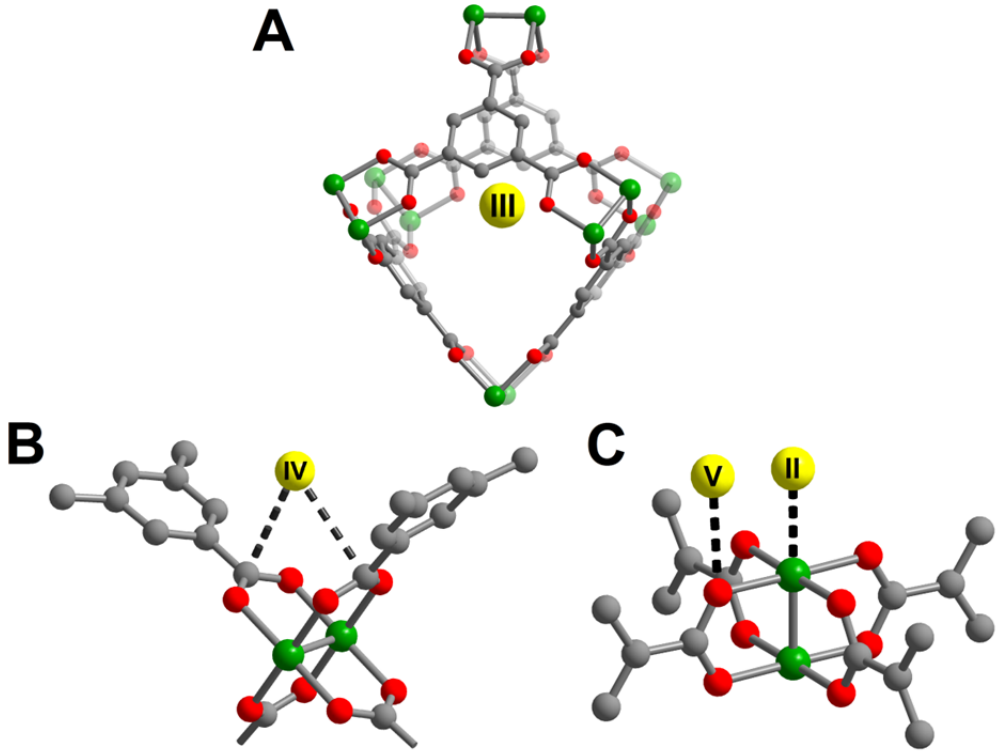


***Figure 5.5.*** $D_2$ binding sites III to V observed within $Cr_3(BTC)_2$ at higher loadings. Site III (A) lies in the center of the octahedral cages, site IV (B) resides within a V-shaped binding pocket between two $BTC^{3-}$ moieties, while site V (C) is situated in a close contact (ca. 2.7 Å) with the oxygen atom of the carboxylate group.

cell.

The neutron diffraction data and Rietveld refinement results for data collected at a loading of 0.5 $D_2$ molecules per $Cr^{2+}$ site are shown in Figure 5.3. Surprisingly, no nuclear density was observed at the open $Cr^{2+}$ site at this loading level, and the $D_2$ is located in the apertures of the octahedral cages at a distance of approximately 4 Å from the carbon atoms of the aryl rings of the $BTC^{3-}$ ligands (Figure 5.4B, site I). Upon increasing the loading to 1.0 $D_2$ molecules per $Cr^{2+}$ site, additional nuclear density was observed at site I, as well as a small quantity at the open $Cr^{2+}$ site (Figure 5.4C, site II). Here, the $D_2$ is disposed at a distance of 2.63(2) Å from the $Cr^{2+}$ center, which is significantly greater than the corresponding distance of 2.39(1) Å observed in $Cu_3(BTC)_2$,[20] and is also much greater than observed for other frameworks featuring exposed metal cation sites.[21] This is consistent with the larger ionic radius of $Cr^{2+}$ (0.80 Å; high spin) compared to $Cu^{2+}$ (0.73 Å), yielding a lower charge density and subsequently a weaker induced dipole on the adsorbed $D_2$ molecules.[22] Furthermore, the Cu···Cu distance in $Cu_3(BTC)_2$ is significantly longer than the Cr-Cr distance in $Cr_3(BTC)_2$, which results in the $Cu^{2+}$ ions projecting out into the pores of the framework. This likely allows the $D_2$ molecules to interact more directly with the metal centers due to the lower steric demand of these sites. Here, the apparent preference for $D_2$ to populate site I rather than site II at the lowest loadings is probably a result of a combination of the $Cr^{2+}$ binding site being sterically less accessible to guest molecules, and the binding energy at the open metal site being comparable to that of site I.

Nevertheless, to our knowledge, $Cr_3(BTC)_2$ is the first example of a metal-organic framework furnished with open metal sites wherein the metal center is not the favored binding site for $D_2$ at low coverages.

Interestingly, upon increasing the $D_2$ loading from 1.0 to 1.5 $D_2$ molecules per $Cr^{2+}$ center, an elongation of the Cr-Cr distance from 2.06(2) Å to 2.17(2) Å is observed, representing a decrease in the bond order of the Cr-Cr interaction. This serves to project the $Cr^{2+}$ cations above the four-atom mean plane of the O atoms of the carboxylate moieties. Importantly, this structural change is accompanied by a reorganization of the nuclear density after the next dosing step such that site II is fully populated, suggesting that the $D_2$ molecules are able to more readily access the open metal site once it is projected out into the channels. Note that the sample is warmed to approximately 60 K during each dosing step, allowing the $D_2$ molecules to migrate more rapidly to their preferred positions following the structural change. Furthermore, at this loading level, additional nuclear density is also observed at the center of the octahedral cages (site III in Figure 5.5), and is observed at full occupancy. As the loading is increased further to 2.0 and 3.0 $D_2$ molecules per $Cr^{2+}$ site, additional nuclear density is appears, corresponding to close contacts in the channels of the framework. As shown in Figure 5.5 site IV is positioned in a V-shaped binding pocket formed by two carboxylate moieties of the paddlewheel units, wherein the $D_2$ molecule is disposed approximately 3.3 Å from the framework surface. Meanwhile, site V is observed approximately 2.8 Å from the O atoms of the carboxylate moieties, although only a small occupancy is observed at this site even at the highest loadings. Previous studies performed on $Cu_3(BTC)_2$ revealed adsorption sites with coordinates and interaction distances similar to sites III-V observed here, which might be anticipated based on the isostructural nature of the two frameworks.

**Inelastic Neutron Scattering Spectra.** The $H_2$ loading characteristics of $Cr_3(BTC)_2$ were examined in further detail by inelastic neutron scattering. Data were collected at the same

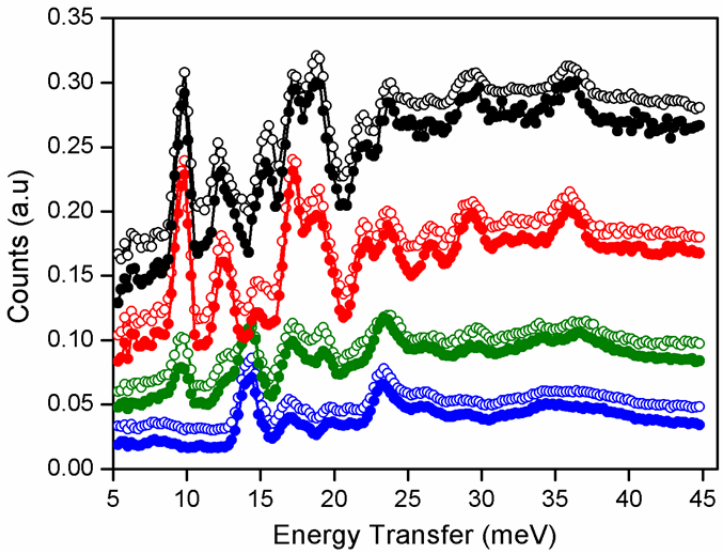


***Figure 5.6.*** Selected inelastic neutron scattering (INS) spectra recorded at 4 K following subtraction of the spectrum of evacuated $Cr_3(BTC)_2$ for loadings of 0.5 (blue), 1.0 (green), 2.0(red), and 3.0 (black) $H_2$ molecules per $Cr^{2+}$ site. Filled and open symbols represent data for *p*-$H_2$ and *n*-$H_2$, respectively.

loadings (0.5, 1.0. 2.0, and 3.0 $H_2$ molecules per $Cr^{2+}$ site) as for the powder neutron diffraction experiments to allow for the best opportunity for correlation of FANS spectra with the binding sites observed crystallographically. For all spectra, routine data reduction and subtraction of the spectrum for the evacuated form of $Cr_3(BTC)_2$ was performed, and selected spectra are displayed in Figure 5.6.

At the lowest loading of 0.5 $H_2$ per $Cr^{2+}$ site, a sharp peak is observed at 14.3 meV. This feature is consistent with the first transition between rotational energy levels, $J = 0 \rightarrow 1$, of an almost unhindered $H_2$ molecule, and presumably corresponds to the molecules located in the windows of the octahedral cages (site I). The lack of a significant shift for these molecules from the corresponding signal for free $H_2$ observed at 14.7 meV is presumably due to the relatively large distance between $H_2$ and the framework surface, resulting in only a small increase in the rotational barrier of the $H_2$ molecule upon occupation of site I. A broader feature is also observed at 23.0 meV, which is likely due to the rotation of $H_2$ coupled with a phonon of approximately 9 meV as observed in $Cu_3(BTC)_2$.[15] The overall similarity of the *n*-$H_2$ and *p*-$H_2$ spectra indicates that the normal hydrogen is converted from the $J = 1$ *ortho* form to the $J = 0$ *para* form, and this is mirrored for all loadings, even in the cases where the strongest accessible adsorption site is not the metal center. This suggests that virtually all of the $H_2$ molecules are able to approach the paramagnetic $Cr^{2+}$ ion with a sufficient proximity for *ortho-para* conversion.

Upon increasing the loading to 1.0 $H_2$ per $Cr^{2+}$ site, a sharp feature at 9.6 meV is observed. This peak is assigned to $H_2$ molecules bound to the unsaturated $Cr^{2+}$ sites (site II), which experience a significant rotational hindrance due to the close approach of these molecules to the framework surface, as observed in the powder neutron diffraction experiments. Rotational transitions are also apparent at energies close to this value for *p*-$H_2$ in $Cu_3(BTC)_2$ where the initial adsorption is at the metal center.[15] The corresponding growth of a peak at around 19 meV is clearly observed and was previously ascribed to a coupled rotation and phonon in $Cu_3(BTC)_2$, which is likely also the case here. The intensities of these peaks increase following subsequent loadings to 2.0 and 3.0 $H_2$ per $Cr^{2+}$ site, which is consistent with the eventual full occupation of molecules at this binding site.

**Infrared Spectra.** The adsorption of $H_2$ within $Cr_3(BTC)_2$ was further probed through the collection of variable-temperature infrared spectra. An activated sample of $Cr_3(BTC)_2$ was exposed to a total dosing of 4 $H_2$ per $Cr^{2+}$ center. As the sample temperature was decreased, the $H_2$ pressure dropped to a base value of 0.01 bar at 30 K, indicating that virtually all of the dosed gas had adsorbed onto the framework. The spectra collected at different temperatures during this procedure are presented in Figure 5.7. As the temperature is lowered from 88 K, the emergence of a single *ortho-para* pair corresponding to the H-H stretch for $H_2$ molecules bound to the framework surface is observed at 4110 and 4116 $cm^{-1}$, respectively. Here, the presence of only a single band at 88 K suggests the occupancy of a single crystallographic site within the unit cell, which, based on the neutron powder diffraction and INS experiments, is presumably the site located at the aperture of the octahedral cages (site I).[23]

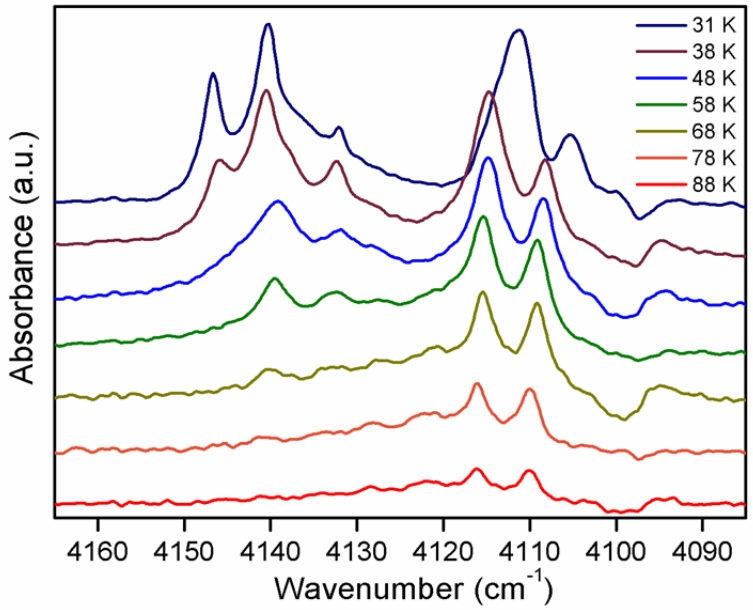


***Figure 5.7.*** Selected variable-temperature infrared spectra (Q-region) for $Cr_3(BTC)_2$ following dosing with $H_2$ collected at temperatures between 31 K and 88 K at a resolution of 1 $cm^{-1}$. Spectra are offset for clarity.

Upon cooling of the sample below 58 K, a second *ortho-para* pair is observed at 4132 and 4141 $cm^{-1}$, respectively. These bands are consistent with the occupation of a secondary binding site that is less-polarizing towards $H_2$, and based upon the neutron diffraction data, is ascribed to adsorption of $H_2$ at the open $Cr^{2+}$ site (site II). Note that the reorganization of the neutron density following elongation of the Cr-Cr bond as observed in the neutron powder diffraction experiments suggests that the interaction between $H_2$ and $Cr^{2+}$ is not necessarily weaker than the adsorption enthalpy for $H_2$ at site I. The change in interaction energy is expected to induce a shift in the position of the absorption band attributable to site II, owing to the change in the degree of activation of the $H_2$ molecules located at this site. However, the relatively constant position of the adsorption bands for $H_2$ at the $Cr^{2+}$ site reveals that under the conditions of the infrared experiments, such a structural change does not occur, possibly due to the significantly higher temperatures (and consequently small quantity of adsorbed $H_2$) under which the data were collected.

The evolution of a single peak at 4146 $cm^{-1}$ is observed upon further cooling of the sample below 38 K. This new signal is attributed to adsorption of $H_2$ at the center of the octahedral cages (site III), which was observed at high loadings in the powder neutron diffraction experiments. Notably, the occupation of this site induces a shift in the infrared absorption band for $H_2$ located in the apertures of these cages (site I). This is presumably due to a change in the chemical environment for the $H_2$ molecules at site I, owing to the relatively short proximity (ca. 3.4 Å) of site III from this site.

The lowest-temperature infrared data obtained for an $H_2$ dosing of 1.1 $H_2$ per $Cr^{2+}$ center are shown in Figure 5.8. The standard enthalpy of adsorption ($\Delta H^0$) for the primary binding site was extracted by generating an Arrhenius-type plot from the integrated infrared absorbance as a function of temperature (see Figure 5.8, inset). The value of –6.7(5) kJ/mol is consistent with the relatively weak binding of $H_2$ at the primary binding site, and is significantly lower than the

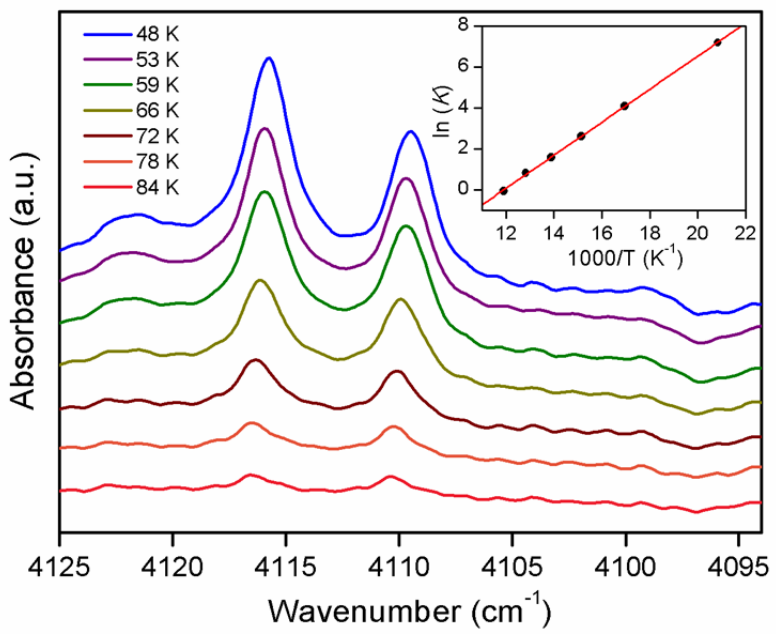


***Figure 5.8.*** Selected variable-temperature infrared spectra of the ortho-para pair for $H_2$ adsorbed at the primary binding site within $Cr_3(BTC)_2$ collected between 48 K and 84 K at a resolution of 1 $cm^{-1}$. Spectra are offset for clarity. Inset: An Arrhenius law plot derived from the integrated absorbance from the spectral data.

corresponding value obtained from a similar analysis for $Cu_3(BTC)_2$ (–10.1 kJ/mol).[12c] However, we note that the primary binding site in $Cu_3(BTC)_2$ is at the open $Cu^{2+}$ cation sites, which leads to a higher site-specific adsorption enthalpy. In addition, the standard enthalpy change $\Delta S^0$ of –78 J/mol·K is consistent with the close approach and efficient packing of the $H_2$ molecules on the framework surface. Note that the enthalpy-entropy correlation for $H_2$ adsorption was recently demonstrated to be a significant factor in assessing the optimal value of $\Delta H^0$ for metal-organic frameworks. The often-quoted optimal $\Delta H^0$ of ca. –15 kJ/mol, is based on a constant $\Delta S^0 = 8R$ = –66.5 J/mol·K, which is smaller in magnitude than the value obtained through variable-temperature infrared spectra for $Cr_3(BTC)_2$, and other porous media. The consideration of this effect leads to the optimal value for $\Delta H^0$ being in the range of –20 to –25 kJ/mol.[5] Note that the value for $\Delta S^0$ is binding site-dependent, which suggests that the more a binding site imposes spatial ordering on the adsorbed $H_2$ molecule, a larger magnitude of $\Delta H^0$ is required to overcome the entropy contribution. Thus, the preparation of a metal-organic framework for ambient $H_2$ storage applications requires careful consideration and fine-tuning of the thermodynamics of each binding site within the material.

## 5.4 Outlook

The foregoing results demonstrate the hydrogen storage properties of $Cr_3(BTC)_2$, a metal-organic framework possessing open $Cr^{2+}$ sites, as probed through a combination of low-pressure adsorption, powder neutron diffraction, inelastic neutron scattering, and variable-temperature infrared experiments. Surprisingly, the loading characteristics differ significantly from those of the isostructural compound $Cu_3(BTC)_2$, with full occupancy at the unsaturated $Cr^{2+}$ center not

being observed until a lengthening of the Cr-Cr distance also occurs at a loading of 1.5 $D_2$ per $Cr^{2+}$ site. Although the low isosteric heat of adsorption in $Cr_3(BTC)_2$ precludes its application as a room temperature hydrogen storage material, such a detailed understanding of the hydrogen sorption properties as probed through several complementary experimental techniques is expected to afford greater insight into the chemical and physical properties that will yield next-generation hydrogen storage materials.

## 5.5 Acknowledgement

The research in Berkeley was funded by the Department of Energy under Contract No. DE-AC02-05CH11231. I thank Fulbright New Zealand for partial financial support. The work at NIST was partially funded by the U.S. Department of Energy within the EERE Hydrogen Sorption Center of Excellence, and the work at Oberlin College was partially funded by the American Chemical Society Petroleum Research Fund. I also thank Dr. Y. Liu for technical assistance during the neutron measurements.

## 5.6 References and Notes

(1) (a) Eddaoudi, M.; Kim, J.; Rosi, N.; Vodak, D.; Wachter, J.; O'Keeffe, M.; Yaghi, O. M. *Science* **2002**, *295*, 469. (b) Matsuda, R.; Kitaura, R.; Kitagawa, S.; Kubota, Y.; Belosludov, R. V.; Kobayashi, T. C.; Sakamoto, H.; Chiba, T.; Takata, M.; Kawazoe, Y.; Mita, Y. *Nature* **2005**, *436*, 238. (c) Millward, A. R.; Yaghi, O. M. *J. Am. Chem. Soc.* **2005**, *127*, 17998. (d) Furukawa, H.; Miller, M. A.; Yaghi, O. M. *J. Mater. Chem.* **2007**, *17*, 3197. (e) Ma, S.; Sun, D.; Simmons, J. M.; Collier, C. D.; Yuan, D.; Zhou, H. C. *J. Am. Chem. Soc.* **2008**, *130*, 1012. (f) Morris, R. E.; Wheatley, P. S. *Angew. Chem. Int. Ed.* **2008**, *47*, 4966. (g) Llewellyn, P. L.; Bourrelly, S.; Serre, C.; Vimont, A.; Daturi, M.; Hamon, L.; De Weireld, G.; Chang, J.-S.; Hong, D.-Y.; Hwang, Y. K.; Jhung, S. H.; Férey, G. *Langmuir* **2008**, *24*, 7245. (h) Furukawa, H.; Ko, N.; Go, Y. B.; Aratani, N.; Choi, S. B.; Choi, E.; Yazaydin, A. Ö; Snurr, R. Q.; O'Keeffe, M.; Kim, J.; Yaghi, O. M. *Science* **2010**, *329*, 424.

(2) EERE: Hydrogen, Fuel Cells, & Infrastructure Technologies Program, http://www.eere.energy.gov/hydrogenandfuelcells, (accessed August 2010).

(3) (a) Rosi, N. L.; Eckert, J.; Eddaoudi, M.; Vodak, D. T.; Kim, J.; O'Keeffe, M.; Yaghi, O. M. *Science* **2003**, *300*, 1127. (b) Férey, G.; Latroche, M.; Serre, C.; Millange, F.; Loiseau T.; Percheron-Guégan, A. *Chem. Commun.* **2003**, 2976. (c) Rowsell, J. L.; Millward, A. R.; Park, K. S.; Yaghi, O. M. *J. Am. Chem. Soc.* **2004**, *126*, 5666. (d) Lee, E. Y.; Suh, M. P. *Angew. Chem., Int. Ed.* **2004**, *43*, 2798. (e) Sun, D.; Ma, S.; Ke, Y.; Collins, D. J.; Zhou, H.-C. *J. Am. Chem. Soc.* **2006**, *128*, 3896. (f) Rowsell, J. L. C.; Yaghi, O. M. *J. Am. Chem. Soc.* **2006**, *128*, 1304. (g) Wong-Foy, A. G.; Matzger, A. J.; Yaghi, O. M. *J. Am. Chem. Soc.* **2006**, *128*, 3494. (h) Lin, X.; Jia, J.; Zhao, X.; Thomas, K. M.; Blake, A. J.; Walker, G. S.; Champness, N. R.; Hubberstey, P.; Schröder, M. *Angew. Chem., Int. Ed.* **2006**, *45*, 7358. (i) Latroche, M.; Surblé, S.; Serre, C.; Mellot-Draznieks, C.; Llewellyn, P. L.; Lee, J.-H.; Chang, J.-S.; Jhung, S. H.; Férey, G. *Angew. Chem., Int. Ed.* **2006**, *45*, 8227. (j) Xiao, B.; Wheatley, P. S.; Zhao, X.; Fletcher, A. J.; Fox, S.; Rossi, A. G.; Megson, I. L.; Bordiga, S.; Regli, L.; Thomas, K. M.; Morris, R. E. *J. Am. Chem. Soc.* **2007**, *129*, 1203. (k) Furukawa,

H.; Miller, M. A.; Yaghi, O. M. *J. Mater. Chem.* **2007**, *17*, 3197. (l) Kaye, S. S.; Dailly, A.; Yaghi, O. M.; Long, J. R. *J. Am. Chem. Soc.* **2007**, *129*, 14176. (m) Sumida, K.; Hill, M. R.; Horike, S.; Dailly, A.; Long, J. R. *J. Am. Chem. Soc.* **2009**, *131*, 15120. (n) Murray, L. J.; Dincă, M.; Long. J. R. *Chem. Soc. Rev.* **2009**, *38*, 1294, and references therein.

(4) Bhatia, S. K.; Myers, A. L. *Langmuir* **2006**, *22*, 1688.

(5) (a) Garrone, E.; Bonelli, B.; Otero Areán, C. *Chem. Phys. Lett.* **2008**, *456*, 68. (b) Otero Areán, C.; Chavan, S.; Cabello, C. P.; Garrone, E.; Palomino, G. T. *ChemPhysChem* **2010**, *11*, 3237.

(6) (a) Dietzel, P. D. C.; Morita, Y.; Blom, R.; Fjellvag, H. *Angew. Chem., Int. Ed.* **2005**, *44*, 6354. (b) Dincă, M.; Long, J. R. *J. Am. Chem. Soc.* **2005**, *127*, 9376. (c) Rosi, N. L.; Kim, J.; Eddaoudi, M.; Chen, B.; O'Keeffe, M.; Yaghi, O. M. *J. Am. Chem. Soc.* **2005**, *127*, 1504. (d) Vimont, A.; Goupil, J.-M.; Lavalley, J.-C.; Daturi, M.; Surblé, S.; Serre, C.; Millange, F.; Férey, G.; Audebrand, N. *J. Am. Chem. Soc.* **2006**, *128*, 3218. (e) Moon, H. R.; Kobayashi, N.; Suh, M. P. *Inorg. Chem.* **2006**, *45*, 8672. (f) Dincă, M; Dailly, A.; Liu, Y.; Brown, C. M.; Neumann, D. A.; Long, J. R. *J. Am. Chem. Soc.* **2006**, *128*, 16876. (g) Dietzel, P. D. C.; Panella, B.; Hirscher, M.; Blom, R.; Fjellvag, H. *Chem. Commun.* **2006**, 959. (h) Dincă, M.; Han, W. S.; Liu, Y.; Dailly, A.; Brown, C. M.; Long, J. R. *Angew. Chem., Int. Ed.* **2007**, *46*, 1419. (i) Dincă, M.; Long, J. R. *Angew. Chem., Int. Ed.* **2008**, *47*, 6766. (j) Caskey, S. R.; Wong-Foy, A. G.; Matzger, A. J. *J. Am. Chem. Soc.* **2008**, *130*, 10870. (k) Dietzel, P. D. C.; Blom, R.; Fjellvag, H. *Eur. J. Inorg. Chem.* **2008**, 3624. (l) Liu, Y.; Kabbour, H.; Brown, C. M.; Neumann, D. A.; Ahn, C. C. *Langmuir* **2008**, *24*, 4772. (m) Dietzel, P. D. C.; Johnsen, R. E.; Fjellvag, H.; Bordiga, S.; Groppo, E.; Chavan, S.; Blom, R. *Chem. Commun.* **2008**, 5125. (n) Dietzel, P. D. C.; Besikiotis, V.; Blom, R. *J. Mater. Chem.* **2009**, *19*, 7362. (o) Zhou, W.; Wu, H.; Yildirim, T. *J. Am. Chem. Soc.* **2008**, *130*, 15268. (p) Sumida, K.; Horike, S.; Kaye, S. S.; Herm, Z. R.; Queen, W. L.; Brown, C. M.; Grandjean, F.; Long, G. J.; Dailly, A.; Long, J. R. *Chem. Sci.* **2010**, *1*, 184.

(7) Belof, J. L.; Stern, A. C.; Eddaoudi, M.; Space, B. *J. Am. Chem. Soc.* **2007**, 15202.

(8) Cheon, Y. E.; Suh, M. P. *Chem. Commun.* **2009**, 2296.

(9) Vitillo, J. G.; Regli, L.; Chavan, S.; Ricchiardi, G.; Spoto, G.; Dietzel, P. D. C.; Bordiga, S.; Zecchina, A. *J. Am. Chem. Soc.* **2008**, *130*, 8386.

(10) (a) Frost, H.; Düren, T.; Snurr, R. Q. *J. Phys. Chem. B* **2006**, *110*, 9565. (b) Han, S. S.; Deng, W.-Q.; Goddard, W. A. *Angew. Chem., Int. Ed.* **2007**, *46*, 6289. (c) Han, S. S.; Goddard, W. A. *J. Am. Chem. Soc.* **2007**, *129*, 8422. (d) Thornton, A. W.; Nairn, K. M.; Hill, J. M.; Hill, A. J.; Hill, M. R. *J. Am. Chem. Soc.* **2009**, *131*, 10662. (e) Han, S. S.; Furukawa, H.; Yaghi, O. M.; Goddard, W. A. *J. Am. Chem. Soc.* **2009**, *131*, 11580. (f) Düren, T.; Bae, Y.-S.; Snurr, R. Q. *Chem. Soc. Rev.* **2009**, *38*, 1237, and references therein.

(11) Murray, L. J.; Dincă, M.; Yano, J.; Chavan, S.; Bordiga, S.; Brown, C. M.; Long, J. R. *J. Am. Chem. Soc.* **2010**, *132*, 7856.

(12) (a) Chui, S. S.-Y.; Lo, S. M.-F.; Charmant, J. P. H.; Orpen, A. G.; Williams, I. D. *Science* **1999**, *283*, 1148. (b) Vishnyakov, A.; Ravikovitch, P. I.; Neimark, A. V.; Bülow, M.; Wang, Q. M. *Nano Lett.* **2003**, *3*, 713. (c) Bordiga, S.; Regli, L.; Bonino, F.; Groppo, E.; Lamberti, C.; Xiao, B.; Wheatley, P. S.; Morris, R. E.; Zecchina, A. *Phys. Chem. Chem. Phys.* **2007**, *9*, 2676.

(13) B. H. Toby, *J. Appl. Cryst*. 2001, **34**, 210.

(14) Larson, A. C.; Von Dreele, R. B. *General Structure Analysis System (GSAS)*, Los Alamos National Laboratory Report LAUR 86-748, 2000.
(15) Brown, C. M.; Liu, Y.; Yildirim, T.; Peterson, V. K.; Kepert, C. J. *Nanotechnology* **2009**, *20*, 204025.
(16) Udovic, T. J.; Brown, C. M.; Leao, J. B; Brand, P. C.; Jiggetts, R. D.; Zeitoun, R.; Pierce, T. A.; Peral, I.; Copley, J. R. D.; Huang, Q.; Neumann, D. A.; Fields, R. J. *Nuclear Inst. and Methods in Physics Research, A*, **2008**, *588*, 406.
(17) Azuah, R. T.; Kneller, L. R.; Qiu, Y.; Tregenna-Piggott, P. L. W.; Brown, C. M.; Copley, J. R. D.; Dimeo, R. M. *J. Res. Natl. Inst. Stan. Technol.*, **2009**, *114*, 241.
(18) FitzGerald, S. A.; Churchill, H. O. H.; Korngut, P. M.; Simmons, C. B.; Strangas, Y. E. *Rev. Sci. Instrum.* **2006**, *77*, 093110.
(19) Rowsell, J. L. C.; Yaghi, O. M. *J. Am. Chem. Soc.* **2006**, *128*, 1304.
(20) Peterson, V. K.; Liu, Y.; Brown, C. M.; Kepert, C. J. *J. Am. Chem. Soc.* **2006**, *128*, 15578.
(21) The shortest M2+-D2 distance directly observed to date within a metal-organic framework *via* neutron diffraction is 2.15(4) Å observed within Fe3[(Fe4Cl)3(BTT)8] (Fe-BTT, BTT3- = 1,3,5-benzenetristetrazolate), which features unsaturated Fe2+ coordination sites; see Ref. 6p.
(22) Ramirez-Cuesta, A. J.; Mitchell, P. C. H.; Ross, D. K.; Georgiev, P. A.; Anderson, P. A.; Langmi, H. W.; Book, D. *J. Mater. Chem.* **2007**, *17*, 2533.
(23) Note that the correlation between the neutron scattering data and infrared data is not definitive owing to the difference in the conditions (temperature and loading level) employed for the two types of experiments. While the analysis presented here allows the greatest degree of consistency and agreement between the two types of data, we envisage a number of alternative scenarios for peak assignment (particularly for site I and II), if the infrared data alone is considered.

# Chapter 6: Development of a High-Throughput Methodology for the Discovery of Robust Metal-Organic Frameworks for Carbon Dioxide Capture

## 6.1 Introduction

As mentioned in Chapter 1.3, one of the most important challenges that must be addressed if metal-organic frameworks are to be deployed within real-world post-combustion $CO_2$ capture systems is the discovery of materials exhibiting enhanced stability toward $H_2O$ and other minor components of the flue gas, such as ($O_2$, CO, $NO_x$ and $SO_x$). Many materials based upon divalent transition metal ions, such as $Cu^{2+}$ and $Zn^{2+}$, feature relatively weak coordination bonding between the metal nodes and the organic ligands (typically carboxylates), and are unstable towards air and moisture following activated. Indeed, air exposure of such a material often leads to a loss of crystallinity, indicating a loss in the integrity of the period structure, and a degradation of the gas adsorption capacity. As a result, the performance of the $CO_2$ capture system would be rapidly diminished, leading to the need to frequently replace the material within the adsorbent bed, which has significant implications on the cost of the system.

One possible strategy through which more robust materials may be generated is through the use of high-valent metal cations (e.g. $Al^{3+}$, $Ti^{4+}$, and $Zr^{4+}$)[1] or more strongly binding organic ligands (e.g. pyrazolates and triazolates).[2] Indeed, a number of materials exhibiting impressive chemical and thermal stability profiles based on these components have appeared recently. For example, the compound $Ni_3(BTP)_2$ ($BTP^{2-}$ = 1,4-benzenedipyrazolate) is stable to heating in air up to 450 ºC, and can also be treated with $H_2O$ and refluxed in a variety of aqueous solutions of acids and bases (in a pH range of 2-14) for 14 days without loss of porosity.[3] Meanwhile, the $Zr_6O_4(OH)_4(BDC)_6$ (UiO-66; $BDC^{2-}$ = 1,4-benzenedicarboxylate) material and its isoreticular analogs feature a high thermal robustness and an impressive stability toward relatively high concentrations of aqueous HCl (pH = 1) and NaOH (pH = 14).[4] Thus, the construction of new materials derived from these types of components featuring a high selectivity for $CO_2$ over $N_2$ is expected to facilitate a high long-term capture performance.

As demonstrated in Chapter 3, a high-throughput methodology is a suitable strategy for the accelerated discovery of robust materials for $CO_2$ capture. However, the adsorption screening of the new compounds utilizing a conventional adsorption instrument is currently a rate-limiting step in the workflow. As such, a parallel adsorption instrument that facilitates the collection of the $CO_2$ adsorption data for multiple samples in a single experiment would allow the most promising materials for post-combustion $CO_2$ capture to be rapidly identified. Herein, the development of a custom-built adsorption apparatus constructed in collaboration with Wildcat Discovery Technologies (San Diego, CA) designed to simultaneously collect single-component gas adsorption isotherms for 28 different samples. In addition, a complete methodology has also been developed to allow the seamless integration of all of the high-throughput elements of the workflow (synthesis, powder X-ray diffraction, and adsorption). We describe the new methodology in the context of metal-insertion reactions within the robust framework Al(OH)(bpydc),[5] which features one-dimensional pores lined with chelating 2,2'-bipyridine sites open for metal coordination (Figure 6.1). In addition to the high thermal and chemical stability of the parent material, high-throughput adsorption screening has allowed the identification of a number of metal salts affording enhanced $CO_2$ adsorption properties. In all, the adsorption isotherms for metal-loaded samples of over 100 different compositions were obtained in less

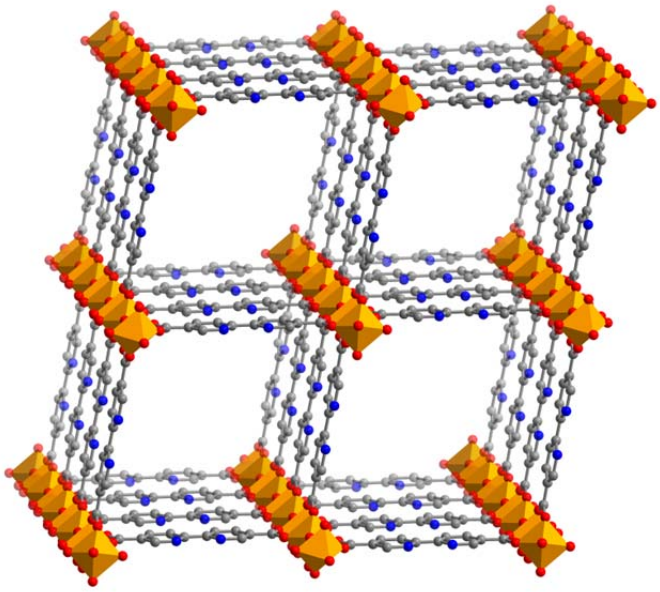

***Figure 6.1*** A portion of the periodic structure of evacuated Al(OH)(bpydc) (MOF-253; $bpydc^{2-}$ = 2,2'-bipyridine-5,5'-dicarboxylate). Yellow octahedra represent $AlO_6$ units, while gray, blue and red spheres represent C, N, and O atoms, respectively. H atoms omitted for clarity.

than 5 days of instrument time, which represents a tremendous increase in throughput compared to conventional adsorption experiments.

## 6.2 Experimental Section

All reagents were purchased from commercial vendors and used without further purification. 2,2'-bipyridine-5,5'-dicarboxylic acid ($H_2$bpydc),[6] $Zn(MeIM)_2$ (ZIF-8; $MeIM^-$ = 2-methylimidazolate)[7] and $Mg_2$(dobdc) (MOF-74(Mg), CPO-27-Mg; $dobdc^{4-}$ = 2,5-dioxido-1,4-benzenedicarboxylate)[8] were synthesized according to the literature procedures.

**Al(OH)(bpydc) (MOF-253).** The literature procedure was adapted. The $H_2$bpydc (5.63 g, 23.1 mmol) ligand was added to a solution of $AlCl_3 \cdot 6H_2O$ (5.63 g, 23.3 mmol) dissolved in DMF (750 mL) charged to a 1 L reaction flask. The vessel was sealed and heated under static conditions at 120 ºC for 3 days, after which a white solid was obtained. This solid was filtered off and washed with DMF (3 × 50 mL), and dried overnight in the air. The dried solid was then transferred to a 1 L bottle, to which anhydrous DMF (500 mL was added). The vessel was tightly capped with a Teflon-lined lid and placed in an oven set to 120 ºC for 24 h. The DMF was then decanted, and the washing procedure was repeated a further three times. The analogous procedure was then performed using anhydrous MeOH, and following the final washing step, the resulting white solid was evacuated overnight on a Schlenk line. Final activation was performed by heating the material to 250 ºC *in vacuo* until the outgas rate was less than 2 mTorr/min. The phase purity of the material was confirmed using a combination of powder X-ray diffraction, thermogravimetric analysis, and comparison of the Langmuir surface area to the literature data.[5] Yield: 5.72 g (86%).

**High-Throughput Synthesis of Metal-Loaded Variants of Al(OH)(bpydc).** In a typical experiment, a 6 × 4 array of 4 mL glass vials was placed on the robot deck, the deck elements of which were described in Chapter 3, and the mass of the empty vials was obtained using an automated routine that transfers each vial to the built-in balance for weighing. During the procedure, each vial was weighed 5 times to obtain an accurate mass, though in all experiments, the standard deviation of the vial mass was below 0.2 mg. The metal salts and the activated form of the bare Al(OH)(bpydc) framework were then loaded into individual powder hoppers used for automated solid dispensing, and placed on the robot deck. The activated framework (50 mg, 17.3 μmol) was firstly dispensed into each of the vials, then the vials were re-weighed using the same routine as for the empty vials in order to obtain a precise mass of the parent framework. Six different metal salts were then dispensed in four different stoichiometries (0.25, 0.50, 0.75, 1.0 equivalents) according to a predetermined composition library, and each vial was then charged with 3 mL of MeCN. The vials were manually capped with Teflon-lined caps, and the reaction mixtures were heated at 90 ºC for 5 days, replacing the MeCN with fresh solvent every 12 h.

**Sample Activation.** The excess solvent from the metal loading reactions was manually decanted, and the 24 samples were transferred to two custom-built assemblies allowing the parallel evacuation of up to 14 samples per assembly. The assemblies were sealed in the glove box, and connected to a Schlenk line equipped with a rotary vacuum pump, and heated *in vacuo* at 80 ºC for 24 h. After this time, the valve opened to the vacuum line was closed off, and the assemblies were transferred to a solvent-free glove box for loading of the samples into the Wildcat assemblies used for parallel gas adsorption measurements.

**High-Throughput Gas Adsorption Measurements.** In a solvent-free glove box, the vials containing the activated samples were weighed to obtain a final sample mass, and these were then transferred into the wells of four 7-well assemblies of the type used for gas adsorption experiments on the first-generation Wildcat adsorption apparatus. The assemblies were attached to the instrument, and the headspace of each manifold was evacuated for at least 5 h prior to opening of the Schrader valves sealing each of the sample wells. These valves were then opened, and the samples evacuated for a further 1 h. The sample wells were then dosed with known amounts of high-purity He gas to obtain a free space volume, which was used in the calculation of the quantity of gas adsorbed in the subsequent adsorption experiments.

## 6.3 Results and Discussion

In this section, the configuration of the high-throughput adsorption instrument is described, followed by a discussion regarding its integration into a high-throughput workflow for the adsorption screening of metal-loaded variants of Al(OH)(bpydc), which serves as an exemplary case for demonstrating the successful implementation of the methodology.

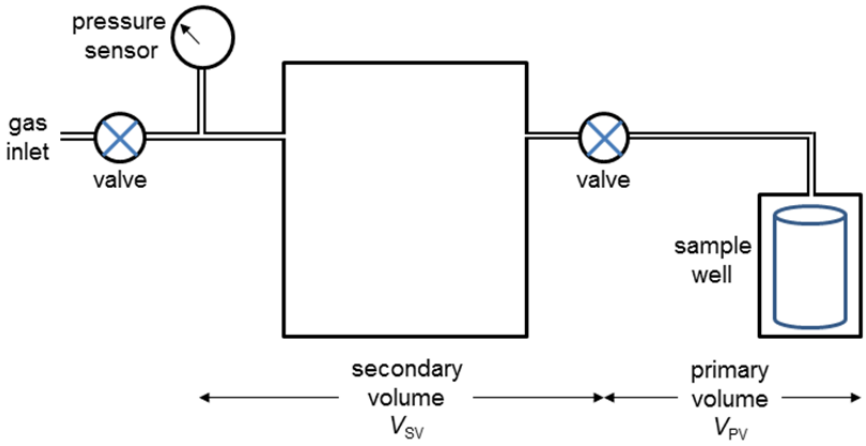


***Figure 6.2.*** A schematic showing a single channel in the high-throughput adsorption instrument. The gases are firstly dosed into the secondary volume ($V_{SV}$), which is a known volume, and expanded into the primary volume ($V_{SV}$) that houses the sample.

**Configuration of the High-Throughput Instrument.** The custom-built high-throughput adsorption instrument designed by Wildcat Discovery Technologies (San Diego, CA) is equipped with 28 separate manifolds that can independently analyze the adsorption of pure gases at ambient temperatures and above. A schematic of a single manifold is displayed in Figure 6.2. Here, the secondary volume ($V_{SV}$) is a known volume determined during the installation of the instrument, allowing the total quantity of gas dosed into the manifold at any time to be precisely known. The primary volume ($V_{PV}$), which contains the adsorbing material, is determined prior to the adsorption experiment by the expansion of a known quantity of a non-adsorbing gas (e.g. He) from the secondary volume into the primary volume, and is computed as follows:

$$V_{PV} = V_{SV}\left(\frac{P_i}{P_f} - 1\right) \qquad (6.1)$$

where $P_i$ and $P_f$ represent the initial and final pressures within the manifold, respectively.

Following determination of the quantity $V_{PV}$, the adsorption experiment of the gas of interest can be performed. In the case of the adsorbing gas, a certain fraction of the dosed gas is accommodated within the framework, which leads to the observed pressure becoming lower than that calculated for the simple expansion of the gas into the primary volume. The quantity adsorbed can hence be computed based on the difference between the pressure expected based on the expected pressure for a given quantity of dosed gas, and the actual observed pressure *via* the following expression:

$$n_{ads} = n_{dose} - \frac{P_{eq}(V_{PV}+V_{SV})}{RT} \qquad (6.2)$$

where $n_{ads}$ and $n_{dose}$ represent the quantity of gas adsorbed within the framework, and the total quantity of gas dosed into the manifold, respectively, and $P_{eq}$ is the final pressure following equilibriation of the system.

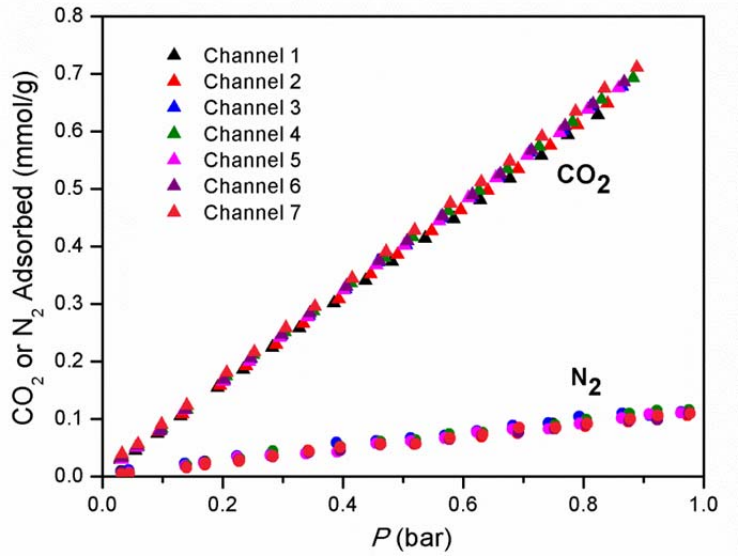


***Figure 6.3.*** $CO_2$ and $N_2$ adsorption isotherms recorded at 298 K for samples from a single batch of ZIF-8 as measured in 7 different channels the high-throughput adsorption instrument. Although just 7 sets of isotherm data are shown here for clarity, the agreement between the adsorption quantities was similar across all 28 channels.

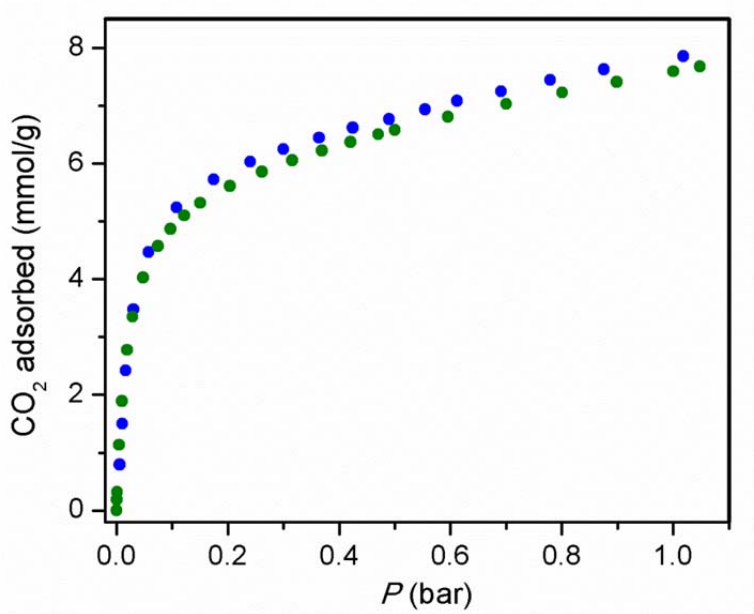


***Figure 6.4.*** $CO_2$ adsorption isotherms recorded at 298 K for $Mg_2(dobdc)$ ($dobdc^{4-}$ = 2,5-dioxido-1,4-benzenedicarboxylate) as measured in a conventional adsorption device (green) and the high-throughput adsorption device (blue). Only a single channel of adsorption data is shown for clarity.

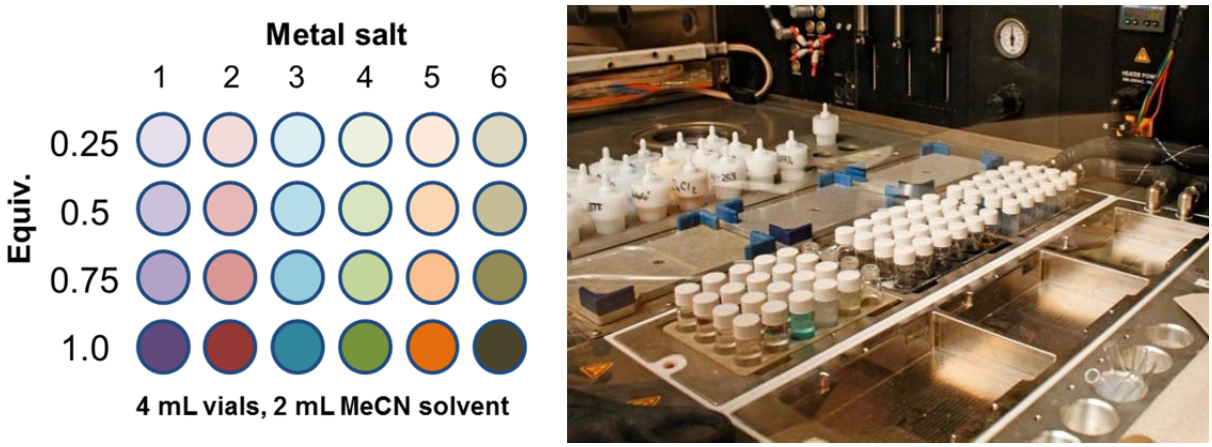


***Figure 6.5.*** (a) A schematic showing the composition of a sample high-throughput library, in which 6 different metal salts and 4 different loading levels can be readily screened in a single batch; and (b) a view of the robot deck, in which samples for three libraries are being simultaneously heated.

**Validation of First-Generation Wildcat Adsorption Instrument.** Following the installation of the instrument, validation of the operation of each of the 28 channels was performed by placing a known quantity of a microporous framework into each of the wells, followed by the collection of a full $CO_2$ and $N_2$ adsorption isotherm at 298 K. As demonstrated by the isotherms collected for ZIF-8 displayed in Figure 6.3, the quantity of $CO_2$ or $N_2$ adsorbed is consistent between the channels, and the magnitude of the uptake is also comparable to those reported previously in the literature. The high agreement between the uptakes of the individual channels also demonstrates the successful calculation of the secondary volumes of each of the channels.

In addition, the accuracy of the magnitude of the quantity adsorbed was further confirmed by collecting the $CO_2$ adsorption isotherms for a variety of materials exhibiting high uptakes, including $Mg_2$(dobdc). Furthermore, owing to the high density of exposed $Mg^{2+}$ sites decorating the pore surface of this material and their sensitivity to exposure to air and moisture, this compound serves as an ideal test case to verify the integrity of the sample assemblies and the elimination of all leaks from the system. In this experiment, the data collected on the high-throughput adsorption device was compared to the corresponding adsorption isotherms obtained on a conventional adsorption instrument. As shown in Figure 6.4, the excellent agreement between the two types of data provides confirmation that the instrument has been correctly calibrated and is able to be used as a reliable method for screening unknown samples stemming from the high-throughput synthesis instrument.

**Preparation and Adsorption Screening of Metal-Loaded Variants of Al(OH)(bpydc).** The activated form of Al(OH)(bpydc) was loaded with a variety of main group and first-row transition metal salts at loading levels of 0.25, 0.50, 0.75, and 1.0 metal ions per bipyridine binding site. In each high-throughput experiment, a total of 6 metal salts and 4 loading levels were utilized to give a total of 24 samples (see Figure 6.5) per library. The salts tested included fluoride, chloride, bromide, nitrate, tetrafluoroborate, and trifluorosulfonate salts of Mg, Ca, V, Cr, Mn, Fe, Co, Ni, Cu, and Zn, though not all salts could be fully incorporated into the pores of the framework due to the insolubility of the salt in MeCN (which was previously shown

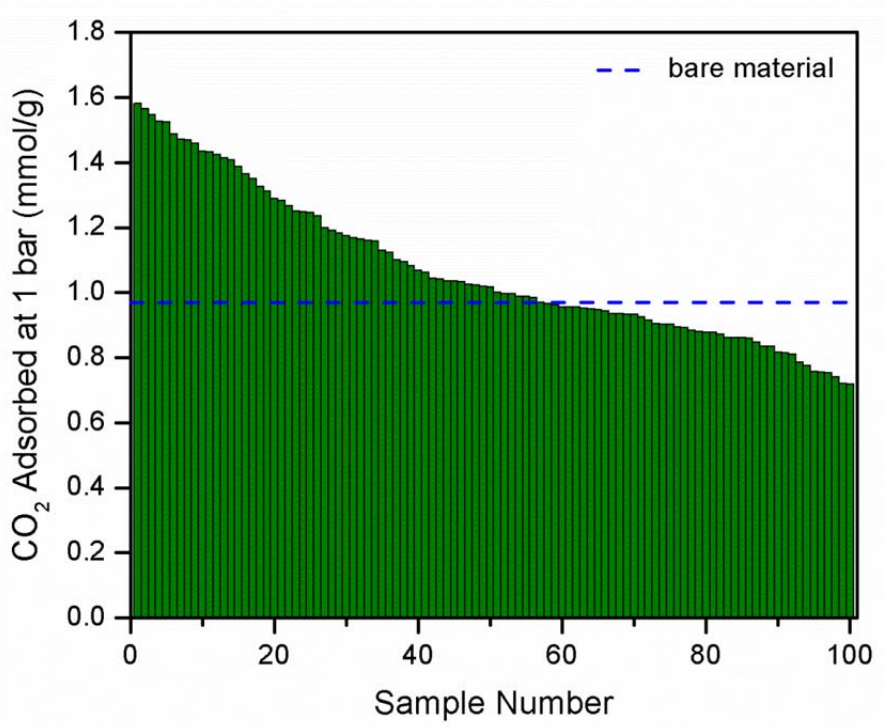


***Figure 6.6.*** A histogram showing the $CO_2$ uptake at 313 K and 1.0 bar for the samples surveyed in the high-throughput adsorption screening experiments. The highest adsorption values were recorded for $NiCl_2$ and $Co(BF_4)_2$-loaded samples, which feature a gravimetric adsorption capacity that is enhanced by over 60% compared to bare Al(OH)(bpydc) ($bpydc^{2-}$ = 2,2'-bipyridine-5,5'-dicarboxylate).

to be an ideal medium for metal insertion reactions involving the Al(OH)(bpydc) framework[5]), or the low affinity of the metal salt toward the bipyridine binding site.

Following the metal insertion reaction, the excess MeCN solvent was decanted from the samples, and the samples were transferred into a degas assembly and activated *in vacuo*. Once removal of the solvent within the pores was achieved (confirmed by the pressure of the vacuum line returning to the baseline level), the solids were transferred to the high-throughput adsorption instrument. For all samples, a full $CO_2$ adsorption isotherm was collected up to 1.2 bar at 313 K, and the uptakes of the fully-loaded samples (1.0 metal ions per bipyridine site) at 1.0 bar are depicted in a histogram form in Figure 6.6. Remarkably, depending on the identity of the salt, the adsorption capacity is considerably affected. Indeed, while some of the materials exhibited diminished adsorption capacities compared to the bare form of the framework, approximately half of the samples demonstrated a higher $CO_2$ adsorption at 1.0 bar. Closer inspection of the identity of the materials exhibiting the highest $CO_2$ adsorption capacities showed a strong trend towards the later transition metals, especially $Co^{2+}$, $Ni^{2+}$, and $Cu^{2+}$. Although the nature of the interaction between the adsorbed $CO_2$ and the metal ions has yet to be established, a likely origin is the smaller ionic radius of these metals compared to the earlier first-row transition metals resulting in a greater induced dipole, and a greater affinity, toward the $CO_2$. Note that the counteranion was also considerably influenced the uptake, wherein lighter anions, such as $Cl^-$, $BF_4^-$, $NO_3^-$ facilitated higher uptakes than their heavier counterparts. This is presumably due to

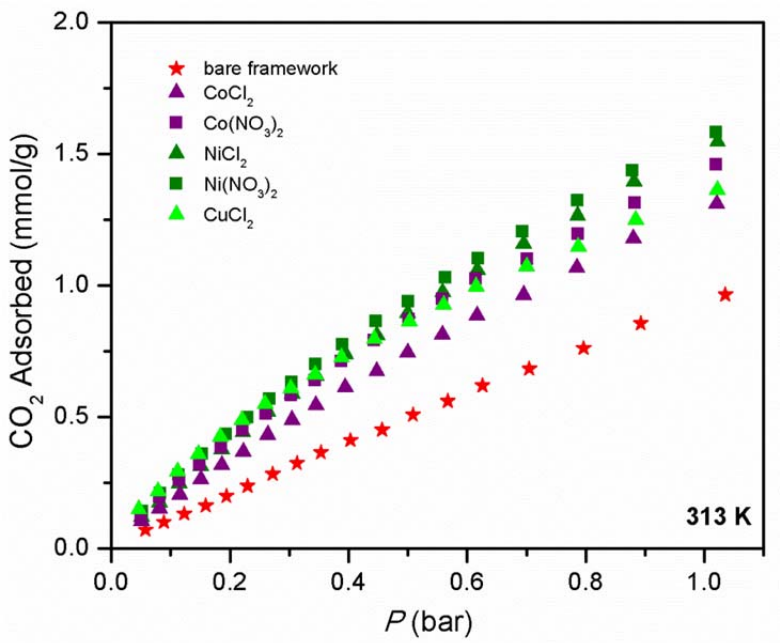


***Figure 6.7.*** $CO_2$ adsorption isotherms for selected metal-loaded samples of Al(OH)(bpydc) (MOF-253; $bpydc^{2-}$ = 2,2'-bipyridine-5,5'-dicarboxylate) collected at 313 K.

the fact that lighter anions contribute less mass to the overall system, resulting in a higher $CO_2$ uptake on a gravimetric basis.

Moreover, in addition to the $Cu(BF_4)_2$-loaded material, which was previously shown to have a dramatically higher uptake compared to the parent material,[5] the $CoCl_2$-, $Co(NO_3)_2$-, $NiCl_2$-, $Ni(NO_3)_2$-, and $CuCl_2$-loaded materials also exhibited enhanced adsorption capacities compared to the bare framework, as shown in Figure 6.7. Indeed, in the case of a sample loaded with a full equivalent of $NiCl_2$, the $CO_2$ adsorption capacity is enhanced by approximately 65% at 1.0 bar. Note that, for all of the samples displayed here, the maximum adsorption capacity was always obtained at a loading level of 1.0 $M^{2+}$ per bipyridine. Excess loadings were also tested for these metal salts, but the uptakes were largely unaffected due to the excess metal being removed during the washing procedure.

## 6.4 Outlook

The foregoing results have described the development of a new high-throughput methodology that can be used for the adsorption screening of new materials for $CO_2$ capture. The new methodology has been employed in the context of rapidly screening the products stemming from metal-loading reactions within the robust framework Al(OH)(bpydc), showing that an enhanced uptake can be observed for a variety of metal salts. The same methodology is now being deployed in the screening of new products stemming from the high-throughput synthesis reactions employing high-valent metal ions and strongly binding ligands. Future work will also focus on long-term cycling of the most promising materials, as well as full elucidation of the stability profile under humidified conditions.

## 6.5 Acknowledgments

This research was funded by the Advanced Research Projects Agency - Energy (ARPA-E), U.S. Department of Energy. I thank Fulbright New Zealand for partial financial support, and Dr. T.-H. Bae, Mr. J. A. Mason and Mr. E. D. Bloch for experimental assistance, as well as Dr. S. S. Kaye, Mr. K. Micklash and Mr. J. Dutton at Wildcat Discovery Technologies for assistance in the installation and the validation of the high-throughput adsorption instrument.

## 6.6 References and Notes

(1) (a) Férey, G.; Serre, C.; Mellot-Draznieks, C.; Millange, F.; Surblé, S.; Dutour, J.; Margiolaki, I. Angew. Chem., Int. Ed. 2004, 43, 6296. (b) Férey, G.; Mellot-Draznieks, C.; Serre, C.; Millange, F.; Dutour, J.; Surblé, S.; Margiolaki, I. Science 2005, 309, 2040. (c) Volkringer, C.; Popov, D.; Loiseau, T.; Guillou, N.; Férey, G.; Haouas, M.; Taulelle, F.; Mellot-Draznieks, C.; Burghammer, M.; Riekel, C. Nat. Mater. 2007, 6, 760. (d) Küsgens, P.; Rose, M.; Senkovska, I.; Fröde, H.; Henshcel, A.; Siegle, S.; Kaskel, S. Microporous Mesoporous Mater. 2009, 120, 325. (e) Low, J. J.; Benin, A. I.; Jakubczak, P.; Abrahamian, J. F.; Faheem, S. A.; Willis, R. R. J. Am. Chem. Soc. 2009, 131, 15834. (f) Ehrenmann, J.; Henninger, S. K.; Janiak, C. Eur. J. Inorg. Chem. 2011, 471.

(2) (a) Choi, H. J.; Dincă, M.; Long, J. R. *J. Am. Chem. Soc.* **2008**, *130*, 7848. (b) Demessence, A.; D'Alessandro, D. M.; Foo, M. L.; Long, J. R., *J. Am. Chem. Soc.* **2009**, *131*, 8784. (c) Maspero, A.; Galli, S.; Colombo, V.; Peli, G.; Masciocchi, N.; Stagni, S.; Barea, E.; Navarro, J. A. R. *Inorg. Chim. Acta* **2009**, *362*, 4340. (d) McDonald, T. M.; D'Alessandro, D. M.; Krishna, R.; Long, J. R. *Chem. Sci.* **2011**, *2*, 2022-2028.

(3) Colombo, V.; Galli, S.; Choi, H. J.; Han, G. D.; Maspero, A.; Palmisano, G.; Masciocchi, N.; Long, J. R. *Chem. Sci.* **2011**, *2*, 1311.

(4) Kandiah, M.; Nilsen, M. H.; Usseglio, S.; Jakobsen, S.; Olsbye, U.; Tilset, M.; Larabi, C.; Quadrelli, E. A.; Bonino, F.; Lillerud, K. P. *Chem. Mater.* **2010**, *22*, 6632.

(5) Bloch, E. D.; Britt, D.; Doonan, C. J.; Uribe-Romo, F. J.; Furukawa, H.; Long, J. R.; Yaghi, O. M. *J. Am. Chem. Soc.* **2010**, *132*, 14382.

(6) Venema, F.; Nelissen, H. F. M.; Berthault, P.; Birlirakis, N.; Rowan, A. E.; Feiters, M. C.; Nolte, R. J. M. *Chem. Eur. J.* **1998**, *4*, 2237.

(7) Park, K. S.; Ni, Z.; Côte, A. P.; Choi, J. Y.; Huang, R.; Uribe-Romo, F. J.; Chae, H. K.; O'Keeffe, M.; Yaghi, O. M. *Proc. Nat. Acad. Sci. U.S.A.* **2006**, *103*, 10186.

(8) Caskey, S. R.; Wong-Foy, A. G.; Matzger, A. J. *J. Am. Chem. Soc.* **2008**, *130*, 10870.

# Chapter 7: Opposing Surface Area Distribution (OSAD) as a Characterization Tool for Metal-Organic Frameworks

## 7.1 Introduction

The preparation and characterization of microporous metal-organic frameworks for use in applications such as gas storage, molecular separations, and catalysis, is an area that has experienced rapid progress in recent years.[1,2] The ability to create new materials with physical and chemical properties that are well-matched to an intended application is in part a result of the modular synthetic approach, in which the geometry and functionalities of the building blocks are preserved when assembled into the extended coordination network. This strategy allows the structural features of the framework, including the pore size, shape, and surface functionalization, to be tuned in a rational fashion. Significant advances have also been made in expanding the scope of the pore surface chemistry via a rapidly growing number of post-synthetic modification reactions that are available, for example, as a means of further optimizing the adsorption properties of the materials.[3] As such, metal-organic frameworks present a tremendously versatile platform for developing next generation materials for a given application, provided researchers are able to elucidate the structural and chemical features that would afford this enhanced performance.

One of the most crucial structural parameters dictating the adsorptive properties of a microporous material is the separation distance of the opposing surfaces within the structure. For storage applications, this separation must be large enough to facilitate the diffusion of the adsorbing molecules into the solid, but should also be a distance that limits the creation of large voids in which the guest molecules are not influenced by the pore walls. Indeed, while a very large wall separation (and large pore diameter) is of benefit for raising the gravimetric storage density, it is generally not advantageous in boosting the volumetric storage density owing to the larger quantities of gas that would be compressed in a bulk-like fashion. Note that the optimal wall separation is strongly dependent on the specific gas to be stored, and the operation temperature and pressure of the material, due to the fact that pore walls exert less of an influence on the adsorbed molecules at higher temperatures and lower pressures. For example, in the area of physisorptive $H_2$ storage, a pore wall separation of ca. 10 Å, which represents a monolayer of $H_2$ molecules on each of the opposing surfaces and an additional monolayer adsorbed in between these layers, is desired for a sorbent operating at 77 K.[4] However, a significantly smaller separation of ca. 7 Å, which represents just a single monolayer on each wall is required for maximizing the storage density at 298 K.

The fine-tuning of the wall separation distance within metal-organic frameworks can also play an important role in enhancing the selectivity of a material towards certain molecules in separation applications. Here, we distinguish between *adsorption-based selectivity*, which is a thermodynamic phenomenon that arises as a result of one of the components of the gas mixture having a higher affinity towards the surface of the material over the other, and *kinetic-based selectivity*, where the separation is achieved based on size exclusion or the more rapid diffusion of one of the gas molecules through the pores of the framework. Although kinetics-based separations are employed in membrane technologies and represent an important means for separating gas mixtures, here, we consider the opposing wall distance as a means of tuning the thermodynamics of adsorption to induce adsorption-based selectivity. For example, in the area of Xe/Kr separations, a recent computational study suggests that materials featuring pore

dimensions that are a good match with the diameter of a Xe atom facilitate the highest adsorptive selectivity over Kr. This is due to the stronger overall interactions of Xe with the pore walls compared to Kr, which has a significantly smaller atomic radius (Kr: 1.03 Å; Xe: 1.24 Å).[5] Thus the identification of the optimal opposing wall distance for a given separation, and the subsequent preparation of new materials with a maximized density of surfaces that have an opposing wall at this distance, is expected to lead to greatly enhanced performance compared to existing adsorbents.

The crystalline nature of metal-organic frameworks presents an opportunity for rationally selecting microporous adsorbents for further testing in certain applications based on the pore structures. Although structural parameters like pore size can be estimated using methods such as Ar porosimetry, they require the material to be synthesized, fully activated, and adsorption data to be collected prior to their determination. Note that, since the pore size distribution is generated from a fitting to the adsorption data, it is also not a direct geometric measurement of the distribution of the opposing wall distances within the material. Furthermore, the structural complexity of most metal-organic frameworks precludes the determination of the distribution of opposing wall separation distances by visual inspection (see Figure 7.1). Herein, we report a geometric method that is able to directly survey the distribution of opposing wall distances within a porous metal-organic framework structure given the unit cell and the coordinates of the framework atoms. We first introduce the basic concept of the calculation and demonstrate its utility by analyzing the data stemming from its application to a number of important metal-organic frameworks. Then, the algorithm is deployed in screening a variety of known materials in the context of high-density methane storage, where, based on recent computational work,[6] structures featuring a high density of opposing wall distances at 4 or 8 Å would be of interest for experimental screening. Although the application of the methodology is applied to the study of methane storage materials in this case, it is expected that data of a similar type would be of utility in the preliminary screening stages for identifying candidate materials for experimental study in a wide range of gas storage and molecular separation applications where the desired wall separation is known.

## 7.2 Experimental Section

All reagents were obtained from commercial vendors and used without further purification. All manipulations, unless otherwise noted, were performed in air. The compound $Zr_6O_4(OH)_4(BDC)_6$ ($BDC^{2-}$ = 1,4-benzenedicarboxylate; UiO-66) was synthesized and activated according to the previously reported procedure.[7]

**Opposing Surface Area Distribution (OSAD) Calculations.** The opposing surface area distribution program[8] was developed using the C++ programming language using the Microsoft Visual C++ 2010 Express platform, which was obtained free of charge from the Internet.[9] The structural data for the metal-organic frameworks used in the opposing surface area calculations were obtained from the Cambridge Structural Database (CSD),[10] and in some cases, atoms corresponding to solvent molecules or other disordered fragments within the structures were removed to most closely represent the pristine, fully-activated form of the material. The list of atomic coordinates was generated by converting the crystallographic information file (CIF) for the single-crystal X-ray structure into the XYZ file format. The atomic radii for the framework atoms were calculated using the universal force field (UFF),[11] and each of the OSAD calculations were run using a dinitrogen-sized probe molecule (diameter = 3.68 Å).

**High-Pressure Methane Adsorption Experiments.** Approximately 200 mg of sample was loaded into a sample holder in a glove box under a dinitrogen atmosphere. Methane excess adsorption measurements were performed on an automated Sieverts' apparatus (PCTPro-2000 from Hy-Energy Scientific Instruments, LLC) over a pressure range of 0-100 bar. UHP-grade methane and helium (99.999% purity) were used for all measurements. Volumetric measurements were carried out at a constant temperature of 298 K by submerging the sample holder in a water bath equipped with a temperature controller. The total gravimetric and volumetric adsorption capacities were calculated as described previously.[12]

## 7.3 Results and Discussion

The internal structures of most metal-organic frameworks feature pore apertures and void spaces with widely varying distances to the opposing surface, as shown schematically in Figure 7.1. The algorithm described in this work exhaustively surveys all of the surfaces of the framework by inserting (usually $N_2$-sized) probe molecules along the surface of the material, and measuring the distance to the opposing wall by moving the probe in steps in a direction that is normal to the pore surface. This results in a distribution (histogram) of opposing wall distances that can be readily associated with a surface area by using the Monte Carlo integration process described in detail below, thereby allowing the amount of surface area for an opposing surface disposed at a given distance to be calculated.

**Calculation of the Opposing Surface Area Distribution (OSAD).** The algorithm for calculating the opposing surface area distribution is related to a method recently reported for calculating the accessible surface area within crystalline networks,[13] which has been utilized for the estimation of the maximum BET surface area[14] within microporous metal-organic frameworks. Here, in addition to the insertion of probe spheres at random positions along the surface, the method samples the surface normal vectors of the surface and measures the distance

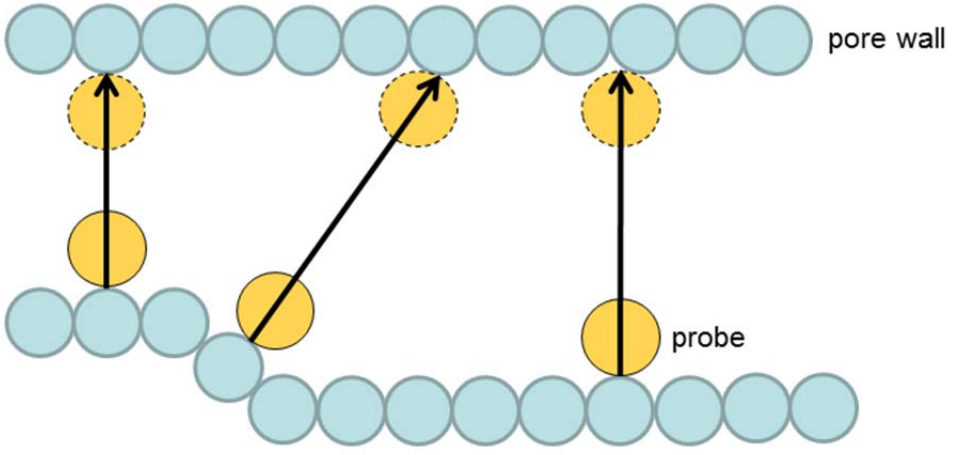


***Figure 7.1.*** A schematic drawing showing the main concept of the opposing surface area calculation. Probe molecules (yellow spheres) are inserted at various points along the surface of the structure, and is moved in the direction of the surface normal until a collision is detected with the opposing wall (at the position of the dotted yellow spheres).

to the nearest surface along the trajectory of the surface normal. along the surface of the structure. The sampling algorithm firstly generates $n$ unit vectors ($n > 5000$) by generating $x$, $y$, and $z$ values between -1 and +1 using a random number generator, followed by normalization of the vector length to 1 to generate a spherical distribution. A set of these unit $n$ vectors is then associated for each atom $a_i$ in the crystal structure, assigning the atom center as the origin of the vector, and setting the length to the value of ($r_{atom} + r_{probe}$), where $r_{atom}$ and $r_{probe}$ represent the radii of the atom (as determined by the UFF force field)[11] and the probe sphere, respectively. The end points of these vectors serve as insertion points for the set of probe molecules $\{P_1, P_2,..., P_n\}$.

Upon insertion of the probe $P_i$, it is first checked whether it is in collision with another atom in the atom list. If a collision is detected, the probe is immediately discarded, and the same procedure is performed for the next probe in the set $P_{i+1}$. If the probe does not intersect with any other atoms, the probe is then moved a small fixed distance ($d_{step}$, typically 0.1 Å) in the direction of the normal vector. Following each increment, a check for collisions with every other atom in the structure is performed, and the probe is stepped in this manner until a collision is eventually detected at an opposing surface within the framework. The distance $d_i$ to the opposing surface is thus readily computed by the expression:

$$d_i = 2\, r_{\mathrm{probe}} + n_{\mathrm{step}} d_{\mathrm{step}} \qquad (7.1)$$

where $n_{step}$ is the number of displacements required to induce a collision of the probe sphere with the opposing surface. Note that the range of $d_i$ takes discrete values ranging from $2r_{probe}$ to ($2r_{probe} + n_{max}d_{step}$) in increments of $d_{step}$, where $n_{max}$ is the maximum number of steps allowed. The value of $n_{max}$ is usually made arbitrarily large (ca. 500, which represents 50 Å for a 0.1 Å step size), and for nearly all structures studied, no probes actually were displaced $n_{max}$ times before encountering a collision. Nevertheless such a parameter was found to be necessary in order to ensure the prevention of infinite looping of the program in the unlikely scenario where a surface normal would lead to a probe with a path that would never lead to a collision with the atoms of the structure.

Next, the surface area associated with the probe, $A_i$, is calculated by the following equation.

$$A_i = \frac{4}{3} \cdot \frac{\pi (r_{\mathrm{atom}} + r_{\mathrm{probe}})^2}{n} \qquad (7.2)$$

This value represents the accessible surface area that is available to the probe on the original atom. Note that the sum of all $A_i$ over the entire set of atoms $a_i$ corresponds exactly to the total accessible surface area for the framework. Here, since we generate data of the type ($d_i$, $A_i$) for each probe (i.e., an opposing wall distance and an associated accessible surface area), a histogram containing the accessible surface area as a function of the distance $d$ can be generated. This data essentially represents the density of the various wall separations within the framework, and can hence be utilized in assessing the suitability of certain structures towards various applications for which a target wall separation has been established.

**Analysis of Representative Metal-Organic Frameworks.** The opposing surface area calculations described above are now discussed in the context of four well-known metal-organic frameworks (see Figures 7.2-7.5): $Mg_2(dobdc)$ ($dobdc^{4-}$ = 2,5-dioxido-1,4-benzenedicarboxylate; Mg-MOF-74, CPO-27-Mg),[15] $Cu_3(BTC)_2$ ($BTC^{3-}$ = 1,3,5-benzenetricarboxylate; HKUST-1),[16] $Zn_4O(BDC)_3$ ($BDC^{2-}$ = 1,4-benzenedicarboxylate; MOF-5),[17] and $Zn_4O(BTB)_2$ ($BTB^{3-}$ = 1,3,5-benzenetribenzoate; MOF-177).[18] These particular structures have been selected based on the diversity of their pore volumes, surface areas, and pore system dimensionality. The compound $Mg_2(dobdc)$ (Figure 7.2; $SA_{BET}$ = 1675 $m^2/g$) possesses a honeycomb-type structure consisting of a hexagonal arrangement of one-dimensional channels, with exposed $Mg^{2+}$ cations at each of the vertices. The structure of $Cu_3(BTC)_2$ (Figure 7.3; $SA_{BET}$ = 1200 $m^2/g$) consists of a cubic twisted boracite network topology based on dinuclear $Cu^{2+}$ paddlewheel units connected by triangular $BTC^{3-}$ linkers. Here, octahedral cages share corners to generate a three-dimensional structure possessing two types of pores: the voids within the octahedra, and the three-dimensional channels on the exterior of the cages. The compound MOF-5 (Figure 7.4; $SA_{BET}$ = 3800 $m^2/g$) is one of the most well-studied metal-organic frameworks, and comprises a cubic

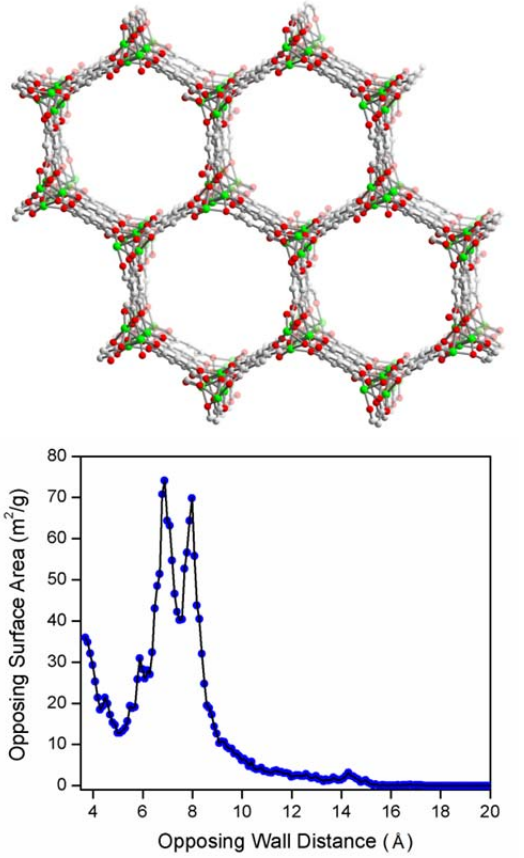


***Figure 7.2.*** (upper) A portion of the crystal structure of $Mg_2(dobdc)$ ($dobdc^{4-}$ = 2,5-dioxido-1,4-benzenedicarboxylate; Mg-MOF-74, CPO-27-Mg). Green, gray and red spheres represent Mg, C and O atoms, respectively. H atoms have been omitted for clarity. (lower) Opposing surface area distribution (OSAD) for $Mg_2(dobdc)$ as calculated with a 3.68-Å probe molecule diameter and a 0.1-Å step size.

network of $[Zn_4O]^{6+}$ clusters coordinated in an octahedral fashion by the linear $BDC^{2-}$ linkers to generate a high-surface area structure with voids extending in three dimensions. Finally, MOF-177 (Figure 7.5; $SA_{BET}$ = 5400 $m^2/g$) is one of the highest-surface area materials reported to date, consisting of significantly larger pores than the other structures considered here, and possessing numerous pore windows that provide access between the large pores.

**$Mg_2$(dobdc).** The opposing surface area distribution generated from the crystal structure of $Mg_2$(dobdc), as obtained with a step size of 0.1 Å, is displayed in Figure 7.2. Interestingly, most of the surface area within the material has an opposing surface disposed between 6 to 9 Å, which is significantly smaller than the distance of ca. 13.8 Å between the surfaces of two $Mg^{2+}$ cations on opposing vertices of the hexagonal pores of the channels, or the separation of ca. 11.7 Å between the surfaces of two benzene rings on opposing edges. This serves to highlight the considerable effect of surface corrugations on the opposing surface area calculations, in which the spherical distribution of surface normals on each atom lead to the probe molecules being

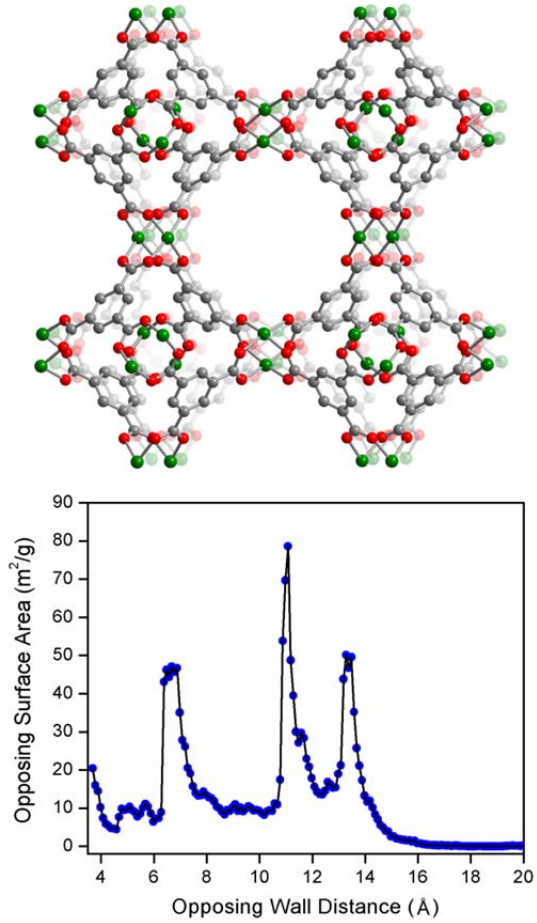


***Figure 7.3*** (upper) A portion of the crystal structure of $Cu_3(BTC)_2$ ($BTC^{3-}$ = 1,3,5-benzenetricarboxylate; HKUST-1). Green, gray and red spheres represent Cu, C and O atoms, respectively. H atoms have been omitted for clarity. (lower) Opposing surface area distribution (OSAD) for $Cu_3(BTC)_2$ as calculated with a 3.68-Å probe molecule diameter and a 0.1-Å step size.

projected toward a variety of opposing surfaces within the channels. For rigid framework structures, as is the case here, such a result is of particular significance, because it reflects the likely trajectories taken subsequent to collision of an adsorbate molecule with the surface. Regardless, the relatively narrow distribution of opposing surface distances is consistent with the one-dimensional nature of the pores, in which the dense walls of the framework prevent the probe spheres from being admitted into adjacent channels.

**$Cu_3(BTC)_2$.** In the case of $Cu_3(BTC)_2$, the opposing surface area distribution exhibits three main maxima at 6.7, 11.1, and 13.3 Å, respectively, as shown in Figure 7.3. Upon close examination of the crystal structure, the 7 Å distances predominantly arise due to probes that are inserted and moved within the octahedral cages. Meanwhile, the surfaces disposed at distances of 12 and 14 Å represent opposing surfaces within the larger three-dimensional channels that extend throughout the structure. Notably, there is also a small amount of opposing surface area below a separation of 5 Å. This portion of the distribution corresponds to probes that are inserted

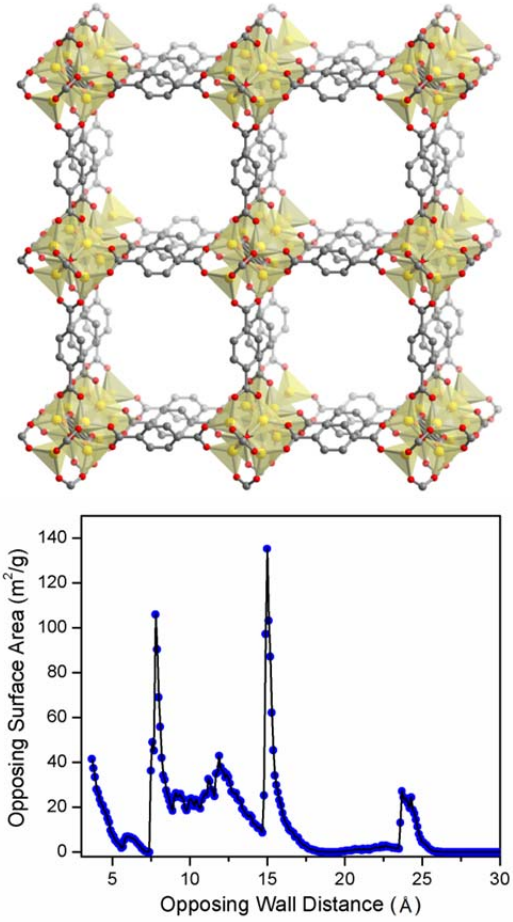


***Figure 7.4*** (upper) A portion of the crystal structure of $Zn_4O(BDC)_3$ ($BDC^{2-}$ = 1,4-benzenedicarboxylate; MOF-5). Yellow, gray and red spheres represent Zn, C and O atoms, respectively, while yellow tetrahedra represent $ZnO_4$ units. H atoms have been omitted for clarity. (lower) Opposing surface area distribution (OSAD) for $Zn_4O(BDC)_3$ as calculated with a 3.68-Å probe molecule diameter and a 0.1-Å step size.

within relatively small pockets, such as the windows of the octahedral cages.

**MOF-5.** For MOF-5, which features three-dimensional pores, three narrow peaks are observed in the opposing surface area distribution at approximately 7.8, 15.0, 23.8 Å, as shown in Figure 7.4. Since most of the surfaces facilitating adsorption in MOF-5 originate from the organic $BDC^{2-}$ linkers, these distances correlate with the mutual separation between the linkers within the structure. Indeed, the 8-Å peak represents the separation between nearest parallel linkers in a single square pore, while the feature at 15 Å is attributable to diagonally opposing linkers within the pores. The broader feature at 24 Å corresponds to the separation between the organic surfaces of two adjacent square pores, and the distribution exhibits no opposing surfaces that are separated by greater than 26 Å. This indicates that the path of the surface normals are such that the probe molecules collide with the framework atoms within the same unit cell or one that is immediately adjacent to the unit cell in which it is generated. It should be noted that, unlike for the previous two examples, the results here could be significantly impacted by taking into account the dynamics of the benzene rings, which are able to rotate with a low activation barrier.[19] The relative importance of such framework dynamics, which are not accounted for here,

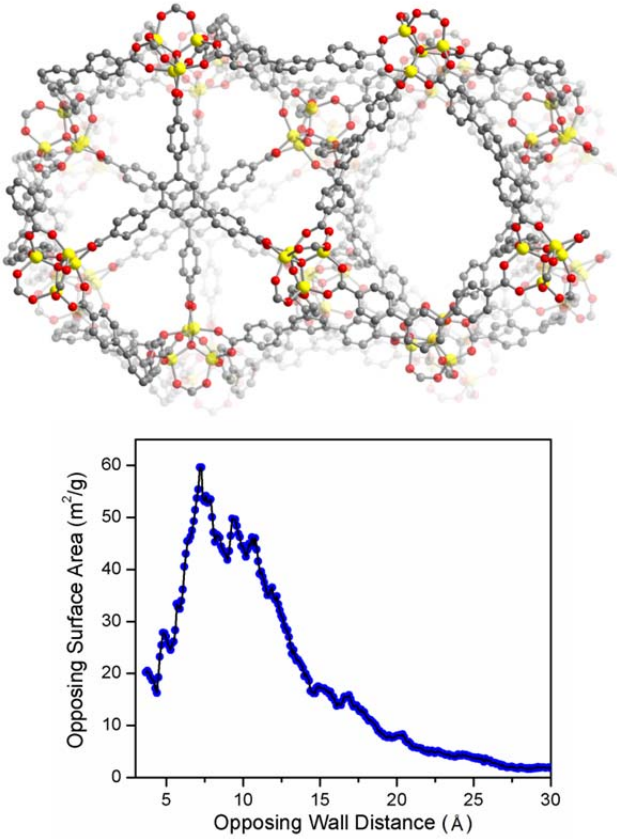


***Figure 7.5*** (upper) A portion of the crystal structure of $Zn_4O(BTB)_2$ ($BTB^{3-}$ = 1,3,5-benzenetribenzoate; MOF-177). Yellow, gray and red spheres represent Zn, C and O atoms, respectively. H atoms have been omitted for clarity. (lower) Opposing surface area distribution (OSAD) for $Zn_4O(BTB)_2$ as calculated with a 3.68-Å probe molecule diameter and a 0.1-Å step size.

will depend on the specifics of the connectivity of the framework structure, as well as the temperature probed.

**MOF-177.** The opposing surface area distribution for MOF-177 is displayed in Figure 7.5. Owing to the relatively anisotropic shape of the pores—where each ellipsoid-shaped cage within the structure is terminated by $[Zn_4O]^{6+}$ clusters approximately 45 Å apart while reaching a width of just over 21 Å—and the high density of small rings and narrow voids within the cages, the distribution is much broader than the other examples presented here. As a consequence of the surface area of the material stemming predominantly from the organic surfaces on the $BTB^{3-}$ ligands, and the fact that the edges of these linkers form a large number of small apertures within the structure, the maximum opposing surface area is observed at wall separations between 6 and 11 Å. However, the surfaces that constitute the walls within the large cavities also contribute a significant proportion of the surface area, resulting in a broad profile at wall separations above 10 Å. Despite the high surface area, with such a broad distribution of opposing surfaces, frameworks of this type would not expected to be optimal for applications in which a specific interwall separation is sought.

**Screening of Metal-Organic Frameworks for High-Density Methane Storage.** The dense storage of methane within metal-organic frameworks is an area that is being actively investigated owing to its possible implementation in mobile applications. Indeed, a number of materials have been demonstrated to exhibit volumetric storage capacities approaching (and in some cases, exceeding) the U.S. Department of Energy volumetric storage target of 180 v/v at 298 K and 35 bar.[20] The discovery of new metal-organic frameworks with enhanced methane storage capacities requires a detailed knowledge of the structural and chemical features that would afford the increase in performance. A recent computational study has demonstrated the significance of the pore size in dictating the adsorption capacity, in which a screening of a large database consisting of isotherms generated by the grand canonical Monte Carlo method for over 130,000 hypothetical structures has revealed that pore sizes around 4 and 8 Å (which roughly correspond to the separation necessary to accommodate one or two methane molecules, respectively) exhibited the highest storage densities.[6]

Currently, the metal-organic framework $Cu_2(adip)$ ($adip^{4-}$ = 5,5′-(9,10-anthracenediyl)diisophthalate; PCN-14), which features pore surfaces that are decorated with exposed $Cu^{2+}$ cation sites on the axial positions of dinuclear paddlewheel units, arguably exhibits the best performance in terms of the absolute volumetric methane uptake, reaching 230 v/v(STP) at 298 K and 35 bar.[21,22] Here, the high uptake is ascribed to the close approach (and dense packing) of the methane molecules adsorbed on the $Cu^{2+}$ centers, as well as to the presence of small cages that also act as preferable binding sites. Note that the contribution of the adsorption within the cages constitutes a significant fraction of the total adsorption under these conditions, since the full occupancy of the $Cu^{2+}$ adsorption sites would afford a maximum volumetric adsorption capacity of just 160 v/v(STP). Thus, the organic surfaces within $Cu_2(adip)$ also act as suitable binding sites for methane, and a recent study[23] has suggested the potential role of the relatively close match between the size of methane and the void spaces within the cages in affording the high methane uptake.

The opposing surface area distribution for $Cu_2$(adip) is displayed in Figure 7.6. Indeed, as a result of the small cages that constitute the three-dimensional network, the bulk of the distribution is concentrated towards wall separations of 8 Å and below, with virtually no opposing surfaces separated by more than 12 Å. As such, the high volumetric storage capacity of $Cu_2$(adip) is likely to be primarily due to the high density of opposing surface area at approximately 4 Å, and also the low fraction of larger voids (> 8 Å). Note that the minimization of wall separations exceeding 8 Å would also be important for boosting the volumetric storage capacity, because it maximizes the van der Waals interactions between methane molecules and the surface of the material. Although the opposing surface area distribution of $Cu_2$(adip) is ideal in this regard, a significant portion of the surfaces are separated by intermediate distances (i.e., greater than 4 Å and less than 8 Å), suggesting that materials featuring narrower distributions centered at either 4 or 8 Å would be worthy of further study by high-pressure methane adsorption experiments.

Owing to the availability of high-pressure methane adsorption data at conditions relevant to mobile methane storage, similar opposing surface area analyses were performed for a collection of representative materials exhibiting a broad range of volumetric adsorption capacities, and the resulting data are tabulated together with the experimental methane adsorption capacities in Table 7.1. In addition to the reported BET and Langmuir surface areas, the calculated accessible surface area is presented here, since a good match between the experimental and calculated surface area is an important aspect in ensuring that the material has been synthesized in pure form and fully activated. The volumetric surface area, which is computed from the accessible surface area and the theoretical crystallographic density obtained

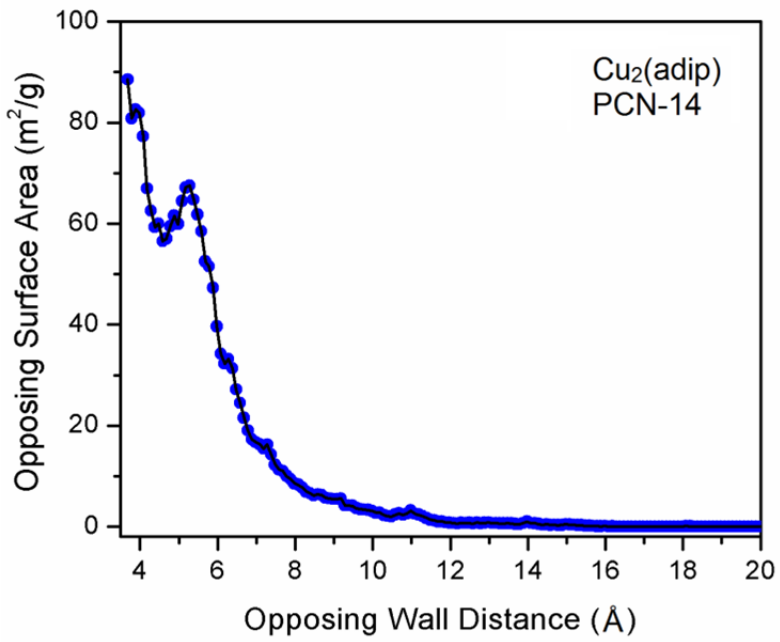


***Figure 7.6.*** The opposing surface area distribution for $Cu_2$(adip) (PCN-14), as calculated with a 3.68-Å probe molecule diameter and a probe step size of 0.1 Å. The small cages that constitute the structure lead to virtually no opposing surfaces that are separated by more than 10 Å, with the bulk of the surfaces less than 6 Å apart.

from the desolvated crystal structure, is also of interest when considering the volumetric storage performance, and is also tabulated to aid the following discussion.

An examination of the compounds with the highest volumetric adsorption capacities reveals that most of the materials possess pore surfaces decorated with exposed metal cations, which act as highly polarizing binding sites. Indeed, the isosteric heat of adsorption ($Q_{st}$) of methane within these materials is as high as –30 kJ/mol in $Cu_2$(adip),[21] and is considerably higher than the corresponding values for materials that facilitate adsorption only on organic surfaces. In these cases, the $Q_{st}$ is generally in the range –13 to –17 kJ/mol, which is similar to the heat of adsorption observed for the dispersion-type interactions that predominate within carbon-based adsorbents.[24]

With regard to materials that do not possess exposed metal cation sites, the highest adsorption capacity to date has been observed in Cr(OH)(BDC) (MIL-53(Cr)), which exhibits a volumetric uptake of 165 v/v(STP) at 35 bar and 304 K.[25] Surprisingly, this is substantially higher than the value observed in MOF-5 (135 v/v(STP) at 36 bar and 298 K),[1a] which exhibits a much higher calculated volumetric surface area of 2155 $m^2$/g, compared to just 1475 $m^2$/g for Cr(OH)(BDC). The higher capacity in Cr(OH)(BDC) is presumably due to the predominant opposing surfaces being disposed at a much closer distance of 6.7 Å, and the narrow nature of the opposing surface area distribution about this separation. Note that, although this separation lies between the 4 and 8 Å—distances that are considered optimal for high-density methane storage—it is preferable to the structure of MOF-5, which features several sets of opposing wall distances at ca. 7.8, 11.9, 15.0, and 23.8 Å. Here, the greater separation of the walls is expected to lead to a significant volume of methane that does not experience any influence from the pore walls, and the volumetric capacity is lowered as a result of bulk-like compression of methane.

A screening of almost 100 common metal-organic frameworks using the opposing surface area analysis revealed a distribution for $Zr_6O_4(OH)_4(BDC)_6$ (UiO-66), as displayed in Figure 7.7a, indicating that this material may be suited for high-density methane storage. As shown, the profile is centered about a single sharp peak at 7.1 Å, while a broader feature is also

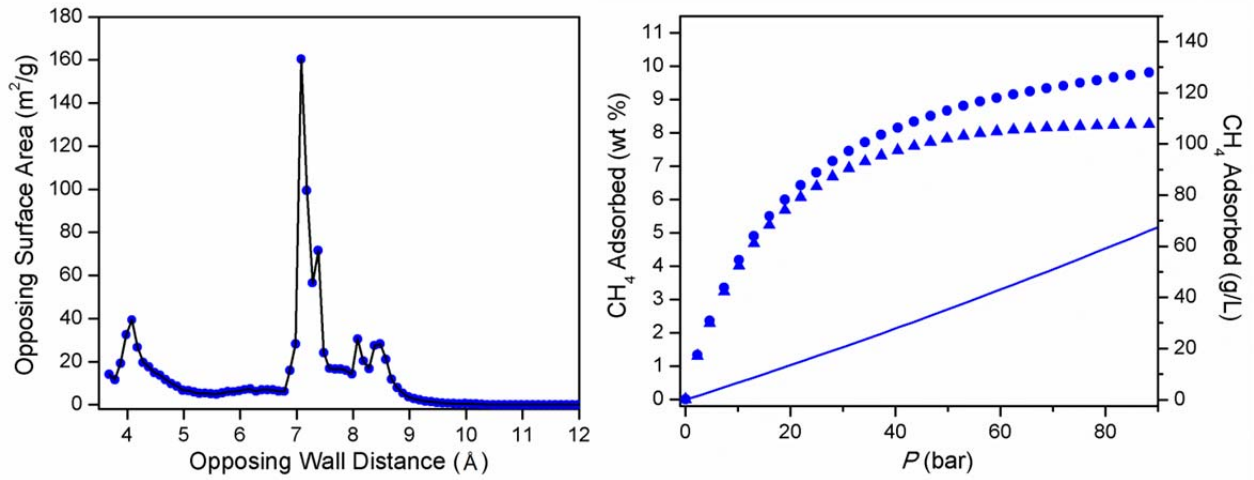


***Figure 7.7*** (a) The opposing surface area distribution for $Zr_6O_4(OH)_4(BDC)_6$ (UiO-66) as calculated with a 3.68-Å probe molecule diameter and a probe step size of 0.1 Å, and (b) the total (circles) and excess (triangles) methane uptake recorded at 298 K. The solid line represents the density of pure methane gas at 298 K as a function of pressure.

observed at smaller separations of ca. 4.1 Å. Although the Langmuir surface area of 1500 $m^2/g$ is modest compared to the highest surface area materials considered in Table 7.1, the narrow distribution of opposing surface distances around the separation distances of interest are expected to be of benefit in the context of the volumetric storage capacity. Indeed, as shown in the high-pressure methane adsorption data recorded at 298 K (see Figure 7.7b), the methane storage capacity reaches 139 v/v(STP) at 35 bar, and 179 v/v(STP) at 90 bar. Although this value lies below those recorded for most of the materials featuring exposed metal cation sites, it ranks among the highest for compounds without such strong adsorption sites. Remarkably, this storage capacity is achieved despite a calculated volumetric surface area of just 1270 $m^2/cm^3$, which is considerably lower than all of the other compounds listed here. This suggests that although strong adsorption sites are of paramount importance for facilitating the close approach of methane to the framework, optimization of the opposing surface area distribution also plays a vital role in boosting the methane storage capacity.

## 7.4 Outlook

The foregoing results demonstrate a convenient and comprehensive method for evaluating the distribution of opposing surface distances within a porous metal-organic framework. The method can be extended to other types of crystalline materials, such as covalent-organic frameworks or zeolites, provided that the unit cell and the coordinates of the framework atoms are available. A screening of common structure types has shown that a wide variety of opposing surface area distributions are already available, and we envisage that this method will assist researchers by allowing new candidate materials for certain applications to be initially identified based on the analysis of their three-dimensional structures, rather than by experimental screening involving time-consuming measurements of the adsorption isotherms. Perhaps more importantly, however, the opposing surface area distribution (OSAD) represents a fundamental characteristic of a porous structure that indicates how well suited it may be for a storage or separation application requiring a specific interwall dimension. Although the method was employed here in the context of studying metal-organic frameworks for high-pressure methane storage, the procedure is expected to be of utility in identifying crystalline materials suitable for other applications, including hydrogen storage, acetylene storage, Xe/Kr separation, and numerous other applications yet to be disclosed. Relatedly, we believe that seeking new framework structures that feature a single intense spike in the OSAD could provide a means of obtaining particularly valuable new adsorbents.

***Table 7.1.*** A comparison of experimental, calculated and predominant opposing surface area distances, and volumetric adsorption capacities of selected metal-organic frameworks.

| Chemical formula[a] | Common name | Surface Area | | | | Main maxima in OSAD | Methane Uptake | Conditions | | $-Q_{st}$ | Exposed cations | Ref. |
|---|---|---|---|---|---|---|---|---|---|---|---|---|
| | | Experimental | | Calculated | | | | | | | | |
| | | BET | Langmuir | Gravimetric | Volumetric | | | *P* | *T* | | | |
| | | ($m^2/g$) | ($m^2/g$) | ($m^2/g$) | ($m^2/cm^3$) | (Å) | (v/v(STP)) | (bar) | (K) | (kJ/mol)[b] | | |
| $Cu_2$(adip) | PCN-14 | 1750 | 2180 | 2080 | 1725 | 3.9, 5.3 | **220** | 35 | 298 | 30.0 | Yes | 21 |
| $Ni_2$(dobdc) | Ni-MOF-74, CPO-27-Ni | 1218 | | 1485 | 1775 | 7.5 | **195** | 35 | 298 | 21.3 | Yes | 26 |
| | | 1027 | | 1485 | 1775 | | **190** | 35 | 298 | 20.2 | | 27 |
| $Co_2$(dobdc) | Co-MOF-74, CPO-27-Co | 1056 | | 1510 | 1820 | 7.0, 8.0 | **174** | 35 | 298 | 19.6 | Yes | 27 |
| $Zn_2$(dobdc) | Zn-MOF-74, CPO-27-Zn | 885 | | 1500 | 1830 | 7.0, 7.9 | **171** | 35 | 298 | 18.3 | Yes | 27 |
| $Cu_2$(sbtc) | PCN-11 | 1930 | 2440 | 3620 | 2385 | 4.0, 5.9 | **170** | 35 | 298 | 14.6 | Yes | 28 |
| $Mg_2$(dobdc) | Mg-MOF-74, CPO-27-Mg | 1542 | | 2020 | 1825 | 6.9, 8.0 | **169** | 35 | 298 | 20.5 | Yes | 26 |
| | | 1332 | | 2020 | 1825 | | **149** | 35 | 298 | 18.5 | | 27 |
| Cr(OH)(BDC) | MIL-53(Cr) | | 1500 | 1415 | 1475 | 6.7 | **165** | 35 | 304 | 17.0 | No | 25 |
| $Cu_3(BTC)_2$ | HKUST-1 | 1502 | 2216 | 2105 | 1865 | 6.7, 11.1, 13.3 | **160** | 35 | 298 | | Yes | 29 |
| $Mn_2$(dobdc) | Mn-MOF-74, CPO-27-Mn | 1102 | | 1545[c] | 1815[c] | 7.0, 8.0 | **158** | 35 | 298 | 19.1 | Yes | 27 |
| Al(OH)(BDC) | MIL-53(Al) | | 1500 | 1455 | 1425 | 6.7 | **155** | 35 | 304 | 17.0 | No | 25 |
| $Zn_4O(dbdc)_3$ | IRMOF-6 | 2804 | 3305 | 3090 | 2020 | 15.0 | **155** | 36 | 298 | | No | 1a |
| $Cu_2(BDC)_2$(dabco) | | | 1819 | 2203[d] | 1830[d] | 4.1, 6.6, 9.6 | **153** | 35 | 298 | 16.3 | No | 30 |
| $Cu_3$(btei) | PCN-61 | 3000 | 3500 | 3540 | 2115 | 7.4, 13.2, 20.1 | **145** | 35 | 298 | 13.8 | Yes | 31 |
| $Co_2(BDC)_2$(dabco) | | 1600 | 2300 | 2241[d] | 1830[d] | 4.1, 6.6, 9.6 | **140** | 35 | 303 | | No | 32 |
| $Zr_6O_4(OH)_4(BDC)_6$ | UiO-66 | | | 1080 | 1270 | 4.1, 7.1 | **139** | 35 | 298 | | No | This work |
| $Zn_2(BDC)_2$(dabco) | | 1450 | | 2190 | 1830 | 4.1, 6.6, 9.6 | **137** | 35 | 296 | 13.6[e] | No | 33 |
| $Zn_4O(BDC)_3$ | MOF-5 | 2296 | 3840 | 3630 | 2155 | 7.8, 11.9, 15.0, 23.8 | **135** | 36 | 298 | | No | 1a |
| $Zn_4O(abdc)_3$ | IRMOF-3 | 2446 | 3062 | 3418 | 2130 | 15.0 | **120** | 36 | 298 | | No | 1a |
| $Zn_4O(btb)_2$ | MOF-177 | 4500 | 5340 | 5140 | 2195 | 4.0-13.0 (broad) | **115** | 35 | 298 | | No | 34 |
| Al(OH)(BPDC) | DUT-5 | 1613 | 2335 | 2450 | 1600 | 11.6, 13.1 | **105** | 35 | 303 | | No | 35 |

[a]$abdc^{2-}$ = 2-amino-1,4-benzenedicarboxylate;$adip^{4-}$ = 5,5'-(9,10-anthracenediyl)diisophthalate; $BDC^{2-}$ = 1,4-benzenedicarboxylate; $BPDC^{2-}$ = 4,4'-biphenyldicarboxylate; $btb^{3-}$ = 1,3,5-benzenetribenzoate; $BTC^{3-}$ = 1,3,5-benzenetricarboxylate; $btei^{6-}$ = 5,5',5''-benzene-1,3,5-triyltris(1-ethynyl-2-isophthalate); dabco = 1,4-diazabicyclo[2.2.2]octane; $dbdc^{2-}$ = 1,2-dihydrocyclobutabenzene-3,6-dicarboxylate; $dobdc^{4-}$ = 2,5-dioxido-1,4-benzenedicarboxylate; $sbtc^{4-}$ = *trans*-stilbene-3,3',5,5'-tetracarboxylate. [b]Unless otherwise stated, calculated using the Clausius-Clapeyron equation. [c]Calculated using the atomic coordinates and unit cell of $Co_2$(dobdc) due to the lack of a suitable crystal structure. [d]Calculated using the atomic coordinates and unit cell of $Zn_2(bdc)_2$(dabco) due to the lack of a suitable crystal structure. [e]Isosteric heat calculated from a virial-type expression.

## 7.5 Acknowledgments

This research was funded by the U.S. Department of Energy through Grant LP0025051. I acknowledge Fulbright New Zealand for partial support, and Prof. R. Krishna for helpful discussions.

## 7.6 References and Notes

(1) (a) Eddaoudi, M.; Kim, J.; Rosi, N.; Vodak, D.; Wachter, J.; O'Keeffe, M.; Yaghi, O. M. *Science* **2002**, *295*, 469. (b) Matsuda, R.; Kitaura, R.; Kitagawa, S.; Kubota, Y.; Belosludov, R. V.; Kobayashi, T. C.; Sakamoto, H.; Chiba, T.; Takata, M.; Kawazoe, Y.; Mita, Y. *Nature* **2005**, *436*, 238. (c) Millward, A. R.; Yaghi, O. M. *J. Am. Chem. Soc.* **2005**, *127*, 17998. (d) Furukawa, H.; Miller, M. A.; Yaghi, O. M. *J. Mater. Chem.* **2007**, *17*, 3197. (e) Ma, S.; Sun, D.; Simmons, J. M.; Collier, C. D.; Yuan, D.; Zhou, H. C. *J. Am. Chem. Soc.* **2008**, *130*, 1012. (f) Morris, R. E.; Wheatley, P. S. *Angew. Chem. Int. Ed.* **2008**, *47*, 4966. (g) Llewellyn, P. L.; Bourrelly, S.; Serre, C.; Vimont, A.; Daturi, M.; Hamon, L.; De Weireld, G.; Chang, J.-S.; Hong, D.-Y.; Hwang, Y. K.; Jhung, S. H.; Férey, G. *Langmuir* **2008**, *24*, 7245. (h) Furukawa, H.; Ko, N.; Go, Y. B.; Aratani, N.; Choi, S. B.; Choi, E.; Yazaydin, A. Ö; Snurr, R. Q.; O'Keeffe, M.; Kim, J.; Yaghi, O. M. *Science* **2010**, *329*, 424.

(2) Metal-organic frameworks were recently the topic of special themed issues of *Chem. Soc. Rev.* and *Chem. Rev.* See: (a) Long, J. R.; Yaghi, O. M. *Chem. Soc. Rev.* **2009**, *38*, 1213. (b) Zhou, H.-C.; Long, J. R.; Yaghi, O. M. *Chem. Rev.* **2012**, *112*, 673.

(3) (a) Wang, Z.; Cohen, S. M. *Chem. Soc. Rev.* **2009**, *38*, 1315. (b) Deshpande, R. K.; Minnaar, J. L.; Telfer, S. G. *Angew. Chem., Int. Ed.* **2010**, *49*, 4598. (c) Tanabe, K. K.; Cohen, S. M. *Chem. Soc. Rev.* **2011**, *40*, 498.

(4) Rzepka, M.; Lamp, P.; de la Casa-Lillo, M. A. *J. Phys. Chem. B* **1998**, *102*, 10894.

(5) Sikora, B. J.; Wilmer, C. E.; Greenfield, M. L.; Snurr, R. Q. *Chem. Sci.* **2012**, Advance Article. DOI: 10.1039/C2SC01097F.

(6) Wilmer, C. E.; Leaf, M.; Lee, C. Y.; Farha, O. K.; Hauser, B. G.; Hupp, J. T.; Snurr, R. Q. *Nat. Chem.* **2012**, *4*, 83.

(7) Schaate, A.; Pascal, R.; Godt, A.; Lippke, J.; Waltz, F.; Wiebcke, M.; Behrens, P. *Chem. Eur. J.* **2011**, *17*, 6643.

(8) The source code for the opposing surface area distribution (OSAD) program is available free of charge on the Internet, at http://alchemy.cchem.berkeley.edu/OSAD/.

(9) Microsoft Visual C++ 2010 Express, http://www.microsoft.com/visualstudio/en-us/products/2010-editions/visual-cpp-express, (accessed June 2012).

(10) Allen, F. H. *Acta Crystallogr.* 2002, *B58*, 380.

(11) Rappe, A. K.; Casewit, C. J.; Colwell, K. S.; Goddard, W. A.; Skiff, W. M. *J. Am. Chem. Soc.* **1992**, *114*, 10024.

(12) Kaye, S. S.; Dailly, A.; Yaghi, O. M.; Long, J. R. *J. Am. Chem. Soc.* **2007**, *129*, 14176.

(13) Düren, T.; Millange, F.; Férey, G.; Walton, K. S.; Snurr, R. Q. *J. Phys. Chem. C* **2007**, *111*, 15350.

(14) Walton, K. S.; Snurr, R. Q. *J. Am. Chem. Soc.* **2007**, *129*, 8552.

(15) Koh, K.; Wong-Foy, A. G.; Matzger, A. J. *J. Am. Chem. Soc.* **2009**, *131*, 4184.

(16) Chui, S. S.-Y.; Lo, S. M.-F.; Charmant, J. P. H.; Orpen, A. G.; Williams, I. D. *Science* **1999**, *283*, 1148.

(17) Rosi, N. L.; Eckert, J.; Eddaoudi, M.; Vodak, D. T.; Kim, J.; O'Keeffe, M.; Yaghi, O. M. *Science* **2003**, *300*, 1127.
(18) Chae, H, K.; Siberio-Pérez, D. Y.; Kim, J.; Go, Y.; Eddaoudi, M.; Matzger, A. J.; O'Keeffe, M.; Yaghi, O. M. *Nature* **2004**, *427*, 523.
(19) Gould, S. L.; Tranchemontagne, D.; Yaghi, O. M.; Garcia-Garibay, M. A. *J. Am. Chem. Soc.* **2008**, *130*, 3246.
(20) Burchell, T.; Rogers, M. *SAE Tech. Pap. Ser.* **2000**, 2001-2205.
(21) Ma, S.; Sun, D.; Simmons, J. M.; Collier, C. D.; Yuan, D.; Zhou, H.-C. *J. Am. Chem. Soc.* **2008**, *130*, 1016.
(22) Note that more recent simulation work predicts a significantly lower adsorption capacity for PCN-14 at 298 K and 35 bar of 197 v/v(STP) (see ref. 6).
(23) Wu. H.; Simmons, J. M.; Liu, Y.; Brown, C. M.; Wang, X.-S.; Ma, S.; Peterson, V. K.; Southon, P. D.; Kepert, C. J.; Zhou, H.-C.; Yildirim, T.; Zhou, W. *Chem. Eur. J.* **2010**, *16*, 5205.
(24) Piper, J.; Morrison, J. A. *Phys. Rev. B* **1984**, *30*, 3486.
(25) Bourrelly, S. Llewellyn, P. L.; Serre, C.; Millange, F.; Loiseau, T.; Férey. G. *J. Am. Chem. Soc.* **2005**, *127*, 13519.
(26) Dietzel, P. D. C.; Besikiotis, V.; Blom, R. *J. Mater. Chem.* **2009**, *19*, 7362.
(27) Wu, H.; Zhou, W.; Yildirim, T. *J. Am. Chem. Soc.* **2009**, *131*, 4995.
(28)Wang, X.-S.; Ma, S.; Rauch, K.; Simmons, J. M.; Yuan, D.; Wang, X.-S.; Yildirim, T.; Cole, W. C.; Lopez, J. J.; De Meijere, A.; Zhou, H.-C. *Chem. Mater.* **2008**, *20*, 3145.
(29) Senkovska, I.; Kaskel. S. *Microporous Mesoporous Mater.* **2008**, *112*, 108.
(30) Seki, K.; Mori, W. *J. Phys. Chem. B* **2002**, *106*, 1380.
(31) Yuan, D.; Zhao, D.; Sun, D.; Zhou, H.-C. *Angew. Chem., Int. Ed.* **2010**, *49*, 5357.
(32) Wang, H.; Getzschmann, J.; Senkovska, I.; Kaskel. S. *Microporous Mesoporous Mater.* **2008**, *116*, 653.
(33) Kim, H.; Samsonenko, D. G.; Das, S.; Kim, G. H.; Lee, H. S.; Dybtsev, D. N.; Berdonosova, E. A.; Kim, K. *Chem. Asian J.* **2009**, *4*, 886.
(34) Mendoza-Cortés, J. L.; Han, S. S.; Furukawa, H.; Yaghi, O. M.; Goddard, W. A. *J. Phys. Chem. A* **2010**, *114*, 10824.
(35) Senkovska, I.; Hoffmann, F.; Fröba, M.; Getzschmann, J.; Böhlmann, W.; Kaskel, S. *Microporous Mesoporous Mater.* **2009**, *122*, 93.

# Appendix A: Evaluation of the Heat Capacity of Metal-Organic Frameworks – Implications on Temperature-Swing Adsorption-Based CO2 Capture Processes

## A.1 Introduction

The regeneration step of a temperature-swing adsorption (TSA) process requires heating of the sorbent up to the desorption temperature, which, depending on the specific configuration of the power plant, may be as high as 200 ºC. One parameter that is expected to impact considerably the efficiency of this process is the heat capacity ($C_p$) of the sorbent. The use of a low-heat capacity sorbent would be expected to afford a lower energy penalty for the regeneration step, which would be of significant benefit for reducing the total energy cost of post-combustion $CO_2$ capture. Herein, we examine the heat capacities of two representative metal-organic frameworks that have been examined for a variety of gas storage and molecular separation applications. $Zn_4O(BTB)_2$ ($BTB^{3-}$ = 1,3,5-benzenetribenzoate; MOF-177) features a high BET surface area of 4690 $m^2/g$ and a large pore volume, but does not possess strong binding sites for guest molecules owing to its predominantly organic surfaces. Meanwhile, $Mg_2$(dobdc) (MOF-74(Mg); $dobdc^{4-}$ = 2,5-dioxido-1,4-benzenedicarboxylate) possesses a lower BET surface area of 1800 $m^2/g$, but contains one-dimensional pores that are decorated with a high density of exposed $Mg^{2+}$ adsorption sites that facilitate strong interactions with gas molecules. The selection of these two frameworks for study is expected to afford vital information regarding the effect of the chemical composition and network structure on the heat capacity of the bulk materials.

## A.2 Experimental Section

All reagents were obtained from commercial vendors and used without further purification. MOF-177 and $Mg_2$(dobdc) were synthesized and activated according to the literature procedures.

**Heat Capacity Measurements.** All thermal analyses were performed on a TA Instruments Q200 differential scanning calorimeter (DSC) equipped with a refrigerated cooling system RSC90 under a nitrogen or helium flow. Baseline data for the empty heating chamber was collected between temperatures of –90 ºC and 400 ºC, followed by a temperature calibration using the melting point of an indium sample (m.p. 156.60 ºC). The energy axis was calibrated by collecting heat flow data on a sapphire sample (21.8 mg) and fitting this data to the literature values.[1]

A sample of activated MOF-177 (6.5 mg) or $Mg_2$(dobdc) (9.4 mg) was hermetically sealed within an aluminum pan in a glovebox under a nitrogen atmosphere, and the sample was quickly transferred to the calorimeter. The heat flow data were collected using a temperature ramp rate of 3 ºC/min in the temperature range of –50 to 250 ºC, using a temperature modulation of ±1 ºC every 60 s. The sample was then cooled back to –50 ºC, the heating cycle was repeated a further two times, and the data for the three runs were averaged. The heat capacity was obtained using the following expression:

$$C_p(\text{sample}) = \frac{H_{\text{sample}}}{H_{\text{ref}}} \cdot \frac{m_{\text{ref}}}{m_{\text{sample}}} \cdot C_p(\text{ref}) \qquad \text{(A.1)}$$

where $C_p$(sample) and $C_p$(ref) represent the heat capacities of the sample and reference material (sapphire), $H_{\text{sample}}$ and $H_{\text{ref}}$ represent the heat flows for the sample and reference material detected by the calorimeter with respect to an empty aluminum pan, and $m_{\text{sample}}$ and $m_{\text{ref}}$ represent the experimental masses of the sample and reference material, respectively.

### A.3 Results and Discussion

The heat capacities for evacuated samples of MOF-177 and $Mg_2$(dobdc) recorded under a flow of $N_2$ are presented in Figure A.1. Interestingly, $Mg_2$(dobdc) initially exhibits a slight decrease in its heat capacity curve at temperatures up to 60 ºC, presumably due to the desorption of bulk $N_2$ from the pores of the framework. Such an effect is not observed when the heat capacity measurement is conducted under a continuous He flow, since the adsorption of He is negligible across this temperature range. In contrast, MOF-177, which adsorbs only a small quantity of $N_2$ at these temperatures, exhibits a nearly linear increase in the heat capacity with temperature. At temperatures above 60 ºC, the heat capacities of the two materials are similar, reaching ca. 1.6 J $g^{-1}$ $K^{-1}$ at 200 ºC. Nevertheless, consideration of the effect of adsorbed species on the heat capacity will be important in evaluating the regeneration energy requirements of any metal–organic framework in a TSA process since the material will contain significant amounts of adsorbed gas molecules (primarily $CO_2$) during the initial heating. The heat capacity values reported here are comparable to the corresponding values for non-porous metal–organic frameworks and zeolites.[2] Importantly, the heat capacities are considerably lower than those of aqueous alkanolamine solutions, which carry a significant disadvantage in that the water in which the amine molecules are dissolved must also be heated to the desorption temperature of

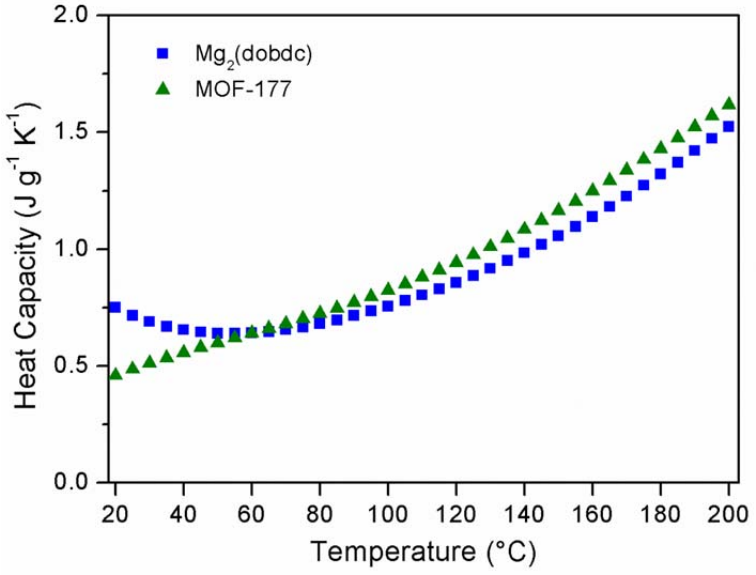


***Figure A.1.*** Heat capacity of MOF-177 (green triangles) and $Mg_2$(dobdc) (blue squares) as a function of temperature as measured under $N_2$.

$CO_2$ (typically > 100 ºC). For example, for a 30 wt % monoethanolamine (MEA) solution, the heat capacity at 25 ºC is 3.73 J $g^{-1}$ $K^{-1}$, which is close to the corresponding value for pure water (4.18 J $g^{-1}$ $K^{-1}$ at 25 ºC), and is more than four times larger than the heat capacities of the metal–organic frameworks studied here.[3] Although the heat capacities of the metal–organic frameworks increase with temperature, the values at 200 ºC are still less than half of the heat capacity of the MEA solution.

### A.4 Outlook

The foregoing results highlight one of the key advantages of adopting a temperature swing adsorption process employing a metal–organic framework, wherein the contribution to the energy penalty arising from heating the adsorbent would be greatly reduced compared to the conventionally employed aqueous amine solutions.

### A.5 Acknowledgments

This research was funded by the Advanced Research Projects Agency - Energy (ARPA-E), U.S. Department of Energy.

### A.6 References and Notes

(1) Archer, D. G. *J. Phys. Chem. Ref. Data* **1993**, *22*, 1441.
(2) (a) Chue, K. T.; Kim, J. N.; Yoo, Y. J.; Cho, S. H.; Yang, R. T. *Ind. Eng. Chem. Res.* **1995**, *34*, 591. (b) Qiu, L.; Murashov, V.; White, M. A. *Solid State Sci.* **2000**, *2*, 841. (c) Song, L.-F.; Jiang, C.-H.; Zhang, J.; Sun, L.-X.; Xu, F.; Tian, Y.-Q.; You, W.-S.; Cao, Z.; Zhang, L.; Yang, D.-W. *J. Therm. Anal. Calorim.* **2009**, *101*, 365. (d) Song, L.-F.; Jiang, C.-H.; Zhang, J.; Sun, L.-X.; Xu, F.; You, W.-S.; Zhao, Y.; Zhang, Z.-H.; Wang, M.-H.; Sawada, Y.; Cao, Z.; Zeng, J.-L. *J. Therm. Anal. Calorim.* **2009**, *100*, 679.
(3) Wieland, R. H.; Dingman, J. C.; Cronin, D. B. *J. Chem. Eng. Data* **1997**, *42*, 1004.

# Appendix B: Synthesis and Structural Flexibility of a Series of Copper(II) Azolate-Based Metal-Organic Frameworks

## B.1 Introduction

Metal-organic frameworks have attracted much recent investigation owing to their high permanent porosity, convenient modular synthesis, and chemical tunability.[1] The ability to judiciously select the metal ion and organic linker suggests that if the appropriate components are combined, frameworks that are tailor-made for specific applications, such as gas storage[2] and separation,[3] may be prepared. However, significant improvements in the understanding of structure-property relationships within this class of material are still needed in order to fulfill their great potential. Indeed, despite the large number of frameworks studied for their gas sorption behavior, flexibility, and chemical stability, it still remains difficult to predict how changes to the framework constituents or network structure might affect the observed properties. Thus, improvements in this regard would greatly aid in materials design, and from a practical point of view, dramatically reduce the number of compounds that need to be studied for the discovery of high-performance materials.

The systematic investigation of the adsorptive and dynamic properties of materials exhibiting a common network topology may allow the effect of subtle changes to the framework, such as the metal node or the functionality or length of the organic bridging unit, to be elucidated. For example, the IRMOF series of frameworks, which feature a cubic network of tetrahedral $[Zn_4O]^{6+}$ clusters bridged by dicarboxylate linkers demonstrates that a common network type can be adopted despite the use of a diverse range of ligands.[1a,4] Meanwhile, in the $M_2$(DOBDC) (M = Mg, Mn, Co, Ni, Zn; $DOBDC^{4-}$ = 2,5-dioxo-1,4-benzenedicarboxylate) and the

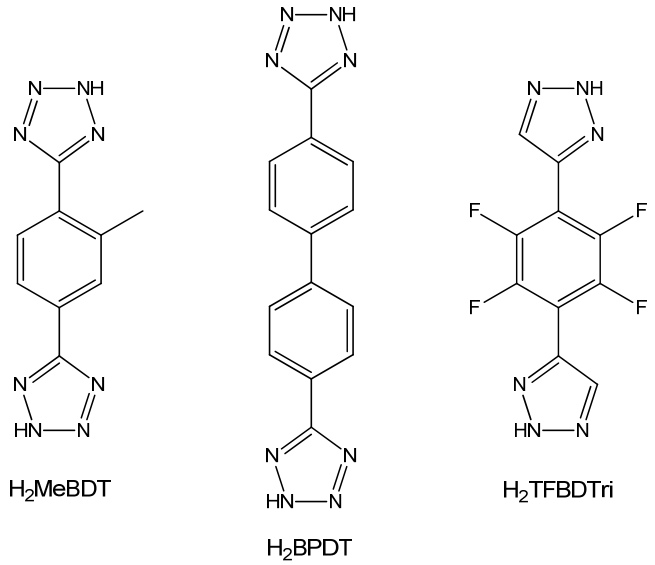


***Figure B.1.*** Organic bridging units employed in the present work; 2-methyl-1,4-benzeneditetrazolate ($H_2$MeBDT), 4,4'-biphenylditetrazolate ($H_2$BPDT), and 2,3,5,6-tetrafluoro-1,4-benzeneditriazolate ($H_2$TFBDTri).

$M_3[(M_4Cl)_3(BTT)_8]_2$ (M = Mn, Fe, Cu; $BTT^{3-}$ = 1,3,5-benzenetristetrazolate) frameworks, the same network connectivity is facilitated by a variety of metals.[5,6] These materials are of significant interest due to the presence of unsaturated coordination sites on the pore surface, and depending on the metal employed the frameworks can exhibit enhanced affinities or selectivities for certain gas molecules, which is crucial for the development of high-performance materials for hydrogen storage and carbon dioxide capture.

In addition to variations in the composition of the materials, metal-organic frameworks exhibiting reversible structural flexibility have also received significant study due to their structural dynamics and unusual response to the adsorption of guest molecules.[7] These materials frequently exhibit stepwise adsorption phenomena owing to transitions in the framework structure, which can be of benefit for gas separation applications. For the separation of gases of very similar kinetic diameters, such as $O_2$ and $N_2$, a potentially viable approach might be to modulate the gate-opening pressure by tuning the internal pore surface of the material. The two strategies mentioned above, namely modification of the metal or ligand component of the framework, are potential avenues for the preparation of optimized materials.

Recently, we have reported two copper-based frameworks; Cu(BDT)(DMF) ($BDT^{2-}$ = 1,4-benzeneditetrazolate), and Cu(BDTri)(L) (L = DMF, DEF; $BDTri^{2-}$ = 1,4-benzeneditriazolate).[8,9] Despite the use of different azolate functional groups, the frameworks are isostructural to each other, and in the case of the triazolate-based materials, the same network topology is adopted despite a different bridging solvent molecule being present in the structure. Interestingly, these materials exhibit reversible changes in the pore dimensions depending on the quantity of guest solvent content of the pores. In the case of the evacuated frameworks, a state in which the pore apertures are closed, a high selectivity of $O_2$ over $N_2$ is observed due to a kinetic sieving effect based on the slightly smaller kinetic diameter of $O_2$ (3.46 Å) compared to $N_2$ (3.64 Å).[10] Here, we extend this library of copper(II) azolate-based metal-organic frameworks derived from three new organic linkers depicted in Figure B.1; 2-methyl-1,4-benzeneditetrazolate ($H_2$MeBDT), 4,4'-biphenylditetrazolate ($H_2$BPDT), and 2,3,5,6-tetrafluoro-1,4-benzeneditriazolate ($H_2$TFBDTri). The ligands have been synthesized for their different functionalities and length, which are anticipated to allow access to unique dynamic properties within the resulting frameworks. Indeed, while the resulting frameworks exhibit the same network topology, they possess significantly different flexibility and chemical stability profiles with respect to exchange of the bridging ligand, demonstrating the exquisite dependence of the framework properties on the organic linker.

## B.2 Experimental Section

**General:** All ligand syntheses were performed under a nitrogen atmosphere using standard Schlenk techniques. Azidomethyl pivalate [11] and 1,4-diethynyl-2,3,5,6-tetrafluorobenzene[12] were prepared as previously reported. All glassware was dried in an oven set to a temperature of 150 °C for 24 h prior to use. Toluene was dried over activated 4 Å molecular sieves, passed through a column of activated alumina, and degassed with nitrogen. Methanol was dried over calcium hydride then distilled. All other syntheses and manipulations were carried out in the air. All reagents were obtained from commercial vendors and used without further purification.

**1,4-ditetrazol-5-yl-2-methylbenzene ($H_2$MeBDT):** Toluene (20 mL) was added to a 100 mL round-bottom flask containing 2-methylterephthalonitrile (0.34 g, 2.4 mmol), sodium azide (0.95 g, 15 mmol) and triethylamine hydrochloride (2.0 g, 15 mmol). The reaction mixture was

heated at reflux for 3 days, after which time a pale-brown solid was observed on the walls of the reaction vessel. The reaction mixture was dissolved in 1 M NaOH (30 mL) and vigorously stirred for 30 min, and the aqueous phase was collected by phase separation. This fraction was treated with 1 M HCl (30 mL) until the pH of the solution was ca. 1, and the resulting white solid was collected by filtration and dried overnight at 120 °C. The dried product was finely ground to yield a pale-yellow powder (0.43 g, 79%). IR (neat): 3137 (m), 3065 (m), 3007 (m br), 2927 (m br), 2827 (m br), 2707 (s br), 2625 (s br), 2495 (s br), 1807 (m br), 1580 (s), 1496 (m), 1454 (m), 1435 (m), 1390 (s), 1350 (w), 1282 (w), 1238 (s), 1153 (m), 1109 (m), 1086 (m), 1030 (m), 986 (s), 920 (s), 887 (s), 835 (s), 741 (s), 705 (w br), $cm^{-1}$. $^1H$ NMR (dmso-$d^6$): $\delta$ 17.10 (br s, 2H, -NH), 8.14 (s, 1H, $H_{Ph}$), 8.07 (d, 1H, $J$ = 8 Hz, $H_{Ph}$), 7.96 (d, 1H, $J$ = 8 Hz, $H_{Ph}$), 2.61 (s, 3H, $-CH_3$) ppm.

**4,4'ditetrazol-5-yl-biphenyl ($H_2$BPDT):** Toluene (20 mL) was added to a 100 mL round-bottom flask containing 4,4-biphenyldicarbonitrile (0.50 g, 2.4 mmol), sodium azide (0.95 g, 15 mmol) and triethylamine hydrochloride (2.0 g, 15 mmol). A workup procedure analogous to $H_2$MeBDT was followed, yielding the pure product as an off-white powder (0.61 g, 87%). Anal. Calcd. for $C_{14}H_{10}N_8$ (290.28): C, 57.93; H, 3.47; N, 38.60. Found: C, 57.75; H, 3.49; N, 38.30. IR (neat): 3130 (m br), 3064 (m br), 3005 (m br), 2853 (s br), 2731 (s br), 2645 (s br), 1612 (s), 1556 (m), 1486 (s), 1423 (s), 1158 (m), 1055 (m), 1034 (m), 987 (m), 847 (w), 823 (s), 741 (s), 698 (w), $cm^{-1}$. $^1H$ NMR (dmso-$d^6$): $\delta$ 17.01 (br s, 2H, -NH), 8.21 (d, 4H, $J$ = 8 Hz, $H_{Ph}$), 8.04 (d, 4H, $J$ = 8 Hz, $H_{Ph}$). MS(FAB$^+$): m/z 289 ([M-H]$^+$: 37%).

**4,4'-(Perfluoro-1,4-phenylene)bis(1H-1,2,3-triazole-4,1-diyl)bis(methyl-ene)bis(2,2-dimethylpropanoate) (FBTriMP):** Water (3 mL) and t-butanol (6 mL) were added to a 50-mL round-bottom flask containing 4-diethynyl-2,3,5,6-tetrafluorobenzene (0.17 g, 0.83 mmol) and azidomethyl pivalate (0.29 g, 1.8 mmol). Sodium L-ascorbate (17 mg, 0.042 mmol) and 1 M $CuSO_4$ solution (42 μL, 0.083 mmol) were added under vigorous stirring. The reaction mixture was heated to 60 $^oC$ for 16 h after which time an orange solid was observed. 10 mL of ice water was added, followed by 10% $NH_3$ solution (3 mL). The resultant suspension was stirred for 2 h, and the product isolated by filtration, washing with water and drying under vacuum to yield a pale orange powder powder (0.35 g, 82%). Anal. Calcd. for $C_{22}H_{24}F_4N_6O_4$ (512.46): C, 51.56; H, 4.72; N, 16.40. Found: C, 51.29; H, 4.62; N, 16.10. IR (neat): 3093 (w), 2983 (w), 1743 (s), 1490 (s), 1435 (m), 1389 (m), 1355 (w), 1275 (m), 1232 (m), 1116 (vs), 1058 (m), 1035 (s), 999 (m), 972 (s), 915 (m), 873 (w), 826 (m), 790 (m), 763 (m), 725(w), 674 (w), 631(w), 584 (w), 532 (w) $cm^{-1}$. $^1H$ NMR (dmso-$d^6$): δ 8.82 (s, 2 H, -CH), 6.46 (s, 4 H, $-CH_2$), 1.15 (s, 18 H, $-C(CH_3)_3$) ppm. $^{19}F$ NMR (dmso-$d^6$): -140 ppm.

**2,3,5,6-tetrafluoro-1,4-benzeneditriazolate ($H_2$TFBDTri):** Methanol (5 mL) and water (5 mL) were added to FBTriMP (0.55 g, 1.1 mmol) in a 50 ml glass round-bottom flask and vigorously stirred for 5 hours. 40 ml of water was added and the mixture extracted with 4 × 20 ml of ether. The aqueous layer was then acidified with an excess of 1 M HCl to obtain an off-white precipitate. The product was filtered and copiously washed with water, ether and dichloromethane and dried under vacuum to afford an off-white powder (0.21 g, 70% yield). The product can be further purified if necessary from residual copper catalyst by dissolution in 15% aqueous ethylene diamine, followed by precipitation with 1 M HCl and washing with water, ether and dichloromethane. IR (neat): 3098 (br w), 2883 (br m), 2784 (br m), 2661 (br m), 1474 (s), 1445 (m), 1404 (w), 1348 (w), 1245 (m), 1234 (m), 1203 (m), 1157 (m), 1147 (m), 1081 (m), 1018 (w), 976 (vs), 907 (m), 854 (m), 825 (m), 781 (m), 727 (w), 673 (w), 619 (w) $cm^{-1}$. $^1H$ NMR (dmso-$d^6$) δ = 15.73 (br s, 2 H, -NH), 8.41 (br s, 2 H, -CH) ppm. $^{13}C$ NMR (dmso-$d^6$) δ =

144 (d, $^{1}J_{C\text{-}F}$= 254 Hz, -CF), 134 (s, -$C_{Ar}$), 125 (br s, -CH), 110 (s, $C_{Tri}$) ppm. $^{19}$F NMR (dmso--$d^6$): -135 ppm. MS (HR-ESI): m/z= 284.0438 (100.00%; $^{12}C_{10}H_4N_6F_4$), 285.0462 (12.16 %; $^{12}C_9{}^{13}CH_4N_6F_4$).

**Cu(MeBDT)(DMF) (B.1, Cu-MeBDT):** $H_2$MeBDT (9.0 mg, 0.04 mmol) and $CuCl_22H_2O$ (6.8 mg, 0.04 mmol) were added to a 4 mL scintillation vial. A 1:1 (v/v) mixture of DMF-ethanol (2 mL), and concentrated HCl (20 μL) were added to the solids, and the vial was placed on a hotplate set to 120 °C following tight sealing with a Teflon-lined cap. A blue-purple microcrystalline powder was collected after 2 days to afford 5.0 mg of product (37%). Crystals appropriate for single-crystal X-ray diffraction analysis were prepared as follows. A solution of $H_2$MeBDT (9.0 mg, 0.042 mmol) in DMF (1 mL) was added to a solution of $CuCl_2{\cdot}2H_2O$ (6.8 mg, 0.040 mmol) in methanol (1 mL) in a 4 mL scintillation vial. Concentrated HCl (20 μL, 12 M) was added to the reaction mixture to yield a green solution, which was allowed to stand at room temperature for 5 days. The resulting pale blue rod-shaped crystals were stored in the mother liquor.

**Cu(BPDT)(DMF) (B.2, Cu-BPDT):** $H_2$BPDT (12 mg, 0.041 mmol) and $CuCl_2{\cdot}2H_2O$ (6.8 mg, 0.040 mmol) were added to a 4 mL glass scintillation vial. A 1:1 (v/v) mixture of DMF-methanol (2 mL), and concentrated HCl (20 μL) were added to the solids, and the vial was placed on a hotplate set to 90 °C following tight sealing with a Teflon-lined cap. A blue-purple microcrystalline powder was collected after 2 days to afford 6.0 mg (37 %) of product. IR (neat): 3317 (m br), 3074 (w), 2915 (w), 2539 (m br), 1673 (s), 1590 (s), 1545 (s), 1424 (m), 1369 (m), 1246 (s), 1126 (m), 1024 (s).

**Cu(TFBDTri)(DMF) (B.3, Cu-TFBDTri):** $H_2$TFBDTri (8.5 mg, 0.029 mmol) and $CuCl_2{\cdot}2H_2O$ (51 mg, 0.30 mmol) was added to a 4 ml glass scintillation vial. 3 ml of DMF acidified with 3 drops of 0.2 M $HNO_3$ was added to the solids and the vial placed on a hotplate set to 80 °C following tight sealing with a Teflon-lined cap. A blue-purple microcrystalline powder was collected after 4 days by filtration, washing with DMF and evacuation under vacuum to afford 4 mg of product. This solid is isostructural to CuBDTri(DMF) C phase[9] and its unit cell can be indexed with the same space group, *Imma* with lattice parameters $a$ = 24.53(2) $b$ = 6.959(7) $c$ = 9.393(7) Å. IR (neat): 1643 (s), 1488 (s), 1384 (m), 1370 (sh), 1337 (w), 1245 (w), 1223 (w), 1106 (m), 1060 (w), 1021 (w), 974 (vs), 849 (m), 789 (s), 696 (w), 665 (w), 637 (w), 482 (m).

**Crystal Data for B.1-AS**: $C_{13}H_4CuN_8O$, $M$ = 351.79, orthorhombic, *Imma*, $a$ = 22.709(5) Å, $b$ = 7.1180(14) Å, $c$ = 12.828(3) Å, $V$ = 2073.6(8) Å$^3$, $T$ = 100(2) K, $\lambda$ = 0.71073 Å, $Z$ = 4, $\rho$ = 1.127 g/cm$^3$, 2554 data measured, 470 unique data, $R_{int}$ = 0.0470, $R1$ = 0.0809, $wR2$ = 0.2241 for 470 contributing reflections [$I \geq 2\sigma(I)$], GOF = 0.902.

**Other Physical Measurements:** Powder X-ray diffraction data was collected using Cu Kα radiation (λ = 1.5406 Å) on a Siemens D5000 diffractometer. Indexing of the diffraction patterns for **1-3** was performed within the Bruker EVA software. Single-crystal X-ray diffraction data were collected on a Siemens SMART 1000 diffractometer, and structures were subsequently solved using the SHELXTL 5.0 software package following absorption corrections applied by SADABS. $^1$H NMR spectra were recorded at ambient temperature on Bruker AV-300, AVQ-400, AVB-400, and AV-600 spectrometers, and all chemical shifts are given in relation to residual solvent peaks. Thermogravimetric analyses were carried out on a TA Instruments TGA 2950 at a temperature ramping rate of 4 °C/min under a flow of nitrogen gas. Infrared spectra were collected using a Nicolet Avatar 360 FTIR spectrometer equipped with an attenuated total

reflectance accessory (ATR). Carbon, hydrogen, and nitrogen analyses were performed by the Microanalytical Laboratory at the University of California, Berkeley.

### B.3 Results and Discussion

The combination of $CuCl_2 \cdot 2H_2O$ and $H_2$MeBDT in an acidified mixture of DMF and methanol at room temperature yielded blue-green, block-shaped single crystals of the solvated form of Cu(MeBDT)(DMF) (**B.1-AS**). X-ray analysis of the crystals revealed an orthorhombic network which crystallizes in an orthorhombic space group *Imma* (Figure B.2), which is isostructural to both Cu(BDT)(DMF)[8] and Cu(BDTri)(L) (L = DMF, DEF).[9] The network consists of octahedral $Cu^{2+}$ ions in which the four equatorial coordination sites are coordinated by nitrogen atoms of four different tetrazolate groups, while the axial sites are occupied by bridging DMF molecules resulting in one-dimensional chains in the [010] direction. The individual chains are linked by the $MeBDT^{2-}$ ligands, creating diamond-shaped one-dimensional channels that run parallel to the $Cu^{2+}$ chains. Note that the methyl substituent on the bridging ligand was crystallographically disordered over the four possible sites on the benzene ring. Thermogravimetric analysis of a sample of **B.1-AS** following immersion in dichloromethane revealed that following the initial evaporation of dichloromethane up to approximately 50 °C, the material maintains its structure until approximately 200 °C, above which the bound DMF molecules are lost, resulting in decomposition of the framework. The thermal stability is indeed comparable to that of other tetrazolate-based frameworks reported recently.[6,8]

Surprisingly, the single-crystallinity of the as-synthesized material was lost following evacuation of the pores by immersing the crystals in dichloromethane and evaporating the solvent within the pores under a slow flow of dinitrogen. This is presumably due to the

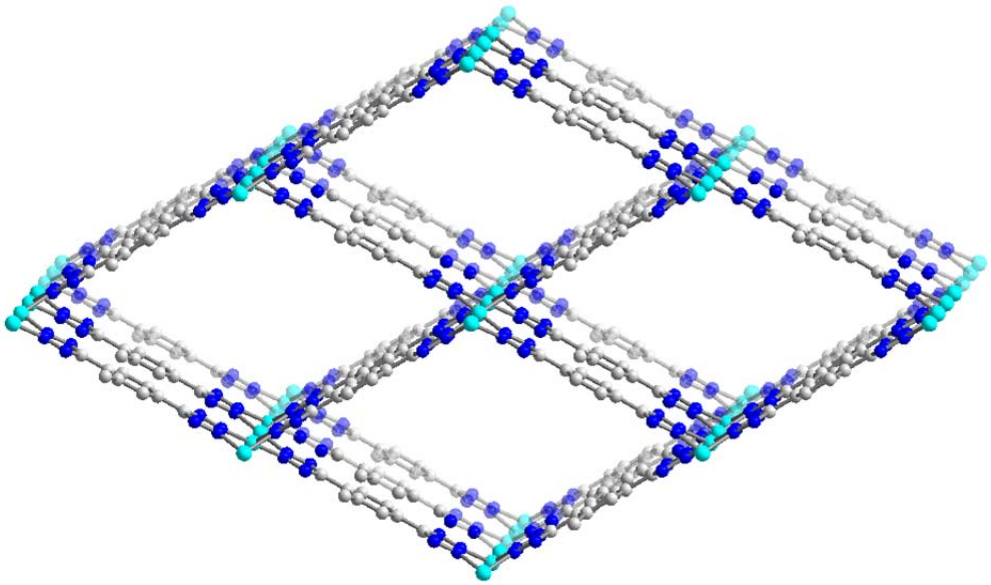

***Figure B.2.*** A portion of the crystal structure of as-synthesized Cu(MeBDT)(DMF) (**B.1-AS**) as viewed down the [010] direction. Turquoise, gray, and blue spheres represent Cu, C, and N atoms, respectively. Hydrogen atoms and bridging DMF molecules have been omitted for clarity.

mechanical stress generated by the significant changes in the dimensions of the channels within the framework. Indeed, comparison of the powder X-ray diffraction pattern of **B.1-AS** (Figure B.3a) with that of the desolvated material (**B.1-DMF**, Figure B.3b) revealed a significant shift in several of the predominant reflections, most notably the (101) reflection. Furthermore, full indexing of the powder pattern was possible to a significantly smaller unit cell within the same space group *Imma*, wherein the cell parameter *c* was significantly contracted compared to the solvated structure, indicating partial collapse of the one-dimensional channels upon removal of the non-coordinated solvent molecules. Infrared spectroscopy confirmed that the bridging DMF molecules, and hence the original network connectivity, had been retained in **B.1-DMF**. Moreover solvation of the pores of **B.1-DMF** by soaking in neat DMF, a powder X-ray diffraction pattern matching that of to **B.1-AS** was obtained, indicating opening of the pore aperture.

The ability of the bridging solvent to be modified in the Cu(BDTri)(L) (L = DMF, DEF) system prompted our efforts to probe the extent to which this is possible for **B.1**. In our hands, while the framework could not be prepared from neat organic solvents other than DMF, we found that the as-synthesized material **B.1-AS** could be immersed in DEF to generate Cu(MeBDT)(DEF) (**B.1-DEF**), in which the bridging DMF solvent molecules were fully displaced by DEF. Furthermore, indexing of the powder X-ray pattern of the dried form of **B.1-**

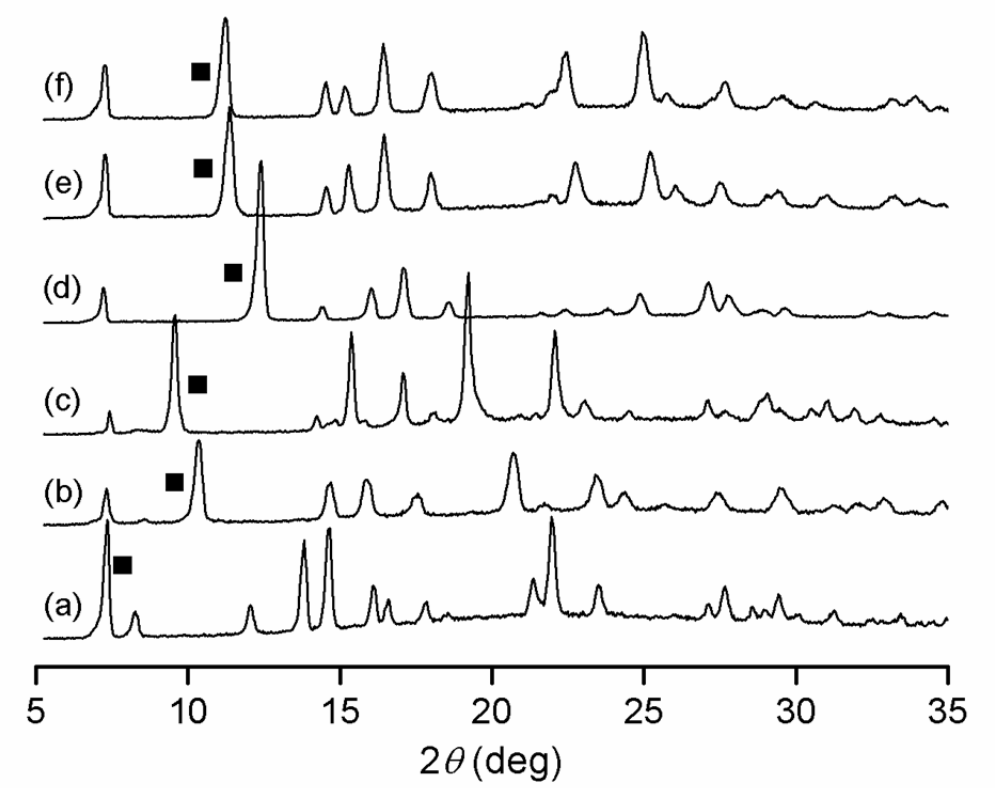


***Figure B.3.*** Powder X-ray diffraction patterns for (a) as-synthesized Cu(MeBDT)(DMF) (**B.1-AS**), (b) evacuated Cu(MeBDT)(DMF) (**B.1-DMF**), (c) Cu(MeBDT)(DEF) (**B.1-DEF**), (d) Cu(MeBDT)(MeOH) (**B.1-MeOH**), (e) Cu(MeBDT)(EtOH) (**B.1-EtOH**), (f) Cu(MeBDT)(DMSO) (**B.1-DMSO**). The filled square symbol indicates the (101) reflection, which readily evolves upon solvent exchange.

**DEF** (Figure B.3c) was possible within the space group *Imma* using a unit cell slightly larger than that observed for **B.1-DMF**, consistent with the slightly greater steric bulk of DEF compared to DMF.

The generality of the substitution of the bridging solvent was tested by submerging samples of **1-AS** within a range of common organic solvents. Indeed, DMF could be displaced by a broad range of other coordinating solvents, such as methanol, ethanol, and DMSO, generating Cu(MeBDT)(MeOH) (**B.1-MeOH**), Cu(MeBDT)(EtOH) (**B.1-EtOH**), and Cu(MeBDT)(DMSO) (**B.1-DMSO**), respectively. Immersion of single-crystals of **B.1-AS** within these coordinating solvents resulted in cracking of the crystals, consistent with the significant mechanical stress imparted by the changes in the dimensions of the one-dimensional channels. However, the powder X-ray diffraction patterns (Figure B.3d-f) could be fully indexed within the space group *Imma* in all cases, affording the unit cell parameters tabulated in Table B.1. Comparison of the unit cell volumes reveals that the pore dimensions follow that of the steric bulk of the coordinated solvent, suggesting the possibility for tuning of the porosity and surface chemistry by use of the appropriate solvent molecule. Notably, the use of solvent molecules larger than the size of the pores, such as 1-butanol and benzyl alcohol resulted in no displacement of the bridging solvent as evidenced by the unchanged powder X-ray pattern following drying of the sample.

***Table B.1.*** Unit cell parameters of as-synthesized and solvent exchanged forms of **B.1**-**B.3** as determined from indexing[a] of the powder X-ray diffraction patterns.

| | **B.1-AS** | **B.1-DMF** | **B.1-DEF** | **B.1-MeOH** | **B.1-EtOH** | **B.1-DMSO** | **B.2** | **B.3-DMF** | **B.3-DEF** | **B.3-DMSO** |
|---|---|---|---|---|---|---|---|---|---|---|
| *a* (Å) | 22.72 | 24.66 | 24.39 | 25.10 | 24.88 | 25.01 | 31.23 | 24.54 | 24.55 | 24.64 |
| *b* (Å) | 7.234 | 7.090 | 7.124 | 7.270 | 7.195 | 7.137 | 6.667 | 6.970 | 6.980 | 6.960 |
| *c* (Å) | 14.95 | 9.290 | 10.21 | 7.561 | 8.338 | 8.480 | 12.98 | 9.390 | 9.948 | 8.618 |
| ***V*** (Å$^3$) | **2349.0** | **1624.3** | **1773.0** | **1379.5** | **1494.0** | **1513.6** | **2702.6** | **1606.1** | **1705.0** | **1478.3** |

[a] Space group: *Imma*

The reaction of $CuCl_2 \cdot 2H_2O$ and $H_2BPDT$ in an acidified DMF and EtOH mixture at room temperature yielded blue, block-shaped crystals of the solvated form of Cu(BPDT)(DMF) (**B.2-AS**). Indexing of the powder X-ray diffraction within the space group *Imma* revealed that the framework is indeed an expanded version of **B.1**. The unit cell parameter *a* (31.559(4) Å) is significantly larger than the corresponding value observed in **B.1-AS** (22.709(5) Å), which is consistent with the use of a longer organic linker, and the formation of wider channels. Interestingly, in contrast to **B.1**, samples of **B.2** washed with methylene chloride and air-dried retained the same powder X-ray diffraction pattern (Figure B.4), indicating structural rigidity upon evacuation of the pores of the framework. The flexibility of **B.2**, and solvent exchange properties thereof, were further assessed by submerging crystals of **B.2** within the same organic solvents as those successfully incorporated into **B.1**. Surprisingly, under all conditions, the framework structure remained rigid, and no changes to the powder X-ray diffraction pattern were detected.

The solvothermal reaction of $CuCl_2 \cdot 2H_2O$ and the fluorinated ligand $H_2TFBDTri$ in DMF at 80 °C in DMF over 4 days resulted in the precipitation of Cu(TFBDTri)(DMF) (**B.3-AS**) as a blue-purple powder. Analysis of the powder X-ray diffraction pattern revealed that the material

is indeed isostructural to **B.1**. Note that in the case of perfluorinated ligands bearing carboxylate functionalities, materials that are isostructural to their non-fluorinated counterparts have not yet been reported.[13] As expected from the higher coordination strength of the ligand, thermogravimetric analysis revealed a modest improvement in the thermal stability of the framework over **B.1** and **B.2**, which may be attributed to the higher thermal stability of the triazole functionality[14] and/or aryl carbon-fluorine bonds.[15] A similar soaking of **B.3-AS** within DEF and DMSO generated the corresponding frameworks Cu(TFBDTri)(DEF) (**B.3-DEF**) and Cu(TFBDTri)(DMSO) (**B.3-DMSO**), respectively. As was observed for **B.1**, the powder X-ray diffraction patterns (Figure B.5a-c) indicated flexibility of the framework, and the resulting unit cell volumes are consistent with the steric bulk of the solvent employed. Surprisingly, when samples of **B.3-AS** were submerged in water or methanol, significant broadening of the reflections in the powder pattern was observed, indicating a decrease in the crystallinity of the sample.

The significant difference in the framework flexibility between compounds **B.1**- **B.3** is quite unexpected due to the structural similarities and network connectivity of the materials. While the exact mechanism giving rise to the solvent substitution is currently unknown, one possibility may lie in the strength of the binding of the bridging solvent molecules as a result of electronic effects and steric demands imposed by the various bridging ligands. Similar effects have been reported recently by Férey and co-workers for derivatives of the MIL-53(Fe) structure type,[16] which exhibited linker-dependent flexibility upon immersion within a variety of organic solvents. Ongoing studies will be directed towards gaining a more detailed understanding of the mechanism of solvent substitution, and effects on the resulting gas sorption properties.

## B.4 Outlook

The foregoing results demonstrate broad applicability of the Cu(BDT)(DMF) structure type, allowing for the generation of three isostructural materials from a variety of organic linkers. The flexibility within this series of framework is strongly influenced by the specific organic bridging unit that is employed, wherein **B.1** is readily flexible upon guest solvent molecules being incorporated into the pores, while the **B.2** remained rigid under all conditions attempted in this study. Flexibility could also be demonstrated for **B.3**, in which DEF and DMSO could be exchanged for DMF. Studies directed towards elucidating the reasons for such a significant difference in the flexibility between these frameworks, are currently underway. Furthermore, efforts to achieve a more detailed understanding of the chemical properties of the channels, such as polarity-dependent guest solubility, and the adsorptive properties of the frameworks, are also ongoing. We envisage that this structure type can be adopted by an even broader range of ligand functionalities, which should lead to an increased understanding of the structure-property relationships within this class of metal-organic framework.

## B.5 Acknowledgments

This work was supported by the Center for Gas Separations Relevant to Clean Energy Technologies, an Energy Frontier Research Center funded by the U.S. Department of Energy, Office of Science, Office of Basic Energy Sciences under award number DE-SC0001015, and

the Korea Research Foundation Grant funded by the Korean Government (MEST) (KRF-2009-220 -C00021). I thank Fulbright New Zealand for partial financial support, and Dr. A. G. DiPasquale for helpful discussions.

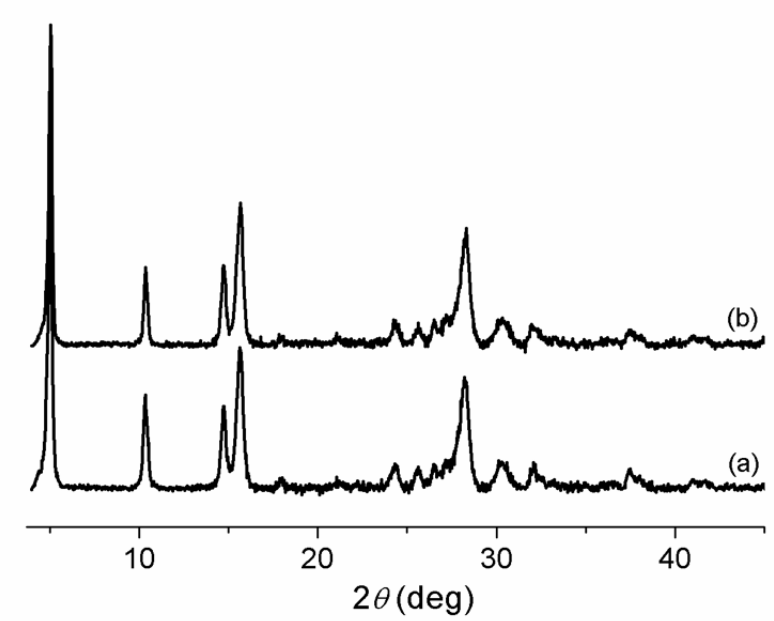


***Figure B.4.*** Powder X-ray diffraction patterns of (a) as-synthesized Cu(BPDT)(DMF) (**B.2-AS**), and (b) following immersion of **B.2-AS** in MeOH. Both diffraction patterns were collected following washing of the solid with dichloromethane, and evacuation of the residual unbound solvent molecules.

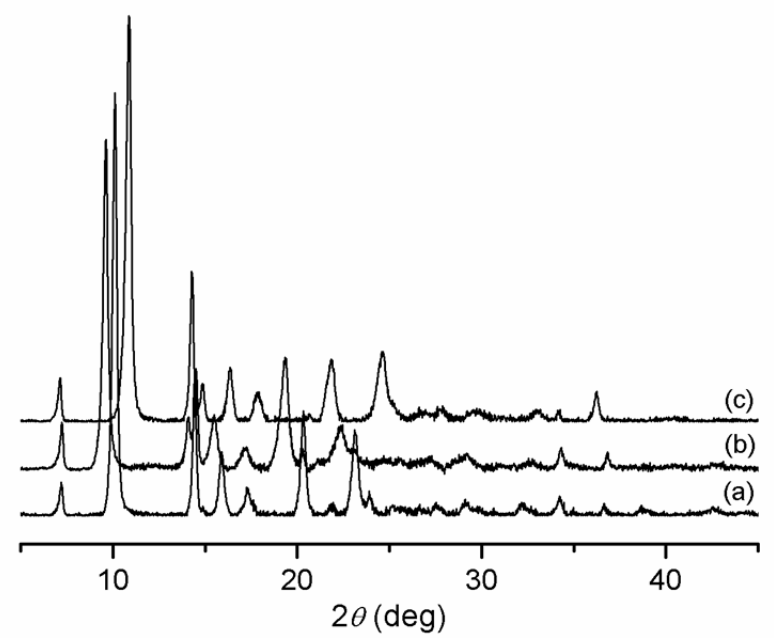


***Figure B.5.*** Powder X-ray diffraction patterns for (a) Cu(TFBDTri)(DMF) (**B.3-DMF**), (b) Cu(TFBDTri)(DEF) (**B.3-DEF**), and (c) Cu(TFBDTri)(DMSO) (**B.3-DMSO**). The intense reflection located at approximately 10° 2$\theta$ represents the (101) reflection, which evolves upon solvent exchange.

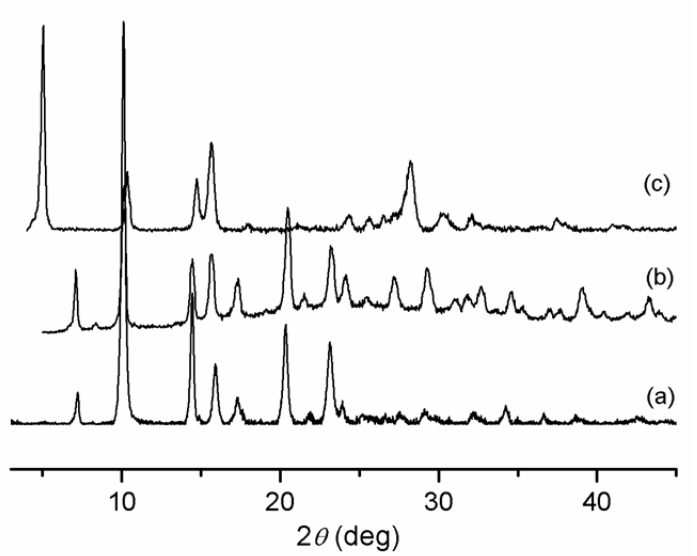


***Figure B.6.*** Powder X-ray diffraction patterns of (a) Cu(MeBDT)(DMF) (**B.1-DMF**), (b) Cu(TFBDTri)(DMF) (**B.2-DMF**), and (c) Cu(BPDT)(DMF) (**B.3-DMF**), following immersion in DMF and evacuation.

***Table B.2.*** Experimental positions (°) of the predominant reflections (*hkl*) within the powder X-ray diffraction patterns of **B.1-AS** used for indexing within the orthorhombic space group *Imma* and fitting of the unit cell parameters.

| $2\theta$ | $h$ | $k$ | $l$ |
|---|---|---|---|
| 7.073 | 1 | 0 | 1 |
| 8.024 | 2 | 0 | 0 |
| 11.803 | 0 | 0 | 2 |
| 13.563 | 3 | 0 | 1 |
| 14.372 | 2 | 0 | 2 |
| 16.334 | 4 | 0 | 0 |
| 15.850 | 2 | 1 | 1 |
| 17.552 | 1 | 1 | 2 |
| 18.308 | 1 | 0 | 3 |
| 21.097 | 3 | 1 | 2 |
| 21.728 | 3 | 0 | 3 |
| 23.251 | 2 | 1 | 3 |

***Table B.3.*** Experimental positions (°) of the predominant reflections (*hkl*) within the powder X-ray diffraction patterns of **B.1-DMF** used for indexing within the orthorhombic space group *Imma* and fitting of the unit cell parameters.

| $2\theta$ | $h$ | $k$ | $l$ |
|---|---|---|---|
| 7.096 | 2 | 0 | 0 |
| 10.141 | 1 | 0 | 1 |
| 14.440 | 3 | 0 | 1 |
| 15.646 | 0 | 1 | 1 |
| 17.342 | 2 | 1 | 1 |
| 19.091 | 0 | 0 | 2 |
| 20.493 | 2 | 0 | 2 |
| 21.519 | 6 | 0 | 0 |
| 23.218 | 1 | 1 | 2 |
| 24.130 | 4 | 0 | 2 |
| 25.442 | 3 | 1 | 2 |
| 27.196 | 1 | 2 | 1 |

***Table B.4.*** Experimental positions (°) of the predominant reflections (*hkl*) within the powder X-ray diffraction patterns of **B.1-DEF** used for indexing within the orthorhombic space group *Imma* and fitting of the unit cell parameters.

| $2\theta$ | $h$ | $k$ | $l$ |
|---|---|---|---|
| 7.163 | 2 | 0 | 0 |
| 9.292 | 1 | 0 | 1 |
| 13.971 | 3 | 0 | 1 |
| 14.572 | 4 | 0 | 0 |
| 15.118 | 0 | 1 | 1 |
| 16.827 | 0 | 0 | 2 |
| 18.963 | 2 | 0 | 2 |
| 21.814 | 6 | 0 | 0 |
| 22.804 | 1 | 1 | 2 |
| 24.255 | 4 | 0 | 2 |
| 26.843 | 1 | 2 | 1 |
| 28.793 | 3 | 2 | 1 |

***Table B.5.*** Experimental positions (°) of the predominant reflections (*hkl*) within the powder X-ray diffraction patterns of **B.1-MeOH** used for indexing within the orthorhombic space group *Imma* and fitting of the unit cell parameters.

| $2\theta$ | $h$ | $k$ | $l$ |
|---|---|---|---|
| 6.961 | 2 | 0 | 0 |
| 12.127 | 1 | 0 | 1 |
| 14.155 | 4 | 0 | 0 |
| 15.775 | 3 | 0 | 1 |
| 16.828 | 0 | 1 | 1 |
| 18.332 | 2 | 1 | 1 |
| 21.385 | 6 | 0 | 0 |
| 22.172 | 4 | 1 | 1 |
| 23.552 | 0 | 0 | 2 |
| 24.625 | 2 | 0 | 2 |
| 26.864 | 1 | 1 | 2 |
| 27.527 | 7 | 0 | 1 |

***Table B.6.*** Experimental positions (°) of the predominant reflections (*hkl*) within the powder X-ray diffraction patterns of **B.1-EtOH** used for indexing within the orthorhombic space group *Imma* and fitting of the unit cell parameters.

| $2\theta$ | $h$ | $k$ | $l$ |
|---|---|---|---|
| 7.019 | 2 | 0 | 0 |
| 11.103 | 1 | 0 | 1 |
| 14.296 | 4 | 0 | 0 |
| 15.065 | 3 | 0 | 1 |
| 17.743 | 2 | 1 | 1 |
| 21.294 | 0 | 0 | 2 |
| 21.755 | 5 | 0 | 1 |
| 22.502 | 2 | 0 | 2 |
| 24.970 | 1 | 1 | 2 |
| 25.814 | 2 | 2 | 0 |
| 27.269 | 7 | 0 | 1 |
| 29.184 | 3 | 2 | 1 |

***Table B.7.*** Experimental positions (°) of the predominant reflections (*hkl*) within the powder X-ray diffraction patterns of **B.1-DMSO** used for indexing within the orthorhombic space group *Imma* and fitting of the unit cell parameters.

| $2\theta$ | $h$ | $k$ | $l$ |
|---|---|---|---|
| 7.016 | 2 | 0 | 0 |
| 10.971 | 1 | 0 | 1 |
| 14.284 | 4 | 0 | 0 |
| 14.926 | 3 | 0 | 1 |
| 16.184 | 0 | 1 | 1 |
| 17.741 | 2 | 1 | 1 |
| 20.910 | 0 | 0 | 2 |
| 21.709 | 4 | 1 | 1 |
| 22.172 | 2 | 0 | 2 |
| 24.737 | 1 | 1 | 2 |
| 27.422 | 1 | 2 | 1 |
| 29.304 | 3 | 2 | 1 |

***Table B.8.*** Experimental positions (°) of the predominant reflections (*hkl*) within the powder X-ray diffraction patterns of **B.2** used for indexing within the orthorhombic space group *Imma* and fitting of the unit cell parameters.

| $2\theta$ | $h$ | $k$ | $l$ |
|---|---|---|---|
| 5.274 | 2 | 0 | 0 |
| 10.599 | 3 | 0 | 1 |
| 14.981 | 2 | 1 | 1 |
| 15.909 | 5 | 0 | 1 |
| 18.223 | 1 | 1 | 2 |
| 24.609 | 2 | 2 | 0 |
| 26.872 | 8 | 1 | 1 |
| 28.491 | 10 | 0 | 0 |

***Table B.9.*** Experimental positions (°) of the predominant reflections (*hkl*) within the powder X-ray diffraction patterns of **B.3-DMF** used for indexing within the orthorhombic space group *Imma* and fitting of the unit cell parameters.

| $2\theta$ | $h$ | $k$ | $l$ |
|---|---|---|---|
| 7.215 | 2 | 0 | 0 |
| 10.116 | 1 | 0 | 1 |
| 14.450 | 4 | 0 | 0 |
| 15.907 | 0 | 1 | 1 |
| 20.341 | 5 | 0 | 1 |
| 23.944 | 4 | 0 | 2 |
| 26.619 | 2 | 2 | 0 |
| 27.572 | 1 | 2 | 1 |
| 29.213 | 5 | 1 | 2 |
| 32.213 | 2 | 1 | 3 |
| 34.244 | 9 | 0 | 1 |
| 38.778 | 1 | 2 | 3 |

***Table B.10.*** Experimental positions (°) of the predominant reflections (*hkl*) within the powder X-ray diffraction patterns of **B.3-DEF** used for indexing within the orthorhombic space group *Imma* and fitting of the unit cell parameters.

| $2\theta$ | $h$ | $k$ | $l$ |
|---|---|---|---|
| 7.250 | 2 | 0 | 0 |
| 9.575 | 1 | 0 | 1 |
| 14.068 | 3 | 0 | 1 |
| 15.497 | 0 | 1 | 1 |
| 17.167 | 2 | 1 | 1 |
| 23.030 | 4 | 0 | 2 |
| 29.070 | 8 | 0 | 0 |
| 36.896 | 2 | 0 | 4 |
| 19.217 | 2 | 0 | 2 |
| 22.206 | 1 | 1 | 2 |
| 23.031 | 4 | 0 | 2 |
| 29.070 | 8 | 0 | 0 |
| 36.896 | 2 | 0 | 4 |

***Table B.11.*** Experimental positions (°) of the predominant reflections (*hkl*) within the powder X-ray diffraction patterns of **B.3-DMSO** used for indexing within the orthorhombic space group *Imma* and fitting of the unit cell parameters.

| $2\theta$ | $h$ | $k$ | $l$ |
|---|---|---|---|
| 7.141 | 2 | 0 | 0 |
| 10.878 | 1 | 0 | 1 |
| 14.303 | 4 | 0 | 0 |
| 14.877 | 3 | 0 | 1 |
| 16.355 | 0 | 1 | 1 |
| 17.837 | 2 | 1 | 1 |
| 20.695 | 5 | 0 | 1 |
| 21.800 | 2 | 0 | 2 |
| 24.628 | 1 | 1 | 2 |
| 27.922 | 1 | 2 | 1 |
| 33.176 | 5 | 2 | 1 |
| 36.238 | 4 | 2 | 2 |

## B.6 References and Notes


(1) (a) Eddaoudi, M.; Kim, J.; Rosi, N.; Vodak, D.; Wachter, J.; O'Keeffe, M.; Yaghi, O. M. *Science* **2002**, *295*, 469. (b) Matsuda, R.; Kitaura, R.; Kitagawa, S.; Kubota, Y.; Belosludov, R. V.; Kobayashi, T. C.; Sakamoto, H.; Chiba, T.; Takata, M.; Kawazoe, Y. *Nature* **2005**, *436*, 238. (c) Férey, G. *Chem. Soc. Rev.* **2008**, *37*, 191. (d) Morris, R. E.; Wheatley, P. S. *Angew. Chem., Int. Ed.* **2008**, *47*, 4966. (e) Férey, G. *Dalton. Trans.* **2009**, 4400.

(2) (a) Millward, A. R.; Yaghi, O. M. *J. Am. Chem. Soc.* **2005**, *127*, 17998. (b) Furukawa, H.; Miller, M. A.; Yaghi, O. M. *J. Mater. Chem.* **2007**, *17*, 3197. (c) Ma, S.; Sun, D.; Simmons, J. M.; Collier, C. D.; Yuan, D.; Zhou, H.-C. *J. Am. Chem. Soc.* **2008**, *130*, 1012. (d) Llewellyn, P. L.; Bourrelly, S.; Serre, C.; Vimont, A.; Daturi, M.; Hamon, L.; De Weireld, G.; Chang, J.-S.; Hong, D.-Y.; Hwang, Y. K.; Jhung, S. H.; Férey, G. *Langmuir* **2008**, *24*, 7245. (e) Murray, L. J.; Dincă, M.; Long, J. R. *Chem. Soc. Rev.* 2009, **38**, 1294. (f) Sumida, K.; Hill M. R.; Horike, S.; Dailly, A.; Long, J. R. *J. Am. Chem. Soc.* **2009**, *131*, 15120.

(3) (a) Demessence, A.; D'Alessandro, D. M.; Foo, M. L.; Long, J. R. *J. Am. Chem. Soc.* **2009**, *131*, 8784. (b) Yazaydin, A. Ö.; Snurr, R. Q.; Park, T.-H.; Koh, K.; Liu, J.; LeVan, M. D.; Benin, A. I.; Jakubczak, P.; Lanuza, M.; Galloway, D. B.; Low, J. J.; Willis, R. R. *J. Am. Chem. Soc.* **2009**, *131*, 18198. (c) Britt, D.; Furukawa, H.; Wang, B.; Glover, T. G.; Yaghi, O. M. *Proc. Nat. Acad. Sci. U. S. A.* **2009**, *49*, 20637.

(4) (a) Rowsell, J. L. C.; Yaghi, O. M. *J. Am. Chem. Soc.* **2006**, *128*, 1304. (b) Pawsey, S.; Moudrakovski, I.; Ripmeester, J.; Wang, L.-Q.; Exarhos, G. J.; Rowsell, J. L. C.; Yaghi, O. M. *J. Phys. Chem. C*, **2007**, *111*, 6060. (c) Kaye, S. S.; Dailly, A.; Yaghi, O. M.; Long, J. R. *J. Am. Chem. Soc.* **2007**, *129*, 14176. (d) Tanabe, K. K.; Wang, Z.; Cohen, S. M. *J. Am. Chem. Soc.* **2008**, *130*, 8508.

(5) (a) Dietzel, P. D. C.; Morita, Y.; Blom, R.; Fjellvag, H. *Angew. Chem., Int. Ed.* **2005**, *44*, 6354. (b) Rosi, N. L.; Kim, J.; Eddaoudi, M.; Chen, B.; O'Keeffe, M.; Yaghi, O. M. *J. Am. Chem. Soc.* **2005**, *127*, 1504. (c) Dietzel, P. D. C.; Panella, B.; Hirscher, M.; Blom, R.; Fjellvag, H. *Chem. Commun.* **2006**, 959. (d) Caskey, S. R.; Wong-Foy, A. G.; Matzger, A. J. *J. Am. Chem. Soc.* **2008**, *130*, 10870. (e) Dietzel, P. D. C.; Blom, R.; Fjellvag, H. *Eur. J. Inorg. Chem.* **2008**, 3624. (f) Zhou, W.; Wu, H.; Yildirim, T. *J. Am. Chem. Soc.* **2008**, *130*, 15268.

(6) (a) Dincă, M.; Dailly, A.; Liu, Y.; Brown, C. M.; Neumann, D. A.; Long, J. R. *J. Am. Chem. Soc.* **2006**, *128*, 16876. (b) Dincă, M.; Han, W. S.; Liu, Y.; Dailly, A.; Brown, C. M.; Long, J. R. *Angew. Chem., Int. Ed.* **2007**, *46*, 1419. (c) Sumida, K.; Horike, S.; Kaye, S. S.; Herm, Z. R.; Queen, W. L.; Brown, C. M.; Grandjean, F.; Long, G. J.; Dailly, A.; Long, J. R. *Chem. Sci.* **2010**, *1*, 184.

(7) (a) Cussen, E. J.; Claridge, J. B.; Rosseinsky, M. J.; Kepert, C. J. *J. Am. Chem. Soc.* **2002**, *124*, 9574. (b) Kitagawa, S.; Kitaura, R.; Noro, S.-I. *Angew. Chem., Int. Ed.* **2004**, *43*, 2334. (c) Maji, T. K.; Mostafa, G.; Matsuda, R.; Kitagawa, S. *J. Am. Chem. Soc.* **2005**, *127*, 17152. (d) Llewellyn, P. L.; Bourrelly, S.; Serre, C.; Filinchuk, Y.; Férey, G. *Angew. Chem., Int. Ed.* **2006**, *45*, 7751. (e) Kondo, A.; Noguchi, H.; Carlucci, L.; Proserpio, D. M.; Ciani, G.; Kajiro, H.; Ohba, T.; Kanoh, H.; Kaneko, K. *J. Am. Chem. Soc.* **2007**, *129*, 12362. (f) Serre, C.; Mellot-Draznieks, C.; Surblé, S.; Audebrand, N.; Filinchuk, Y.; Férey, G. *Science*, **2007**, *315*, 1828. (g) Choi, H. J.; Dincă, M.; Long, J. R. *J. Am. Chem. Soc.* **2008**, *130*, 7848. (h) Horike, S.; Shimomura, S.; Kitagawa, S. *Nat. Chem.* **2009**, *1*, 695.

(8) Dincă, M.; Yu, A. F.; Long, J. R. *J. Am. Chem. Soc.* **2006**, *128*, 8904.
(9) Demessence, A.; Long, J. R. *Chem. Eur. J.* **2010**, *16*, 5902.
(10) Breck, D. W. *Zeolite Molecular Sieves*, Wiley, New York, **1984**.
(11) Loren, J. C.; Krasiński, A.; Fokin, V. V.; Sharpless, K. B. *Synlett* **2005**, *18*, 2847.
(12) Neenan, T. X.; Whitesides, G. M. *J. Org. Chem.* **1988**, *53*, 2489.
(13) Hulvey, Z.; Falcao, E. H. L.; Eckert, J.; Cheetham, A. K. *J. Mater. Chem.* **2009**, *19*, 4307.
(14) Akutsu, Y.; Tamura, M. *J. Energ. Mat.* **1993**, *11*, 205.
(15) Chambers, R. D. *Fluorine in Organic Chemistry,* Blackwell Publishing, Oxford, **2004**.
(16) Devic, T.; Horcajada, P.; Serre, C.; Salles, F.; Maurin, G.; Moulin, B.; Heurtaux, D.; Clet, G.; Vimont, A.; Grenèche, J.-M.; Le Ouay, B.; Moreau, F.; Magnier, E.; Filinchuk, Y.; Marrot, J.; Lavalley, J.-C.; Daturi, M.; Férey, G. *J. Am. Chem. Soc.* **2010**, *132*, 1127.